



**Universidade Nova de Lisboa**

OMNIS CIVITAS CONTRA SE DIVISA NON STABIT

**Faculdade de Ciências e Tecnologia**

Dissertação de Doutoramento

**Characterization of Molybdenum and  
Tungsten Formate Dehydrogenases from  
Sulfate Reducing Bacteria.**

Cristiano de Sousa Mota

Lisboa, 2011



**Cristiano de Sousa Mota**

# **Characterization of Molybdenum and Tungsten Formate Dehydrogenases from Sulfate Reducing Bacteria.**

Dissertação apresentada para a obtenção  
do Grau de Doutor em Bioquímica,  
especialidade Bioquímica-Física pela  
Universidade Nova de Lisboa, Faculdade  
de Ciências e Tecnologia

Lisboa, 2011



- Nº DE ARQUIVO

- COPYRIGHT



## AKNOWLEDGEMENTS

First of all, I would like to express my gratitude to my advisor Prof. Isabel Moura and to Prof. José Moura, for accepting me to carry out my Ph.D. work in their research group, for all the trust in my work and ability to get the results and for all the help in key questions of my Ph.D.

Maria Gabriela Rivas, thank you for all the help, all the teaching, all the patience, all the persistence since the very first beginning. Thanks to you, I'm today a best student and a best scientist (I want to think that!).

Pablo Javier Gonzalez, for all the useful discussions, for all help in the headaches with EPR theory and practice, for all the information about Gaussian v03 and ORCA 2.8 and, for all the fruitfulness brainstorms with the software PES v09 and v10, thank you.

To the latter two, I would like to express my recognition for all the work and contribution in the achievement of this thesis.

Carlos Brondino, Nuno Cerqueira, Alain Dolla, Özlen Ferruh Erdem, Marie-Claire Durand, Edward Reijerse and Wolfgang Lubitz. The collaborators that contributed with experimental data, data discussion and, help to write and discuss manuscripts. Thanks for your useful knowledge.

To Bioin and Bioprot groups thanks for your friendship, you teach me a lot about research and lab work, it was a pleasure work with you every single day.

Thanks to Fundação para a Ciência e Tecnologia for funding (Grant SFRH/BD/32478/2006).

To my friends, they know who they are, thanks for your friendship, all the support, for becoming my days so happy.

To my family, the most important people in my life, thank you for all the support in good and bad moments.

Finally but not less, Fânia thanks for all the support, friendship and love. This was not easy for you too! This thesis is fruit of our work. Thank you!



## RESUMO

As enzimas de Mo e W têm funções vitais na catálise de passos fundamentais do metabolismo do carbono, azoto e enxofre. Estes metais em condições fisiológicas são activos redox, variando entre os estados de oxidação IV, V e VI.

Esta tese reporta sobre desidrogenases de formato (Fdhs) que contêm Mo e W, estas enzimas pertencem à família das DMSO reductases das enzimas mononucleares de Mo e W. No centro activo destas enzimas o ião metálico é coordenado por quatro átomos de enxofre pertencentes a duas moléculas de piranopterin, um selénio de uma selenocisteína (SeCys) e um enxofre inorgânico. Estas enzimas contêm também nas suas estruturas outros cofactores redox como centros [4Fe-4S] e em alguns casos, grupos hemo.

No Capítulo I é feita uma introdução geral ao âmbito das enzimas de Mo e W, enquanto uma visão mais aprofundada no conhecimento actual das Fdhs de Mo e W é apresentada no Capítulo II.

O Capítulo III descreve os estudos aplicados para compreender os efeitos da suplementação com Mo e W, no meio de cultura, nos níveis de expressão e propriedades bioquímicas das Fdhs isoladas de *D. alaskensis*. Duas Fdhs diferentes são expressas, uma que pode conter no centro activo tanto Mo como W (Mo/W-Fdh), e outra que apenas pode incorporar W (W-Fdh). Ambas as enzimas foram purificadas de células cultivadas em meio suplementado com Mo, enquanto em meio suplementado com alta concentração de W apenas a W-Fdh pode ser isolada. Os genes que codificam para ambas as enzimas foram identificados e os níveis de expressão nas condições optimizadas foram avaliados por RT-PCR. Os resultados mostraram que os genes que codificam a Mo/W-Fdh (*Mo/W-fdh*) foram fortemente reprimidos na presença de W e ligeiramente sobreexpressos na presença de Mo. Contudo, a expressão dos genes *W-fdh* são menos susceptíveis tanto à suplementação com Mo como com W. Foi ainda observado que tanto a presença de Mo como de W induz a repressão dos genes envolvidos no transporte de Mo e W. As características das Fdhs e a especificidade para incorporar tanto Mo como W são discutidas neste capítulo.

O mecanismo catalítico das Fdhs foi estudado por meios cinéticos e computacionais no capítulo IV. A Fdh catalisa a reacção redox de oxidação do formato a dióxido de carbono que envolve a transferência de dois electrões do substrato para o ião metálico

presente no centro activo. O mecanismo catalítico foi simulado usando ferramentas de DFT e correlacionado com as propriedades cinéticas experimentais tanto de Fdhs isoladas de três espécies de *Desulfovibrio* como de outros exemplos reportados na literatura. Os nossos estudos indicaram que a substituição do Mo por W no centro activo não afectava a velocidade de reacção. A função de alguns aminoácidos conservados perto do centro metálico é também discutida.

O Capítulo V foca os tipos de inibição que nitrato, azida e cianeto produzem nas Fdhs. Foram determinadas as constantes cinéticas de três Fdhs similares, de espécies *Desulfovibrio*, na presença destes inibidores. O nitrato inibe a oxidação de formato de um modo competitivo enquanto a azida é um forte inibidor e exhibe um tipo de inibição misto. O cianeto inibe a Fdh de Mo de *D. desulfuricans*, demonstrando um tipo de inibição misto, mas não tem qualquer efeito nas Fdhs de W isoladas de *D. gigas* e *D. alaskensis*. Esta diferença observada entre as enzimas de Mo e W é discutida baseada nas propriedades do metal do centro activo, nos aminoácidos na vizinhança do centro e nas subunidades que compõem as enzimas.

No Capítulo VI foram aplicadas ferramentas de DFT de forma a tentar entender os dados espectroscópicos disponíveis na literatura. Foram propostos modelos estruturais do centro de Mo com o objectivo de clarificar as propriedades espectroscópicas dos sinais de EPR de Mo(V) observados na Fdh-H de *E. coli* e Fdh de *D. desulfuricans*. A importância destes modelos do centro activo no mecanismo catalítico das Fdhs é também proposto.

No último capítulo são apresentados os comentários finais da tese e é proposto trabalho futuro.

## ABSTRACT

Mo and W-containing enzymes have crucial physiological roles in catalysis of key steps in the carbon, nitrogen and sulfur metabolism. These metals are redox-active under physiological conditions ranging between oxidation states VI, V and IV.

This thesis deals with Mo and W containing formate dehydrogenases (Fdhs), which belong to the DMSO reductase family of mononuclear Mo and W enzymes. The metal ion at the active site is coordinated by four sulfur atoms from two pyranopterin molecules, a Se from a SeCys and an inorganic sulfur atom. These enzymes also harbor in their structures other redox cofactors such as [4Fe-4S] centers and in some cases heme groups.

A general introduction to the field of Mo- and W-enzymes is described in Chapter I whereas a deeper overview of the current knowledge regarding Mo- and W-Fdhs is summarized in Chapter II.

Chapter III describes studies aimed to understand the effects of Mo and W supplementation on the gene expression levels and biochemical properties of the Fdhs isolated from *D. alaskensis*. Two different Fdhs can be expressed, one that can harbor either Mo or W in the active site, and a second one that only incorporates W. Both enzymes were purified from the cells cultured in medium supplemented with Mo, whereas only the W-Fdh can be isolated from cells cultured in medium supplemented with high W concentrations. The genes coding both enzymes were identified and the expression levels under the conditions tested were evaluated by RT-PCR. The results showed that the genes encoding the Mo/W-Fdh (*Mo/W-fdh*) were strongly down-regulated in the presence of W and slightly up-regulated in the presence of Mo. However, the *W-fdh* genes expression was less susceptible to either Mo or W supplementation. Furthermore it was observed that the presence of either Mo or W induces down-regulation of the genes involved in Mo and W transport. The characteristics of Fdhs and the specificity to incorporate either Mo or W are discussed.

The catalytic mechanism of Fdhs was studied by kinetic and computational means in Chapter IV. Fdh catalyze the oxidation of formate to carbon dioxide in a redox reaction that involves the transfer of two electrons from the substrate to the metal ion present in the active site. The catalytic mechanism of Fdh has been simulated using DFT tools and correlated with the experimental kinetic properties of both Fdhs isolated from three

different *Desulfovibrio* species and some other examples reported in the literature. Our studies indicate that the substitution of Mo for W in the active site does not affect the turnover rates. Also, the role of some conserved aminoacids located near to the metal site is discussed.

The Chapter V focuses on the determination of the type of inhibition that nitrate, azide and cyanide have on Fdhs. The kinetics constants of three similar Fdhs from *Desulfovibrio* species in presence of such inhibitors were determined. Nitrate inhibits the formate oxidation in a competitive way while azide is a strong inhibitor showing a mixed inhibition type. Cyanide can inhibit the Mo-Fdh from *D. desulfuricans* in a mixed way but has no effect on W-Fdhs isolated from *D. gigas* and *D. alaskensis*. This difference observed between the Mo and W enzymes is discussed based on the properties of the active site metal, aminoacids in the neighborhood of the active site, and the subunit composition of the enzymes.

In Chapter VI, DFT tools have been used to explain the spectroscopic data available in the literature. Structural models of the Mo-site were proposed in order to clarify the spectroscopic properties of both the formate and azide Mo(V) EPR signals observed in *Ec* Fdh-H and *Dd* Fdh. The relevance of these active site models in the catalytic mechanism of Fdhs is discussed.

In the last Chapter the final remarks of the thesis are presented and future work is proposed.

## ABBREVIATIONS

3D	Three dimensional
Å	Angstrom
A	Value of the hyperfine coupling
<i>A. thaliana</i>	<i>Arabidopsis thaliana</i>
a.u.	Atomic unit
A <sub>280 nm</sub>	Absorbance at 280 nm
A <sub>400 nm</sub>	Absorbance at 400 nm
<i>Aa</i>	<i>Aromateleum aromaticum</i>
Aba3	Protein involved in Moco sulfuration in plants
ABC transporter	Adenosine triphosphate binding cassette transporter
ADP	Adenosine diphosphate
AMP	Adenosine monophosphate
AOR	Aldehyde ferredoxin oxidoreductase
AOX	Aldehyde oxidase
Arg	Arginine
Asn	Asparagine
Asp	Aspartate
ATCC	American type culture collection
ATP	Adenosine triphosphate
β-ME	Beta mercaptoethanol
BV	Benzyl viologen
c.a.	From the latin "circa" that means around
cDNA	Complementary DNA
CMP	Cytidine monophosphate
<i>Cn</i>	<i>Cupriavidus necator</i>
Cnx1E/G	Protein involved in Moco biosynthesis from plants
Cnx2/3/5/6/7	Proteins involved in Moco biosynthesis from plants
CO dehydrogenase	Carbon monoxide dehydrogenase
CODH	Carbon monoxide dehydrogenase
CPCM	Conductor-like polarizable continuum model
cPMP	Cyclic pyranopterin monophosphate
CTP	Cytidine triphosphate

CW	Continuous wave
Cys	Cysteine
<i>D. alaskensis</i> or <i>Da</i>	<i>Desulfovibrio alaskensis</i> NCIMB 13491
<i>D. desulfuricans</i> G20	<i>Desulfovibrio desulfuricans</i> G20
<i>D. desulfuricans</i> or <i>Dd</i>	<i>Desulfovibrio desulfuricans</i> ATCC 27774
<i>D. gigas</i> or <i>Dg</i>	<i>Desulfovibrio gigas</i> NCIB 9332
<i>D. vulgaris</i>	<i>Desulfovibrio vulgaris</i> Hildenborough
Da	Dalton
DE-52	Anion exchange resin based on cellulose with diethylaminoethyl ligands
DFT	Density functional theory
DMSO	Dimethyl sulfoxide
DMSOr	Dimethyl sulfoxide reductase
DNA	Deoxyribonucleic acid
dNTPs	Deoxynucleotide triphosphates
DTT	Dithiothreitol
$\epsilon$	UV-Vis extinction coefficient
<i>E. acidaminophilum</i>	<i>Eubacterium acidaminophilum</i>
<i>E. coli</i> or <i>Ec</i>	<i>Escherichia coli</i>
E.C.C.	Enzyme Commission Classes
$E_a$	Activation energy
EBDH	Ethylbenzene dehydrogenase
EC	Enzyme Classe
EDTA	Ethylenediamine tetraacetic acid
ENDOR	Electron nuclear double resonance
EPR	Electron paramagnetic resonance
$E_r$	Reaction energy
ES	Enzyme-substrate complex
ESEEM	Electron spin echo envelope modulation
<i>et al</i>	From the Latin "et alli" means and others
Euk	Eukaryotic
EXAFS	Extended X-ray Absorption Fine Structure
Fdh	Formate dehydrogenase
<i>fdh</i>	formate dehydrogenase gene
<i>fdh3</i>	Dde_812-Dde_813 genes from <i>D. desulfuricans</i> G20

<i>fdhD/E</i>	Gene codifying for a Fdh chaperone
Fdh-H	Formate dehydrogenase-H from <i>E. coli</i>
Fdh-N	Formate dehydrogenase N from <i>E. coli</i>
Fdhs	Formate dehydrogenases
FeMoco	Molybdenum iron cofactor
g	g-factor
Geph-E/G	Proteins involved in Moco biosynthesis from human
Gln	Glutamine
GMP	Guanosine monophosphate
GTP	Guanosine triphosphate
hfc	Hyperfine coupling
His	Histidine
HPLC	High-performance liquid chromatography
HYSCORE	Hyperfine sub-level correlation
ICP-AES	Inductively coupled plasma atomic emission spectroscopy
Ile	Isoleucine
IRC	Internal reaction coordinate
kcal	kiloCalories
$k_{cat}$	Catalysis constant
kDa	kiloDalton
$K_{ic}$	Competitive inhibition constant
$K_{iuc}$	Uncompetitive inhibition constant
$K_M$	Michaelis-Menten constant
KPB	Potassium phosphate buffer
Leu	Leucine
<i>M. barkeri</i>	<i>Methanosarcina barkeri</i>
<i>M. formicium</i>	<i>Methanobacterium formicium</i>
<i>M. thermoautotrophicum</i>	<i>Methanobacterium thermoautotrophicum</i>
<i>M. wolfei</i>	<i>Methanobacterium wolfei</i>
MCD	Molybdopterin cytidine dinucleotide
Met	Metionine
Mg-ATP	Magnesium-binding adenosine triphosphate
MGD	Molybdopterin guanosine dinucleotide
<i>Mo/W-fdh</i>	Dde_3512-3514 genes from <i>D. desulfuricans</i> G20

Mo/W-Fdh	Fdh incorporating molybdenum or tungsten
MoaA	Protein involved in Moco biosynthesis from <i>E. coli</i>
<i>moaABCDE</i>	Operon involved in Moco biosynthesis
MoaB/C/D/E	Proteins involved in Moco biosynthesis from <i>E. coli</i>
MobA/B	Proteins involved in guanosine/cytidine monophosphate attachment to the Moco in <i>E. coli</i>
<i>mobAB</i>	Operon involved in Moco biosynthesis
Moco	Molybdenum cofactor
MocoCD	Human Moco deficiency
MOCOS	Protein involved in Moco sulfuration in human
Mocs1	Human MoaA homologue
MOCS1A/B or 2A/B or 3A	Proteins involved in Moco biosynthesis from human
<i>mod</i>	Operon that codifies to molybdenum ABC transporter
<i>modA</i>	Gene codifying to the periplasmic molybdenum-binding protein from the molybdenum ABC transporter
ModA	Molybdenum ABC transporter, periplasmic molybdenum-binding protein
<i>modB</i>	Gene coding to the permease protein from molybdenum ABC transporter
ModB	Molybdenum ABC transporter, permease protein
<i>modC</i>	Gene codifying to the ATP-binding protein from molybdenum ABC transporter
ModC	Molybdenum ABC transporter, ATP-binding protein
ModE	Protein involved in Moco biosynthesis regulation
<i>moeA</i>	Gene that express the protein involved in molybdenum/tungsten incorporation
MoeA	Protein involved in molybdenum/tungsten incorporation by the cofactor
<i>moeAB</i>	Operon involved in Moco biosynthesis
MoeB	Protein involved in Moco biosynthesis from <i>E. coli</i>
<i>mogA</i>	Gene involved in Moco biosynthesis
MogA	Protein involved in Moco biosynthesis from <i>E. coli</i>
MPT	Metal-binding pterin
MPT synthase	Metal-binding pterin synthase
MPT-AMP	Adenylylated metal-binding pterin
MW	Molecular weight
NAD <sup>+</sup>	Nicotinamide adenine dinucleotide
NADH	Nicotinamide adenine dinucleotide
NapA/AB	Periplasmic nitrate reductase A/AB



Nar	Dissimilatory nitrate reductase
NarGH/I	Nitrate reductase GH / nitrate reductase GHI
NCIB	National collection of industrial bacteria
NCIMB	National collection of industrial, marine and food bacteria
NR	Nitrate reductase
<i>O. carboxidovorans</i>	<i>Oligotropha carboxidovorans</i>
OD	Optical density
<i>P. aerophilum</i>	<i>Pyrobaculum aerophilum</i>
<i>P. denitrificans</i>	<i>Paracoccus denitrificans</i>
PCR	Polymerase chain reaction
PDB	Protein data bank
<i>P. furiosus</i> or <i>Pf</i>	<i>Pyrococcus furiosus</i>
PGD	Pyranopterin guanine dinucleotide
P <sub>i</sub>	Inorganic phosphate
pI	Isoelectric point
ppm	Part per million
psi	Pound-force per square inch
qRT-PCR	Quantitative real-time PCR
<i>R. capsulatus</i>	<i>Rhodobacter capsulatus</i>
REST	Relative expression software tool
RMSD	Root mean square deviation
RNA	Ribonucleic acid
RNAse	Ribonuclease
ROS	Reactive oxygen species
SDH	Sulfite dehydrogenase
SDS-PAGE	Sodium dodecyl sulfate polyacrylamide gel electrophoresis
SECIS element	Selenocysteine insertion element
SeCys	Selenocysteine
<i>selA/B/C/D</i>	Genes that express the protein involved in selenocysteine insertion
SelB	Selenocysteine tRNA-specific elongation factor
Ser	Serine
S <sub>i</sub>	Inorganic sulfur
SO	Sulfite oxidase
SorAB	Periplasmic sulfite dehydrogenase AB

sp.	Species
SRB	Sulfate reducing bacteria
<i>T. weissflogii</i>	<i>Thalassiosira weissflogii</i>
TMAO	Trimethylamine N-oxide
<i>tup</i>	Operon codifying to the molybdenum ABC transporter
<i>tupA</i>	Gene codifying to the periplasmic tungsten uptake protein from the Tungsten-specific ABC transporter
TupA	Tungsten-specific ABC transporter, periplasmic tungsten uptake protein
<i>tupB</i>	Gene codifying to the permease protein from the Tungsten-specific ABC transporter
TupB	Tungsten-specific ABC transporter, permease protein
<i>tupC</i>	Gene codifying to the ATP-binding protein from the Tungsten-specific ABC transporter
TupC	Tungsten-specific ABC transporter, ATP-binding protein
U	Enzyme unit - amount of the enzyme that catalyzes the conversion of 1 mmol of substrate per minute
UGA codon	Stop codon
UV-Vis	Ultraviolet-visible
Val	Valine
Wco	Tungsten cofactor
<i>W-fdh</i>	<i>Dde_0716-07178</i> genes from <i>D. desulfuricans</i> G20
W-Fdh	Fdh incorporating tungsten
WO <sub>4</sub> <sup>2-</sup>	Tungstate
WtpA	Tungsten-specific ABC transporter, periplasmic tungsten uptake protein
WtpB	Tungsten-specific ABC transporter, permease protein
WtpC	Tungsten-specific ABC transporter, ATP-binding protein
XANES	X-ray Absorption near edge structure
XAS	X-ray absorption spectroscopy
XDH	Xanthine dehydrogenase
XdhC	Protein involved in Moco sulfurilation in <i>R. capsulatus</i>
XO	Xanthine oxidase

## TABLE OF CONTENTS

	Page
AKNOWLEDGEMENTS	I
RESUMO	III
ABSTRACT	V
ABBREVIATIONS	VII
TABLE OF CONTENTS	XIII
FIGURES INDEX	XVII
<b>Chapter I: <i>General introduction</i></b>	<b>1</b>
<b>I.1 Metals in proteins</b>	<b>2</b>
<b>I.2 Cell biology of molybdenum and tungsten</b>	<b>4</b>
I.2.1 Cellular uptake	4
I.2.2 Biosynthesis of the cofactor	5
I.2.3 Molybdenum cofactor deficiency	8
<b>I.3 Molybdenum and tungsten enzymes</b>	<b>8</b>
I.3.1 Categories and general structures of mononuclear Mo/W containing enzymes	9
I.3.1.1 The xanthine oxidase family	11
I.3.1.2 The sulfite oxidase family	12
I.3.1.3 The DMSO reductase family	12
<b>I.4 Subject and objectives of this thesis</b>	<b>13</b>
<b>I.5 References</b>	<b>14</b>
<b>Chapter II: <i>Biology and structure of Fdhs</i></b>	<b>19</b>
<b>II.1 Introduction</b>	<b>20</b>
<b>II.2 Fdh: an overview of the biochemical and crystallographic characteristics</b>	<b>22</b>
II.2.1 Fdh-H from <i>E. coli</i>	22
II.2.2 Fdh-N from <i>E. coli</i>	24
II.2.3 Fdh from <i>D. gigas</i>	25
II.2.4 Fdh from <i>D. desulfuricans</i>	26
<b>II.3 References</b>	<b>27</b>

<b>Chapter III: <i>Influence of Mo and W in the expression of Fdh from D. alaskensis</i></b>	31
<b>III.1 Summary</b>	32
<b>III.2 Introduction</b>	32
<b>III.3 Experimental procedures</b>	34
III.3.1 Bacterial strain, culture media, and growth conditions.	34
III.3.2 Soluble extract preparation and activity tests.	34
III.3.3 Enzymes purification.	36
III.3.4 Protein and metal content quantification.	37
III.3.5 Molecular mass and cofactor content determination.	37
III.3.6 Determination of the N-terminal sequence of Fdhs from <i>D. alaskensis</i> .	37
III.3.7 Quantitive real-time PCR (qRT-PCR).	38
<b>III.4 Results</b>	40
III.4.1 Carbon source and optimal metal concentration for Fdh production.	40
III.4.2 Protein purification, identification and biochemical characterization.	42
III.4.3 Gene expression analysis.	45
<b>III.5 Discussion</b>	48
<b>III.6 References</b>	53
<b>Chapter IV: <i>The mechanism of formate oxidation by Fdh</i></b>	59
<b>IV.1 Summary</b>	60
<b>IV.2 Introduction</b>	60
<b>IV.3 Experimental procedures</b>	64
IV.3.1 Bacterial strain, culture media, and growth conditions.	64
IV.3.2 Enzymes purification.	64
IV.3.3 Enzyme Kinetic Assays.	64
IV.3.4 Theoretical calculations.	65
IV.3.4A The configuration of the active site.	65
IV.3.4B Methods used.	65
<b>IV.4 Results</b>	67
IV.4.1 Steady-state kinetic studies.	67

IV.4.2 DFT calculations.	69
IV.4.2.1 Structure and oxidation state of the active site.	69
IV.4.2.2 Formation of enzyme-substrate complex: selenium-sulfur shift.	71
IV.4.2.3 Formation of selenide anion and formate oxidation.	71
IV.4.2.4 Carbon dioxide release.	77
IV.4.2.5 Regeneration of the active site to the initial state.	79
<b>IV.5 Discussion</b>	82
<b>IV.6 References</b>	87
<b>Chapter V: <i>Inhibition studies on Fdhs</i></b>	91
<b>V.1 Summary</b>	92
<b>V.2 Introduction</b>	92
<b>V.3 Experimental procedures</b>	94
V.3.1 Bacterial strain, culture media, and growth conditions.	94
V.3.2 Enzymes purification.	94
V.3.3 Fdhs sequences alignments and three-dimensional structures alignments.	94
V.3.4 Enzyme inactivation test.	94
V.3.5 Enzyme kinetic assays.	95
V.3.6 Analysis of initial rate data.	95
<b>V.4 Results</b>	96
V.4.1 Inhibition studies	96
V.4.1.1 Inhibition by nitrate.	96
V.4.1.2 Inhibition by azide.	101
V.4.1.3 Inhibition by cyanide.	106
V.4.2 Homology between $\alpha$ and $\beta$ subunits of Fdhs.	107
<b>V.5 Discussion</b>	112
<b>V.6 References</b>	115
<b>Chapter VI: <i>Theoretical methods revising spectroscopic data</i></b>	119
<b>VI.1 Summary</b>	120
<b>VI.2 Introduction</b>	120

<b>VI.3 Theoretical methods</b>	124
VI.3.1 Structure optimizations	124
VI.3.2 EPR parameters	124
<b>VI.4 Results</b>	125
<b>VI.5 Discussion</b>	130
<b>VI.6 References</b>	132
<b>Chapter VII: <i>Final remarks and future work</i></b>	135

## FIGURES INDEX

	Page
<p><b>Figure I.1  Metals used in catalysis. A,</b> The elements used as cofactors by enzymes are shown in green. The height of each column represents the proportion of all enzymes with known structures using the respective metal. A single enzyme use cadmium (carbonic anhydrase from <i>T. weissflogii</i> [6]). <b>B,</b> The proportion of proteins using the indicated metals that occur in each of the six enzyme classes: oxidoreductases (EC 1), blue; transferases (EC 2), yellow; hydrolases (EC 3), purple; lyases(EC 4), pink; isomerases (EC 5), green; ligases (EC 6), grey. EC, Enzyme Commission. Figures were taken from reference [3].</p>	3
<p><b>Figure I.2  Biosynthesis of the Pyranopterin-based molybdenum cofactors.</b> Schematic overview of the molybdenum cofactor biosynthesis adapted from reference[12] and based on data derived from studies in <i>E. coli</i>, plants and humans. Abbreviations of the intermediates are written in bold on the left side of their structures, and the enzymes are on the right side of the arrows. The fifth step present only in prokaryotes. For MPT and MPT-AMP, the dithiolate sulfurs are bonded to a Cu, because in the crystal structure of plant Cnx1G was found a copper ion in that place.</p>	6
<p><b>Figure I.3  Active-site structures of the different families molybdo- and tungsto-pterins containing enzymes.</b> XO/XDH: xanthine oxidase/xanthine dehydrogenase; CODH: carbon monoxide dehydrogenase; NDH: Nicotinate dehydrogenase; SO: sulfite oxidase; SDH: sulfite dehydrogenase; Euk-NR: eukaryotic nitrate reductase; <i>Dg</i> Fdh: <i>Desulfovibrio gigas</i> formate dehydrogenase; <i>Ec</i> Fdh-H: <i>Escherichia coli</i> formate dehydrogenase H; <i>Dd</i> NapA: <i>Desulfovibrio desulfuricans</i> ATCC 27774 periplasmatic nitrate reductase A; <i>Cn</i> NapAB: <i>Cupriavidus necator</i> periplasmatic nitrate reductase AB; <i>Aa</i> EBDH: <i>Aromateleum aromaticum</i> ethylbenzene dehydrogenase; <i>Ec</i> NarGH/I: <i>Escherichia coli</i> nitrate reductase GH/nitrate reductase GHI; <i>Pf</i> AOR: <i>Pyrococcus furiosus</i> aldehyde ferredoxin:oxidoreductase.</p>	10
<p><b>Figure II.1  NAD-dependent Fdh active site.</b> Crystal structure of NAD-dependent formate dehydrogenase active site from methylotrophic bacterium <i>Pseudomonas</i> sp. 101, adapted from [1].</p>	20
<p><b>Figure II.2  <i>E. coli</i> formate dehydrogenase H structure [17].</b> Left: Fdh-H structure at 2.27 Å (PDB code: 2IV2). Right: Redox centers in Fdh-H: molybdenum active site and [4Fe-4S] center.</p>	22
<p><b>Figure II.3  Active site of Fdh-H from <i>E. coli</i>.</b> A: Oxidized Fdh-H active site [6]. B: Reduced Fdh-H active site [6]. C: Reduced Fdh-H active site (reinterpretation) [17].</p>	23
<p><b>Figure II.4  <i>E.coli</i> Fdh-N structure[7].</b> Left: Fdh-N structure at 1.6Å (PDB code:1KQF). Right: Redox centers in Fdh-N: molybdenum active site, [4Fe-4S] centers and type <i>b</i> hemes.</p>	25

**Figure II.5| *D. gigas* Fdh structure[9].** Left: Fdh structure at 1.8Å (PDB code:1H0H). Right: Redox centers in Fdh: tungsten active site and [4Fe-4S] centers.

26

**Figure III.1| In gel Fdh activity test of *D. alaskensis* cells grown in medium C [17] with different carbon sources.** Cells cultured until the end of the exponential phase ( $OD_{600}=0.5-0.6$ ) in medium C [33] with different carbon sources, harvested and subjected to the procedure described in Material and Methods section to obtain the soluble fraction. The amount of total proteins loaded in each lane was 10 µg. Panel (A) shows the effect of the partial replacement of lactate by formate and/or acetate, and panel (B) the optimization of formate concentration for maximal in-gel specific Fdh activity. Concentrations of lactate, acetate and formate in the culture medium for each growth condition are indicated below the respective lanes.

40

**Figure III.2| Influence of W and Mo on the Fdh activity of soluble extract of *D. alaskensis*.** The soluble extracts were obtained as described in the Material and Methods section from cells grown until the end of the exponential phase ( $OD_{600}=0.5-0.6$ ) in modified medium C supplemented with different concentrations of  $Na_2WO_4 \cdot 2H_2O$  (A) or  $Na_2MoO_4 \cdot 2H_2O$  (B). Total amount of proteins loaded in each lane in tungstate and molybdate supplementation conditions was 10 µg and 45 µg, respectively.

41

**Figure III.3| UV-visible spectrum and electrophoresis gels.** UV-visible spectrum of W-Fdh (black line) and Mo/W-Fdh (gray line) isolated from *D. alaskensis* cells. Inset: (A) SDS-PAGE of W-Fdh (lane 1, 2 µg) and molecular weight markers (lane 2); (B) SDS-PAGE of molecular weight markers (line 1) and Mo/W-Fdh (lane 2, 1 µg); (C) in-gel activity of the as-purified W-Fdh (lane 1, 2 µg) and Mo/W-Fdh (lane 2, 9 µg).

43

**Figure III.4| Influence of metal in Fdh expression.** Relative gene expression of *Mo/W-fdh* and *w-fdh* depending on metal supplementation. Ratio of transcripts abundance of *Mo/W-fdhA* (*Dde\_3513*) (□) or *W-fdhA* (*Dde\_0717*) (■) from *D. alaskensis* cultured in modified medium C supplemented with either 1µM molybdate or 10µM tungstate versus culture in modified medium C without metal supplementation.

46

**Figure III.5| Influence of metal in transporters and MoeA expression.** Relative expression of *modB* (*Dde\_3519*) and *tupB* (*Dde\_0233*) genes encoding proteins responsible for Mo and W transport and *moeA1* (*Dde\_0230*) and *moeA2* (*Dde\_3228*) genes putatively involved in the selective incorporation of Mo or W in the cofactor [25,30] as determined by using quantitative real-time PCR. The abundance of transcripts was determined from *D. alaskensis* cells cultured until the end of the exponential phase ( $OD_{600}=0.5-0.6$ ) in modified medium C supplemented with either 1 µM Mo (□) or 10 µM W (■) and in modified medium C without metal addition.

47



**Figure III.6 Organization of the *fdh* genes, elements putatively involved in molybdenum transport and metal cofactor biosynthesis and incorporation present in the *fdh* genes surrounding area.** (A) *fdh1E* and *fdh1D* genes encode for proteins probably involved in Fdh formation, *MobA* gene codes for a protein that catalyzes the conversion of MPT to MGD, *moaA* gene codes for a protein that catalyzes the conversion of GTP into cyclic pyranopterin monoPhosphate (precursor Z), *W-fdhA* and *W-fdhB* genes encoding the alpha and beta subunits of the W-Fdh, respectively. *Dde\_0719* gene encodes a protein homologous to MobB which binds GTP and has weak GTPase activity [40]. (B) *Mo/W-fdhA* and *Mo/W-fdhB* genes encoding the alpha and beta subunits of the Mo/W-Fdh. The *modABC* genes encode the molybdate uptake transport system. The *modE* encodes a protein that regulates the *modABC* operon expression [31,41,42]. (C) *Dde\_0230* gene encodes a homologous MoeA protein involved in Mo/W insertion into the MPT. *Dde\_0232-Dde\_0234* genes codify for an ABC-type tungstate transport system (TupA, TupB, and TupC) similar to the *modABC* gene cluster. (D) *fdh3A* and *fdh3B* genes encoding a third putative periplasmic Fdh.

49

**Figure IV.1|*E. coli* Fdh-H active site in the presence of nitrite.** Fdh structure at 2.9Å (PDB code:1FDI) [6].

61

**Figure IV.2| Reaction mechanisms proposed for the oxidation of formate to carbon dioxide by Fdhs.** (A) Mechanism proposed by Boyington *et al* where the SeCys remains bonded to the Mo atom during the catalysis [6]. (B) Mechanism proposed by Raaijmakers *et al* where the SeCys bond is replaced by a formate molecule in the first step of the reaction [17].

62

**Figure IV.3| Fdh model.** Model used to study the catalytic mechanism of formate dehydrogenase (frozen atoms are marked with the F letter and the truncation of the residues marked with a white asterisk).

65

**Figure IV.4| Enzyme activation.** Kinetic timescan of the reduction of benzyl viologen monitored at 555 nm catalyzed by Mo-dependent Fdh from *D. desulfuricans*. **Red:** with activation, Fdh (35 nM) was incubated with 10 mM of sodium formate in 60 mM Tris-HCl buffer pH 8.0 and 133 mM  $\beta$ -mercaptoetanol at 37 °C. The reaction was started adding 7.5 mM benzyl viologen. **Black:** without activation, Fdh (35 nM) was incubated with 7.5 mM benzyl viologen in 60 mM Tris-HCl buffer pH 8.0 and 133 mM  $\beta$ -mercaptoetanol at 37 °C. The reaction was started adding 10 mM sodium formate. All assays were performed in Argon atmosphere in stoppered quartz cell.

67

**Figure IV.5| Michaelis-Menten behavior from Fdh.** Michaelis-Menten plots of the steady-state kinetic assays performed in the three Fdh enzymes studied. Black and red lines are the fitting of the experimental values obtained with  $^1\text{HCOO-Na}$  (squares) and  $^2\text{HCOO-Na}$  (circles) as substrates.

68

**Figure IV.6| Fdh active site structures.** Optimized structure of the active site of the models of Fdh assuming  $\text{Mo}^{4+}$ ,  $\text{Mo}^{5+}$  and  $\text{Mo}^{6+}$  formal oxidation states.

70

<b>Figure IV.7  Enzyme activation.</b> General overview of the energies involved in the activation of the enzyme (the total charge and multiplicity of the system are between brackets).	72
<b>Figure IV.8  Formation of the ES complex.</b> General overview of the energies involved in the formation of the ES complex (the total charge and multiplicity of the system is between brackets).	73
<b>Figure IV.9  SeCys dissociation.</b> General overview of the energies involved in the dissociation of the SeCys (the total charge and multiplicity of the system is between brackets).	75
<b>Figure IV.10  Proton transfer.</b> General overview of the energies involved in the Proton transfer (the total charge and multiplicity of the system are between brackets).	76
<b>Figure IV.11  Active site after proton transfer.</b> Product obtained after finishing the proton transfer from the formate to the SeCys140.	77
<b>Figure IV.12  Carbon dioxide release.</b> The mechanism of the carbon dioxide release prior (top) and after (bottom) the electron transfer (the total charge and multiplicity of the system is enclosed in brackets).	78
<b>Figure IV.13  Active site regeneration.</b> Regeneration of the active site to the initial oxidized state (the total charge and multiplicity of the system are between brackets).	80
<b>Figure IV.14  Turnover in presence of formate.</b> Formate binding to an intermediate species produced after oxidation of the active site (the total charge and multiplicity of the system are between brackets).	81
<b>Figure IV.15  Global scheme of formate oxidation by Fdh.</b> Global view of the catalytic mechanism of formate dehydrogenase.	83
<b>Figure IV.16  Mo- and W-dependent Fdhs active site-core.</b> Close-up view of the active site of Mo- and W-dependent formate dehydrogenases. The H-S <sub>i</sub> distance is written in red and the relevant aminoacids in black. Atom color code: white, hydrogen; yellow, sulfur; dark yellow, selenium; cyan, molybdenum.	86
<b>Figure V.1  Comparison of the Nap and Fdh active site-core.</b> Superposition of W-Fdh from <i>D. gigas</i> (red) and NapA (blue) from <i>D. desulfuricans</i> (PDBs: 1H0H and 2JIM).	93
<b>Figure V.2  Normalized initial rates vs. nitrate concentration.</b> (■): Fdh from <i>D. desulfuricans</i> (35 nM); (▲): Fdh from <i>D. gigas</i> (35 nM); (●): Fdh from <i>D. alaskensis</i> (10 nM). Conditions used as described in section V.3.5, 10 mM of formate was used.	96

**Figure V.3| Inhibition type characterization of Fdh from *D. desulfuricans* by nitrate.** Direct linear plot showing competitive inhibition. Black and red lines correspond to the experiments in absence and presence of 20 mM of nitrate, respectively; Inhibition constant ( $K_{ic}$ ) determined by Rivas *et al* [16]. 97

**Figure V.4 Inhibition type characterization of *Dg* Fdh by nitrate.** (a) Direct linear plot showing competitive inhibition. Black and red lines correspond to the experiments in absence and presence of 10 mM of nitrate, respectively; (b) Dixon plot used to calculate  $K_{ic}$ . (c) Parallel pattern of Cornish-Bownden plot showing competitive inhibition. Formate concentrations used: (■) 500  $\mu$ M, (▲) 250  $\mu$ M, (●) 100  $\mu$ M and (◆) 50  $\mu$ M. 98

**Figure V.5| Inhibition type characterization of Fdh from *D. alaskensis* by nitrate.** (a) Direct linear plot showing competitive inhibition. Black and red lines correspond to the experiments in the presence or absence of 5 mM of nitrate, respectively; (b) Dixon plot used to calculate  $K_{ic}$ . (c) Parallel pattern of Cornish-Bownden plot showing competitive inhibition. Formate concentrations used: (■) 250  $\mu$ M, (▲) 50  $\mu$ M, (●) 20  $\mu$ M and (◆) 12.5  $\mu$ M. 99

**Figure V.6| Normalized initial rates vs. azide concentration.** (■): Fdh from *D. desulfuricans* (35 nM); (▲): Fdh from *D. gigas* (35nM); (●): Fdh from *D. alaskensis* (10 nM). Conditions used as described in section V.3.5, 10 mM of formate was used. 101

**Figure V.7| Characterization of the inhibition type by azide for the *Dd* Fdh.** (a) Direct linear plot showing mixed inhibition. Black and red lines correspond to the experiments in absence and presence of 0.5 mM of azide, respectively; (b) Inhibition constants ( $K_{ic}$  and  $K_{iuc}$ ) determined by Rivas *et al* [2,16]. 102

**Figure V.8| Characterization of the inhibition type by azide for the *Dg* Fdh.** (a) Direct linear plot showing mixed inhibition. Black and red lines correspond to the experiments in absence and presence of 10 mM of azide, respectively; (b) Dixon plot used to calculate  $K_{ic}$ . (c) Cornish-Bownden plot used to calculate  $K_{iuc}$ . Formate concentrations used: (■) 500  $\mu$ M, (▲) 250  $\mu$ M, (●) 100  $\mu$ M and (◆) 50  $\mu$ M. 103

**Figure V.9| Characterization of the inhibition type by azide for the *Da* Fdh.** (a) Direct linear plot showing mixed inhibition. Black and red lines correspond to the experiments in absence and presence of 0.5 mM of azide, respectively; (b) Dixon plot used to calculate  $K_{ic}$ . (c) Cornish-Bownden plot used to calculate  $K_{iuc}$ . Formate concentrations used: (■) 250  $\mu$ M, (▲) 50  $\mu$ M, (●) 25  $\mu$ M and (◆) 15  $\mu$ M. 104

**Figure V.10| Normalized initial rates vs. cyanide concentration.** (■): Fdh from *D. desulfuricans* (35 nM); (▲): Fdh from *D. gigas* (35 nM); (●): Fdh from *D. alaskensis* (35 nM). Conditions used as described in section V.3.5, 10 mM of formate was used 106

**Figure V.11| Characterization of the inhibition type by cyanide for the *Dd* Fdh.** Direct linear plot showing mixed inhibition. Black and red lines correspond to the experiments in absence and presence of 2.5 mM of cyanide, respectively; Inhibition constants ( $K_{ic}$  and  $K_{iuc}$ ) determined by Rivas *et al* [2,16]. 107

**Figure V.12| Aminoacids alignment of Fdhs  $\alpha$  subunits.** FdhDg:  $\alpha$  subunit from *D. gigas*; FdhDa:  $\alpha$  subunit from *D. alaskensis*; FdhDd:  $\alpha$  subunit from *D. desulfuricans*; light grey: twin arginine motif; light yellow: conserved SeCys; light blue: conserved residues probably involved in enzymatic catalysis; ▼: signal peptide cleavage site; ·: cysteines motifs involved in the coordination of [4Fe-4S] clusters; (\*): identity; (:): strongly similar; and (.) weekly similar. 110

**Figure V.13| Aminoacids alignment of Fdhs  $\beta$  subunits.** FdhDg:  $\beta$  subunit from *D. gigas*; FdhDa:  $\beta$  subunit from *D. alaskensis*; FdhDd:  $\beta$  subunit from *D. desulfuricans*; ●, ●, and ●: cysteine motifs involved in the FeSII, FeSIII and FeSIV cluster binding; (\*): identity; (:): strongly similar; and (.) weekly similar. 111

**Figure V.14| Fdhs active sites overlapped.** Fdhs active sites with aminoacids from neighborhood from *D. gigas* (black), *D. alaskensis* (green) and *D. desulfuricans* (red). The overlay was done using the structure of Fdh from *D. gigas* [19] as support. 115

**Figure VI.1| Schematic representations of the several Mo ion coordination sphere proposed by several authors based on different experimental evidences.** X-ray crystallography: (A), (B), (D) and (E). DFT calculations: (C). XAS spectroscopy: (F). 121

**Figure VI.2| CW-EPR spectra obtained in *Dd* Fdh samples (200  $\mu$ M) in presence or absence of the competitive inhibitor azide.** A) Formate-reduced *Dd* Fdh incubated with 3 mM sodium azide in H<sub>2</sub>O-buffer. B) As A) but in D<sub>2</sub>O-buffer. C) Formate-reduced *Dd* Fdh in H<sub>2</sub>O-buffer. D) As C) but in D<sub>2</sub>O-buffer. Measurement conditions: Microwave frequency, 9.65 GHz; Modulation frequency, 100 kHz, Modulation amplitude, 5Gpp; Microwave power, 2 mW; Temperature, 100 K. 123

**Figure VI.3| 3D view of the structural model used to predict EPR parameters of the *formate* Mo(V) species.** Predicted  $g$ -values and hfc constants of the exchangeable proton bound to the -SH group are written next to the model. 128

**Figure VI.4: 3D view of the structural model used to predict EPR parameters of the *azide* (2.094) Mo(V) species.** Predicted  $g$ -values and hfc constants of the exchangeable proton are written next to the model. The bond lengths specified in the model were frozen according to the EXAFS data. 130

# **Chapter I**

*General introduction*

## **I.1 Metals in proteins**

Proteins are the most versatile macromolecules in living systems and have crucial functions in essentially all biological processes. They function as catalysts, transport and store other molecules, provide mechanical support and immune protection, generate movement, transmit nerve impulses, and control cell growth and differentiation. The entire set of proteins of a living cell is called the proteome. Although the genetic information coding for the proteome is stored in the form of DNA within the genome, is the proteome that determines which and at which levels proteins should be expressed under given conditions in a given cell type [1].

It has been estimated that about one third of all proteins bind one or more metal ions as prosthetic groups. A systematic bioinformatics study of 1,371 enzymes with known three-dimensional structures showed that 47% require metals from which 41% contain metals at their catalytic centers [2]. Metalloenzymes occur in all six Enzyme Commission Classes (E.C.C.), accounting for 44% of oxidoreductases, 40% of transferases, 39% of hydrolases, 36% of lyases, 36% of isomerases and 59% of ligases. Figure I.1A shows the frequency of metals in proteins structures. Magnesium is the most prevalent metal in metalloenzymes being often involved in loose partnerships with phosphate-containing substrates such as ATP. Since this metal is sometimes interchangeable with manganese, the frequency of Mn *in vivo* may be overestimated [3]. A classification of the principal type of enzymes that incorporate metals showed in figure I.1B reveals that iron (81%), copper (93%) and molybdenum plus tungsten (81%) are most commonly used as conduits for electrons in oxidoreductases [2]. These are the so called redox active elements because they occur in various stable oxidations states.

A variety of transition metals have found their way into biological systems. Although only a minor constituent of the earth's crust, molybdenum is readily available to biological systems because of the solubility of molybdate salts in water. Indeed, molybdenum is the most abundant transition metal in seawater and, since the modern oceans resemble the primordial soup from which life arose, it is not surprising that molybdenum has been incorporated widely into biological systems [4]. The only life forms that do not require molybdenum use tungsten instead, which lies immediately below molybdenum in the periodic table. Probably due to the hot, anaerobic conditions of the early Earth, tungsten might have been the first of these elements to be acquired by living organisms [5]. Once, low-valent tungsten sulfides are more soluble in aqueous

solutions and thus would be more available in anaerobic and highly reducing environment [4].

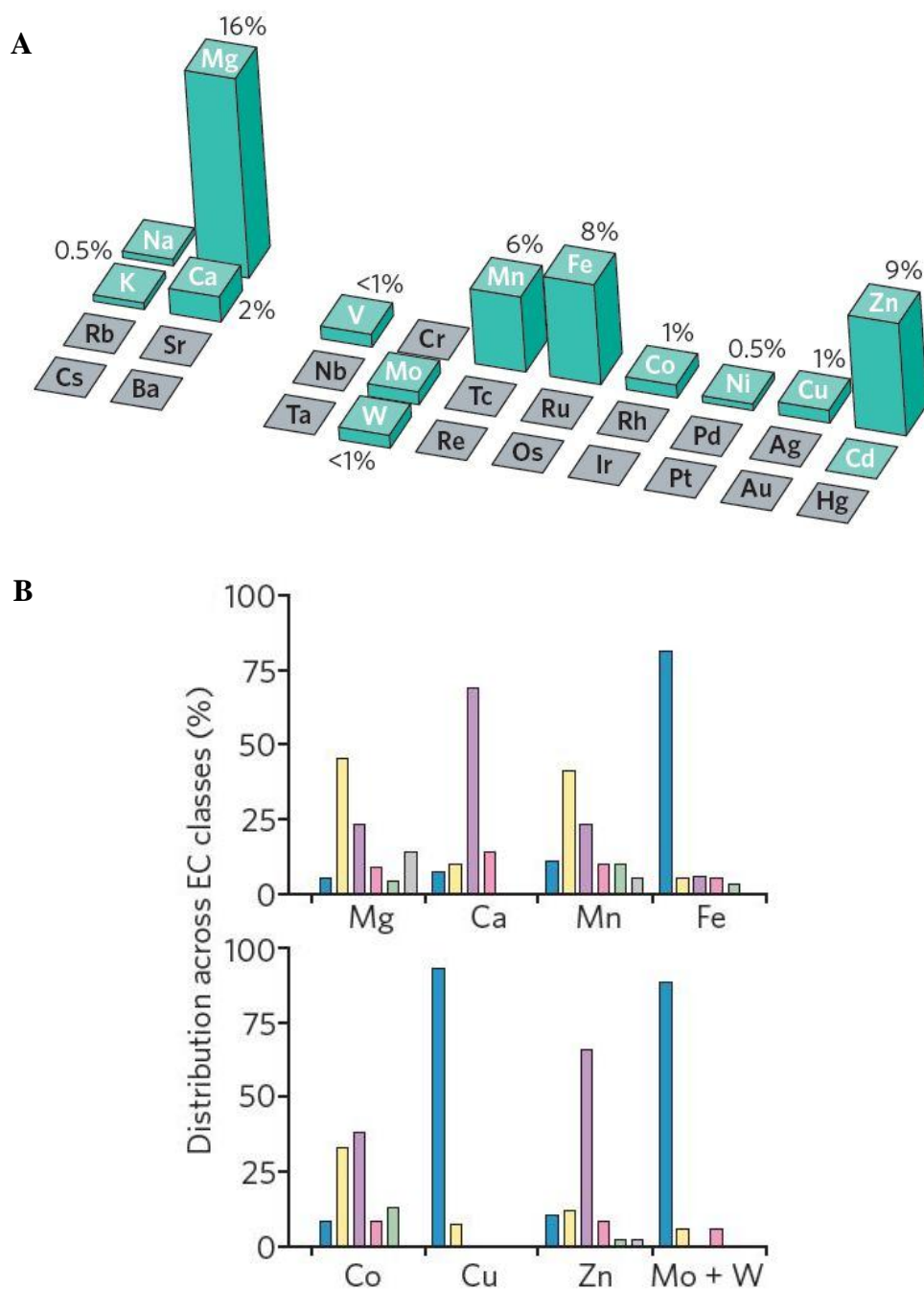


**Figure I.1| Metals used in catalysis.** **A**, The elements used as cofactors by enzymes are shown in green. The height of each column represents the proportion of all enzymes with known structures using the respective metal. A single enzyme use cadmium (carbonic anhydrase from *T. weissflogii* [6]). **B**, The proportion of proteins using the indicated metals that occur in each of the six enzyme classes: oxidoreductases (EC 1), blue; transferases (EC 2), yellow; hydrolases (EC 3), purple; lyases (EC 4), pink; isomerases (EC 5), green; ligases (EC 6), grey. EC, Enzyme Commission. Figures were taken from reference [3].

Both molybdenum and tungsten are redox-active under physiological conditions (ranging between oxidation states VI, V and IV) and this chemical versatility make them useful in biological systems [4]. The physiological roles of enzymes containing these metals are fundamental and include the catalysis of key steps in carbon, nitrogen and sulfur metabolism [7].

## **I.2 Cell biology of molybdenum and tungsten**

Molybdenum and tungsten are widely distributed in biology. Molybdenum-containing enzymes are present in bacteria, fungi, algae, plants and animals [8,9], whereas the majority of the tungsten-containing enzymes purified to date are found in anaerobic organisms of Archaea and Bacteria [5].

On the basis of cofactor composition and catalytic function, molybdenum and tungsten dependent enzymes can be grouped into two categories: bacterial nitrogenases containing an FeMoco in the active site [10], and pterin-based molybdenum/tungsten enzymes [4,7].

Molybdenum and tungsten are bioavailable as molybdate ( $\text{MoO}_4^{2-}$ ) and tungstate ( $\text{WO}_4^{2-}$ ) oxoanions, respectively. Once these oxoanions enters inside the cell (see section I.2.1), they are incorporated into metal cofactors by complex biosynthetic machineries (see section I.2.2).

### **I.2.1 Cellular uptake**

The cellular transport systems for oxoanions like tungstate, molybdate and sulfate have been studied and described for many organisms. In particular, the uptake mechanisms of these oxoanions have been deeply characterized in *E. coli* [11]. All these transport systems are members of the adenosine triphosphate (ATP) binding cassette (ABC) transporter group. According to the currently accepted model for cellular Mo uptake, molybdate is captured by ModA, a periplasmic molybdate-binding protein that transfer the metal oxo-ion to ModB, which is a transmembrane channel. At the cytoplasmic side ATP is hydrolyzed to ADP and  $\text{P}_i$  in ModC, which generates the energy necessary to complete the transport of molybdate into the cell cytoplasm. Additional proteins encoded by the *mod* operon have functions in intracellular molybdate binding and regulation of gene expression that depend on the extra- and intracellular concentration



of the metal. ModA is also able to bind tungstate with a similar affinity as to molybdate [12,13]. For tungsten, two ABC-type transporters are known: TupABC and WtpABC [13]. The TupABC system is specific for tungstate and was identified in *E. acidaminophilum* [14]. More recently, the structurally different WtpABC transporter was reported in the hyperthermophilic archaeon *P. furiosus* [15].

### **I.2.2 Biosynthesis of the cofactor**

Molybdenum and tungsten association with enzymes occur in a similar cofactor, which consist of one or two tricyclic pterin moieties usually referred as molybdopterin, tungstopterin or pyranopterin. The pathway of Mo-cofactor (Moco) biosynthesis has been extensively studied in prokaryotes (*E. coli*) as well as eukaryotes (*Arabidopsis thaliana* and *Homo sapiens*) and appears to be highly conserved [16]. The pathway of W-cofactor (Wco) biosynthesis is thought to be similar to the pathway of Moco biosynthesis, at least up to the step of the metal insertion. The support of this hypothesis is that homologues of almost all genes that have an assigned function in the Moco biosynthetic pathway are also present in the genomes of organisms that incorporates W instead of Mo in the enzymes active sites.

The first model of Moco synthesis was based on *E. coli* data [17]. Three operons and one gene have been identified to be involved in the Moco biosynthesis in this organism: *moaABCDE*, *mobAB*, *moeAB* and *mogA*, respectively. Among the ten proteins involved in the biosynthesis of Moco, eight have an assigned function and two remain to be demonstrated. Figure I.2 schematizes the Moco biosynthesis pathway including the function of each one of this proteins.

The process starts with the conversion of guanosine triphosphate (GTP) into cyclic pyranopterin monophosphate (cPMP), previously identified as precursor Z. This step is catalyzed by two proteins: MoaA and MoaC (Cnx2 and Cnx3 for plants; MOCS1A and MOCS1B for human) [18]. The expression of these two proteins is regulated by ModE [13]. Subsequently, Metal-binding pterin (MPT) is synthesized from cPMP by MPT synthase, which consists in a dimer of heterodimers of MoaD/MoaE (Cnx7 and Cnx6 for plants; MOCS2B and MOCS2A for human). MoaD needs to be previously activated by MoeB (Cnx5 in plant; MOCS3 in human) [19].

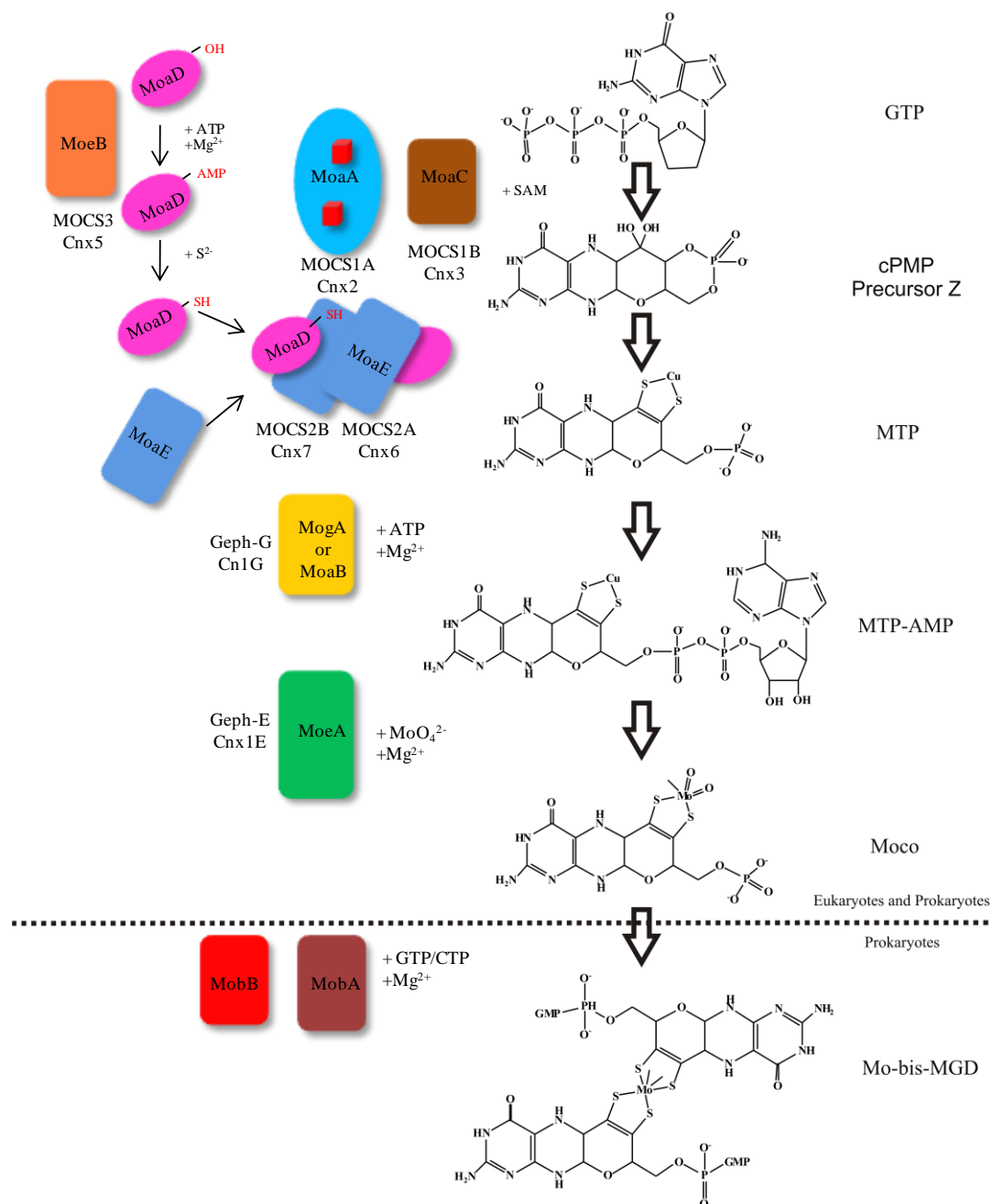


**Figure I.2| Biosynthesis of the Pyranopterin-based molybdenum cofactors.** Schematic overview of the molybdenum cofactor biosynthesis adapted from reference[12] and based on data derived from studies in *E. coli*, plants and humans. Abbreviations of the intermediates are written in bold on the right side of their structures, and the enzymes are on the left side of the arrows. The fifth step present only in prokaryotes. For MPT and MPT-AMP, the dithiolate sulfurs are bonded to a Cu, because in the crystal structure of plant Cnx1G was found a copper ion in that place.

The next steps involve the coordination of the metal atom (Mo or W) to the dithiolene sulfurs replacing the Cu atom present in the MPT. The proteins MoeA and MogA (Cnx1E and Cnx1G for plant; Geph-E and Geph-G for human) catalyze these steps, and very recently also MoaB was found to be involved in this stage of the cofactor synthesis

[20]. The proteins MogA and MoaB catalyse the activation of MPT by adenylation with Mg-ATP [21,22]. The trimeric MogA proteins are commonly found in bacteria and eukaryotes, whereas the hexameric MoaB proteins are mostly found in archaea and in some bacteria though believed to be specific for the biosynthesis of the tungsten cofactor [20]. Subsequently, MoeA is thought to bind the adenylylated MPT (MPT-AMP) produced after reaction with MogA or MoaB and in the presence of molybdate and/or tungstate the MPT-AMP complex is hydrolyzed. At this step, molybdenum or tungsten displaces the Cu ion coordinated to the dithiolene sulfurs, and the AMP is released. Because Moco is deeply buried within the holoenzymes, it needs to be incorporated before the completion of folding and oligomerization of enzyme subunits domains in the presence of chaperones [12,13].

As a final maturation step (only in prokaryotes), guanosine monophosphate (GMP) or cytidine monophosphate (CMP) can be attached (phosphoester condensation from GTP and CTP) to the MoCo, forming molybdopterin guanosine/cytidine dinucleotide (MGD/MCD) cofactor. This reaction is catalyzed by MobA and MobB [23]. For some prokaryotes enzymes the coupling of a second pyranopterin dinucleotide cofactor can be required, leading to the formation of the Mo/W-*bis*-pyranopterin dinucleotide cofactor. The pathway that lead to the formation of this type of cofactors still remains unclear and needs to be more studied [13].

Eukaryotic molybdenum hydroxylases (e.g. xanthine oxidase, aldehyde oxidase) harbor the Moco in the mature protein, but require the addition of a terminal sulfido ligand to the molybdenum to get enzymatic activity. This step is catalyzed by Moco sulfurilase (Aba3 in plants and MOCOS in humans) [12,24]. Among prokaryotes, no Moco sulfurilases homologues to eukaryotic have been found. So far, only one exception was reported and corresponds to the XdhC which is a specific chaperone coded by the *R. capsulatus* genome found to perform Moco sulfurilation of xanthine dehydrogenase [25].

### **I.2.3 Molybdenum cofactor deficiency**

Moco biosynthesis is a relevant target of study because many steps of the synthesis still remain unclear and the specificity for Mo or W is not yet understood. The Moco biosynthesis is an important metabolic pathway in cells, for example, human Moco deficiency (MocoCD) results in complete loss of sulfite oxidase, xanthine oxidase and aldehyde oxidase activity. This disease is characterized by progressive neurological damage, leading to early childhood death in most cases. Symptoms are mainly caused by deficiency of sulfite oxidase protecting the organs (in particular the brain) from elevated concentrations of toxic sulfite [12]. The biochemical explanation behind this is that sulfite oxidase catalyzes the last step in the oxidative degradation of sulfur-containing amino acids and lipids. Localized in the intermembrane space of mitochondria, this enzyme catalyzes the oxidation of sulfite to sulfate. Under conditions of Moco or sulfite oxidase deficiency, sulfite accumulates in the plasma and serum, crosses the blood-brain barrier and rapidly triggers neuronal death [12].

An animal model, in which the gene encoding Mocs1 (a MoaA homologue) was deleted, has been used to study the Moco cofactor deficiency [26]. Homozygous mice displayed a severe phenotype that reflects all biochemical characteristics of human Moco-deficient patients. They failed to thrive, and died within the first 12 days of life. Mice treated with cPMP purified from *E. coli* [27], gained weight and reached the adulthood and fertility like their wild-type analogues. When the delivery of cPMP by injections stops, Mocs-1-knockout mice die within 10-14 days. These promising results are already being applied in clinical assays in humans [12].

## **I.3 Molybdenum and tungsten enzymes**

In contrast to the multinuclear iron-molybdenum clusters found in bacterial nitrogenases [10] and copper-molybdenum sites found in carbon monoxide dehydrogenase from *O. carboxidovorans* [28], the active sites of all other well-characterized molybdenum- and tungsten-containing enzymes are mononuclear [8]. In these mononuclear molybdenum containing enzymes, the metal coordinated by one or two cis-dithiolene groups plus additional terminal oxo/hydroxo and/or sulfido groups or side chains of serine, cysteine, selenocysteine or aspartate residues in a diversity of arrangements. For most of the molybdenum- and tungsten-dependent enzymes the catalyzed reaction is an oxo-transfer

reaction coupled to electron-transfer between substrate and other cofactors such as iron-sulfur centers, hemes or flavins.

### **I.3.1 Categories and general features of mononuclear Mo/W containing enzymes**

Based on X-ray structural data, primary sequence alignments, spectroscopic and biochemical characteristics, molybdenum- and tungsten-containing enzymes can be grouped in four broad families (figure I.3) [7]:

1) The xanthine oxidase family: can harbor one MCD or MPT that provides the only attach of the Mo ion to the protein. The Mo coordination sphere can be completed by oxygen (oxo, hydroxo) and sulfur (sulfido) ligands.

2) The sulfite oxidase family (and eukaryotic nitrate reductases): can harbor one MPT that together with a sulfur atom from a cysteine sidechain attach the Mo ion to the protein. The coordination sphere is completed by two oxygenic species (oxo, hydroxo).

3) The DMSO reductase family: can bind two MGD molecules that provide four sulfur ligands to the Mo/W ion arising from the two dithiolene groups. In addition, the Mo/W can bind oxygen, sulfur or selenium from aminoacid sidechains (O-Ser, O-Asp, S-Cys, Se-Cys). The Mo coordination sphere is completed with oxygen (oxo, hydroxo) or sulfur (sulfido) atoms.

4) The tungsten aldehyde oxidoreductase family: can bind two MPT molecules that in a similar arrangement to the DMSO reductase family. The W coordination sphere is completed by two oxygen atoms (oxo, hydroxo). This family of proteins includes a few enzymes within the aldehyde ferredoxin oxidoreductase (AOR) from *P. furiosus* [29] is the most representative example.

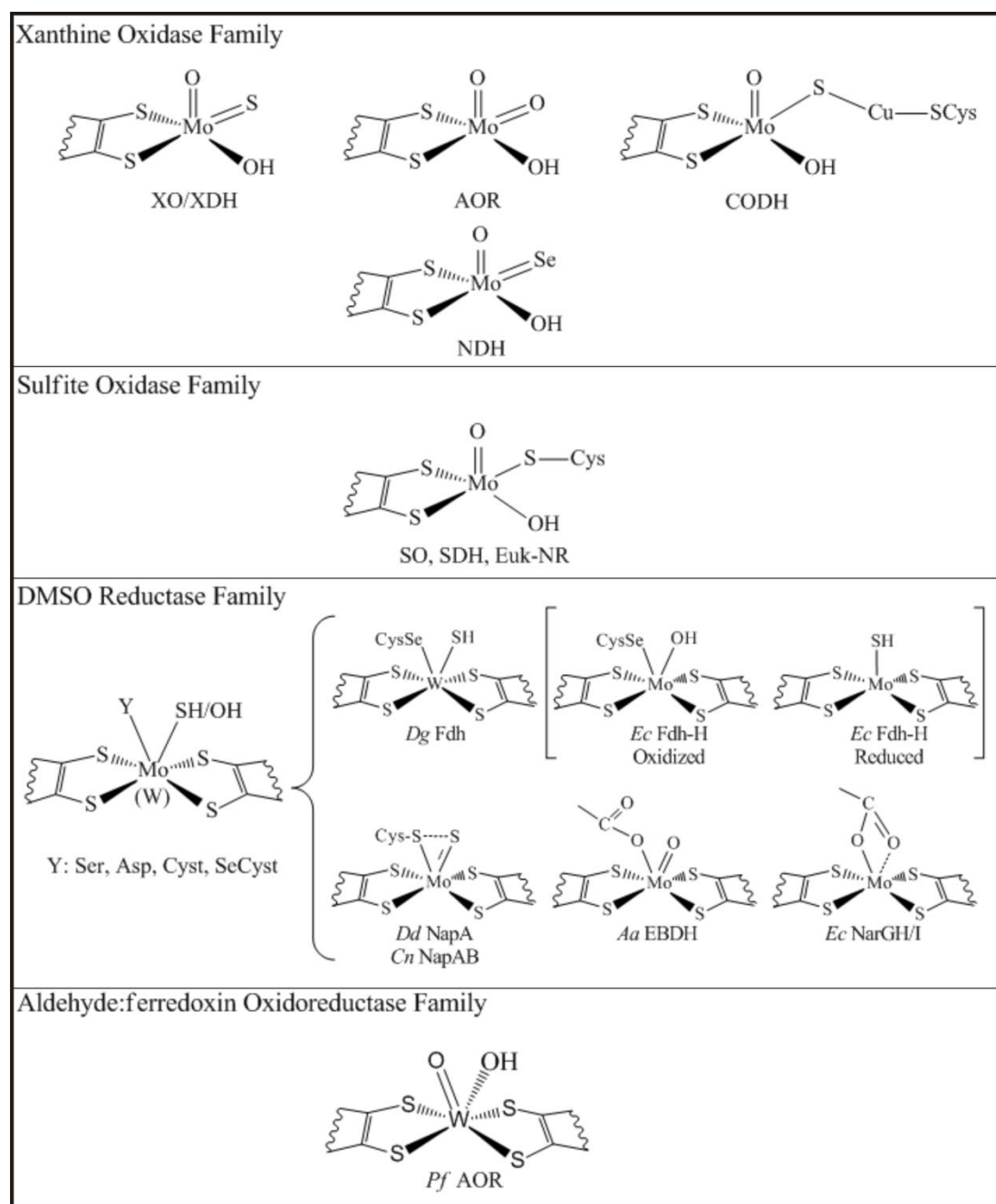


**Figure I.3| Active-site structures of the different families molybdo- and tungsto-pterins containing enzymes.** XO/XDH: xanthine oxidase/xanthine dehydrogenase; AOR: aldehyde oxidoreductase; CODH: carbon monoxide dehydrogenase; NDH: Nicotinate dehydrogenase; SO: sulfite oxidase; SDH: sulfite dehydrogenase; Euk-NR: eukaryotic nitrate reductase; *Dg Fdh*: *Desulfovibrio gigas* formate dehydrogenase; *Ec Fdh-H*: *Escherichia coli* formate dehydrogenase H; *Dd NapA*: *Desulfovibrio desulfuricans* ATCC 27774 periplasmatic nitrate reductase A; *Cn NapAB*: *Cupriavidus necator* periplasmatic nitrate reductase AB; *Aa EBDH*: *Aromateleum aromaticum* ethylbenzene dehydrogenase; *Ec NarGH/I*: *Escherichia coli* nitrate reductase GH/nitrate reductase GHI; *Pf AOR*: *Pyrococcus furiosus* aldehyde ferredoxin:oxidoreductase.

### **I.3.1.1 The xanthine oxidase family**

Enzymes of the xanthine oxidase family are the best characterized mononuclear Mo-containing enzymes. With a few exceptions, they catalyze the oxidative hydroxylation of a diverse range of aldehydes and aromatic heterocycles in reactions that involve the cleavage of a C-H and the formation of a C-O bond:



Members of this family can be found distributed within eukaryotes and prokaryotes. Xanthine dehydrogenase (XDH) [30] is the key enzyme in the catabolism of purines, catalyzing the conversion of hypoxanthine to xanthine, and xanthine to uric acid. XDH can be converted to xanthine oxidase (XO) by proteolysis and cysteines oxidation. XO also catalyzes the reactions of purine catabolism but is not NADH-dependent and reactive oxygen species (ROS) are formed as by-products of the reaction [31]. The mammalian aldehyde oxidase is also an important enzyme involved in metabolism of several aldehyde compounds and the biotransformation of xenobiotics [32].

Enzymes belonging to the XO family have the Mo-MPT cofactor without any covalent attachment to the polypeptide chain. They are organized either as homodimers, with several redox-active cofactors placed within a single subunit, or as multi-subunit enzymes. In the case of a single subunit structure (mammalian xanthine oxidase and aldehyde oxidase (AOX)), two [2Fe-2S] centers are located in the N-terminal domain (~20kDa), followed by the flavin domain (~40kDa) and finally the C-terminal domain (90kDa) that hold the Moco. The prokaryotic aldehyde oxidoreductases isolated from sulfate reducers like *D. gigas* and *D. desulfuricans* [33,34] are very similar to the XO and AOX but they lack the flavin domain.

In multi-subunit structures (e.g. CO dehydrogenase from *Oligotropha carboxidovorans* [28] and quinoline oxidoreductase from *Pseudomonas putida* [35]), the redox centers are found within independent subunits ( $\alpha$ ,  $\beta$  and  $\gamma$ ). The  $\alpha$  subunit harbors the two [2Fe-2S] centers, the  $\beta$  subunit a flavin and the  $\gamma$  subunit the Moco. The CO dehydrogenase is an interesting and unique case because is a MPT binding enzyme that has a binuclear Mo-S<sub>μ</sub>-Cu active site, but owing the structural similarities still belongs to the XO family.

### **I.3.1.2 The sulfite oxidase family**

The members of this family include not only sulfite oxidases from plants, animals and bacteria but also the eukaryotic nitrate reductases [36]. These assimilatory nitrate reductases catalyze the first and rate-limiting step of nitrate assimilation in plants, algae and fungi, and are completely different from the bacterial nitrate reductases that belong to the DMSO reductase family.

Three different sulfite-oxidizing subfamilies are known: sulfite oxidase (SO) in animals, SO in plants, and sulfite dehydrogenase (SDH) in bacteria. The animal SO catalyzes the last reaction in the oxidative degradation of the sulfur containing amino acids cysteine and methionine and is critical in transforming the toxic sulfite into the more soluble sulfate anion that can be excreted. Similarly, the plant SO is responsible for detoxifying excess sulfite produced during sulfur assimilation. In bacteria, e.g. *Sarkeya novella* [37], SDH has an important role oxidizing the sulfite formed during dissimilatory oxidation of reduced sulfur compounds.

In contrast to the XO family, the polypeptide chain coordinates directly to the Mo ion by a cysteinyl residue. The animal SO are homodimeric and bind Moco and one *b*-type heme in different domains. The plants SO are also homodimeric, harbor the Moco domain but lacks the heme domain. The most representative bacterial enzyme is heterodimeric periplasmic sulfite dehydrogenase (SorAB) which contains a Moco and one *c*-type heme in  $\alpha$  and  $\beta$  subunits, respectively [37]. Some of these enzymes occur as monomers or dimers and lack the heme groups [38].

### **I.3.1.3 The DMSO reductase family**

The most widespread family of Mo and W enzymes is the dimethyl sulfoxide reductase (DMSOr) family which was divided into subfamilies I, II and III [7]. Its members are found in prokaryotes and include diverse enzymes such as dissimilatory nitrate reductases and formate dehydrogenases (Fdhs) (subfamily I) [39]; respiratory nitrate reductases [40,41] and ethylbenzene dehydrogenase [42] (subfamily II); DMSO reductase [43,44] and trimethylamine N-oxide (TMAO) reductase [45,46] (subfamily III). Other members from this family with singular characteristics are the arsenite oxidase [47,48] and the W-containing acetylene hydratase [49]. Despite the fact that arsenite oxidase has high structural similarity with other members of the family, its active site does not present an amino acid side chain coordinating the W atom.



With some exceptions, members of the DMSOr family catalyze the transfer of an oxygen atom to or from the substrate. The exceptions are the Fdhs, which catalyze the oxidation of formate to carbon dioxide by cleaving a C-H bond. In addition, the acetylene hydratase from *Pelobacter acetylenicus* [49] catalyzes a non-redox reaction, that is, the hydration of acetylene to acetaldehyde. This process is part of an anaerobic degradation pathway of unsaturated hydrocarbons.

The enzymes from DMSOr family present high degree of similarity in the overall polypeptide fold of crystal structures. However, there are some variations in the active site, not only at the metal coordination sphere, but also with the surrounding amino acids residues. These slight but important differences at the catalytic sites of the different enzymes can explain the remarkable diversity of functions performed by enzymes of the DMSOr family. The amino acid that coordinates the molybdenum or tungsten atom differs among the several enzymes of the family: cysteine in the periplasmic nitrate reductase and acetylene hydratase, selenocysteine in Fdh, aspartate in the membrane-bound respiratory nitrate reductases and ethylbenzene dehydrogenase, and a serine in DMSO reductase and TMAO reductase. Only in the arsenite oxidase the Mo ion has no ligands from the polypeptide chain.

To date, it is known that only Fdhs [50] and DMSO reductases [51] are capable of incorporating either molybdenum or tungsten at their active sites.

#### **I.4 Subject and objectives of this thesis**

This thesis deals with formate dehydrogenases isolated from sulfate reducing bacteria (SRB), namely *Desulfovibrio* species. These organisms can use formate, the product of the reaction catalyzed by pyruvate formate lyase, as carbon source and electron donor [52]. The protons released in formate oxidation by Fdh will contribute for a proton gradient and subsequently energy production.

The active site of Fdh comprises a metal ion (Mo or W) coordinated to five sulfur atoms and a selenium. The chemistry of transition metals like Mo and W in biological systems is not yet well understood. Also, the preference of some Fdhs to incorporate Mo or W to perform the catalysis is a phenomenon that lies in the shade for microbiologists.

The main goal of this thesis is to understand how Fdh performs the catalysis. To obtain information about this issue, these are some of the questions that were discussed along

this work: How substrate binds to the active site? What is the role of the Se in the catalytic mechanism? How is the catalytic mechanism of formate oxidation? Why different active sites structures are proposed in the literature for the same Mo species? Why some Fdhs prefer incorporate Mo and other W in the active site?

The studies described in this work covers a large set of techniques:

- Real Time PCR, purification and biochemical characterization methods were used to obtain information about the influence of Mo and W on the Fdh and metal transport systems expression.
- Kinetics studies and DFT calculations were used to characterize the enzyme by determining the kinetic parameters and to understand the reaction mechanism.
- DFT calculations were also used to reconcile the available structural and spectroscopic data obtained in Mo and W containing Fdhs.

## **I.5 References**

- 1 Berg, J. M., Tymoczko, J. L. & Stryer, L. Biochemistry. 5th Edition edn, (W. H. FREEMAN AND COMPANY, 2002).
- 2 Andreini, C., Bertini, I., Cavallaro, G., Holliday, G. L. & Thornton, J. M. Metal ions in biological catalysis: from enzyme databases to general principles. *J Biol Inorg Chem* 13, 1205-1218, (2008).
- 3 Waldron, K. J., Rutherford, J. C., Ford, D. & Robinson, N. J. Metalloproteins and metal sensing. *Nature* 460, 823-830, (2009).
- 4 Hille, R. Molybdenum and tungsten in biology. *Trends Biochem Sci* 27, 360-367, (2002).
- 5 Johnson, M. K., Rees, D. C. & Adams, M. W. Tungstoenzymes. *Chem Rev* 96, 2817-2840, (1996).
- 6 Lane, T. W., Saito, M. A., George, G. N., Pickering, I. J., Prince, R. C. & Morel, F. M. M. Biochemistry A cadmium enzyme from a marine diatom. *Nature* 435, 42-42, (2005).
- 7 Romao, M. J. Molybdenum and tungsten enzymes: a crystallographic and mechanistic overview. *Dalton Trans*, 4053-4068, (2009).
- 8 Hille, R. The Mononuclear Molybdenum Enzymes. *Chem Rev* 96, 2757-2816, (1996).

- 9 Williams, R. J. P. & da Silva, J. J. R. F. The involvement of molybdenum in life. *Biochem Biophys Res Commun* 292, 293-299, (2002).
- 10 Burgess, B. K. & Lowe, D. J. Mechanism of Molybdenum Nitrogenase. *Chem Rev* 96, 2983-3012, (1996).
- 11 Rech, S., Deppenmeier, U. & Gunsalus, R. P. Regulation of the molybdate transport operon, modABCD, of *Escherichia coli* in response to molybdate availability. *J Bacteriol* 177, 1023-1029, (1995).
- 12 Schwarz, G., Mendel, R. R. & Ribbe, M. W. Molybdenum cofactors, enzymes and pathways. *Nature* 460, 839-847, (2009).
- 13 Bevers, L. E., Hagedoorn, P. L. & Hagen, W. R. The bioinorganic chemistry of tungsten. *Coordination Chem Rev* 253, 269-290, (2009).
- 14 Makdessi, K., Andreesen, J. R. & Pich, A. Tungstate Uptake by a highly specific ABC transporter in *Eubacterium acidaminophilum*. *J Biol Chem* 276, 24557-24564, (2001).
- 15 Bevers, L. E., Hagedoorn, P. L., Krijger, G. C. & Hagen, W. R. Tungsten transport protein A (WtpA) in *Pyrococcus furiosus*: the first member of a new class of tungstate and molybdate transporters. *J Bacteriol* 188, 6498-6505, (2006).
- 16 Schwarz, G. Molybdenum cofactor biosynthesis and deficiency. *Cell Mol Life Sci* 62, 2792-2810, (2005).
- 17 Rajagopalan, K. V. & Johnson, J. L. The pterin molybdenum cofactors. *J Biol Chem* 267, 10199-10202, (1992).
- 18 Wuebbens, M. M. & Rajagopalan, K. V. Investigation of the early steps of molybdopterin biosynthesis in *Escherichia coli* through the use of in vivo labeling studies. *J Biol Chem* 270, 1082-1087, (1995).
- 19 Schwarz, G. & Mendel, R. R. Molybdenum cofactor biosynthesis and molybdenum enzymes. *Annu Rev Plant Biol* 57, 623-647, (2006).
- 20 Bevers, L. E., Hagedoorn, P. L., Santamaria-Araujo, J. A., Magalon, A., Hagen, W. R. & Schwarz, G. Function of MoaB proteins in the biosynthesis of the molybdenum and tungsten cofactors. *Biochemistry* 47, 949-956, (2008).
- 21 Llamas, A., Mendel, R. R. & Schwarz, G. Synthesis of adenylated molybdopterin: an essential step for molybdenum insertion. *J Biol Chem* 279, 55241-55246, (2004).

- 22 Nichols, J. D. & Rajagopalan, K. V. In vitro molybdenum ligation to molybdopterin using purified components. *J Biol Chem* 280, 7817-7822, (2005).
- 23 Palmer, T., Goodfellow, I. P., Sockett, R. E., McEwan, A. G. & Boxer, D. H. Characterisation of the mob locus from *Rhodobacter sphaeroides* required for molybdenum cofactor biosynthesis. *Biochim Biophys Acta* 1395, 135-140, (1998).
- 24 Bittner, F., Oreb, M. & Mendel, R. R. ABA3 is a molybdenum cofactor sulfurase required for activation of aldehyde oxidase and xanthine dehydrogenase in *Arabidopsis thaliana*. *J Biol Chem* 276, 40381-40384, (2001).
- 25 Neumann, M., Schulte, M., Junemann, N., Stocklein, W. & Leimkuhler, S. *Rhodobacter capsulatus* XdhC is involved in molybdenum cofactor binding and insertion into xanthine dehydrogenase. *J Biol Chem* 281, 15701-15708, (2006).
- 26 Lee, H. J., Adham, I. M., Schwarz, G., Kneussel, M., Sass, J. O., Engel, W. & Reiss, J. Molybdenum cofactor-deficient mice resemble the phenotype of human patients. *Hum Mol Genet* 11, 3309-3317, (2002).
- 27 Schwarz, G., Santamaria-Araujo, J. A., Wolf, S., Lee, H. J., Adham, I. M., Grone, H. J., Schwegler, H., Sass, J. O., Otte, T., Hanzelmann, P., Mendel, R. R., Engel, W. & Reiss, J. Rescue of lethal molybdenum cofactor deficiency by a biosynthetic precursor from *Escherichia coli*. *Hum Mol Genet* 13, 1249-1255, (2004).
- 28 Dobbek, H., Gremer, L., Kiefersauer, R., Huber, R. & Meyer, O. Catalysis at a dinuclear [CuSMo(=O)OH] cluster in a CO dehydrogenase resolved at 1.1Å resolution. *Proc Natl Acad Sci U S A* 99, 15971-15976, (2002).
- 29 Chan, M. K., Mukund, S., Kletzin, A., Adams, M. W. & Rees, D. C. Structure of a hyperthermophilic tungstopterin enzyme, aldehyde ferredoxin oxidoreductase. *Science* 267, 1463-1469, (1995).
- 30 Truglio, J. J., Theis, K., Leimkuhler, S., Rappa, R., Rajagopalan, K. V. & Kisker, C. Crystal structures of the active and alloxanthine-inhibited forms of xanthine dehydrogenase from *Rhodobacter capsulatus*. *Structure* 10, 115-125, (2002).
- 31 Nishino, T., Okamoto, K., Eger, B. T. & Pai, E. F. Mammalian xanthine oxidoreductase - mechanism of transition from xanthine dehydrogenase to xanthine oxidase. *FEBS J* 275, 3278-3289, (2008).

- 32 Garattini, E., Mendel, R., Romao, M. J., Wright, R. & Terao, M. Mammalian molybdo-flavoenzymes, an expanding family of proteins: structure, genetics, regulation, function and pathophysiology. *Biochem J* 372, 15-32, (2003).
- 33 Brondino, C. D., Romao, M. J., Moura, I. & Moura, J. J. Molybdenum and tungsten enzymes: the xanthine oxidase family. *Curr Opin Chem Biol* 10, 109-114, (2006).
- 34 Brondino, C. D., Rivas, M. G., Romao, M. J., Moura, J. J. & Moura, I. Structural and electron paramagnetic resonance (EPR) studies of mononuclear molybdenum enzymes from sulfate-reducing bacteria. *Acc Chem Res* 39, 788-796, (2006).
- 35 Hanzelmann, P., Dobbek, H., Gremer, L., Huber, R. & Meyer, O. The effect of intracellular molybdenum in *Hydrogenophaga pseudoflava* on the crystallographic structure of the seleno-molybdo-iron-sulfur flavoenzyme carbon monoxide dehydrogenase. *J Mol Biol* 301, 1221-1235, (2000).
- 36 Feng, C., Tollin, G. & Enemark, J. H. Sulfite oxidizing enzymes. *Biochim Biophys Acta* 1774, 527-539, (2007).
- 37 Kappler, U. & Bailey, S. Molecular basis of intramolecular electron transfer in sulfite-oxidizing enzymes is revealed by high resolution structure of a heterodimeric complex of the catalytic molybdopterin subunit and a c-type cytochrome subunit. *J Biol Chem* 280, 24999-25007, (2005).
- 38 Kappler, U. Bacterial sulfite-oxidizing enzymes. *Biochim Biophys Acta*, (2010).
- 39 Moura, J. J., Brondino, C. D., Trincao, J. & Romao, M. J. Mo and W bis-MGD enzymes: nitrate reductases and formate dehydrogenases. *J Biol Inorg Chem* 9, 791-799, (2004).
- 40 Bertero, M. G., Rothery, R. A., Palak, M., Hou, C., Lim, D., Blasco, F., Weiner, J. H. & Strynadka, N. C. Insights into the respiratory electron transfer pathway from the structure of nitrate reductase A. *Nat Struct Biol* 10, 681-687, (2003).
- 41 Jormakka, M., Richardson, D., Byrne, B. & Iwata, S. Architecture of NarGH reveals a structural classification of Mo-bisMGD enzymes. *Structure* 12, 95-104, (2004).
- 42 Kloer, D. P., Hagel, C., Heider, J. & Schulz, G. E. Crystal structure of ethylbenzene dehydrogenase from *Aromatoleum aromaticum*. *Structure* 14, 1377-1388, (2006).

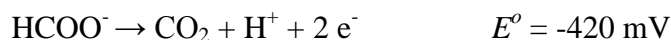
- 43 Schneider, F., Lowe, J., Huber, R., Schindelin, H., Kisker, C. & Knablein, J. Crystal structure of dimethyl sulfoxide reductase from *Rhodobacter capsulatus* at 1.88 Å resolution. *J Mol Biol* 263, 53-69, (1996).
- 44 Schindelin, H., Kisker, C., Hilton, J., Rajagopalan, K. V. & Rees, D. C. Crystal structure of DMSO reductase: redox-linked changes in molybdopterin coordination. *Science* 272, 1615-1621, (1996).
- 45 Czjzek, M., Dos Santos, J. P., Pommier, J., Giordano, G., Mejean, V. & Haser, R. Crystal structure of oxidized trimethylamine N-oxide reductase from *Shewanella massilia* at 2.5 Å resolution. *J Mol Biol* 284, 435-447, (1998).
- 46 Zhang, L., Nelson, K. J., Rajagopalan, K. V. & George, G. N. Structure of the molybdenum site of *Escherichia coli* trimethylamine N-oxide reductase. *Inorg Chem* 47, 1074-1078, (2008).
- 47 Conrads, T., Hemann, C., George, G. N., Pickering, I. J., Prince, R. C. & Hille, R. The active site of arsenite oxidase from *Alcaligenes faecalis*. *J Am Chem Soc* 124, 11276-11277, (2002).
- 48 Ellis, P. J., Conrads, T., Hille, R. & Kuhn, P. Crystal structure of the 100 kDa arsenite oxidase from *Alcaligenes faecalis* in two crystal forms at 1.64 Å and 2.03 Å. *Structure* 9, 125-132, (2001).
- 49 Seiffert, G. B., Ullmann, G. M., Messerschmidt, A., Schink, B., Kroneck, P. M. & Einsle, O. Structure of the non-redox-active tungsten/[4Fe:4S] enzyme acetylene hydratase. *Proc Natl Acad Sci U S A* 104, 3073-3077, (2007).
- 50 Brondino, C. D., Passeggi, M. C., Caldeira, J., Almendra, M. J., Feio, M. J., Moura, J. J. & Moura, I. Incorporation of either molybdenum or tungsten into formate dehydrogenase from *Desulfovibrio alaskensis* NCIMB 13491; EPR assignment of the proximal iron-sulfur cluster to the pterin cofactor in formate dehydrogenases from sulfate-reducing bacteria. *J Biol Inorg Chem* 9, 145-151, (2004).
- 51 Stewart, L. J., Bailey, S., Bennett, B., Charnock, J. M., Garner, C. D. & McAlpine, A. S. Dimethylsulfoxide reductase: an enzyme capable of catalysis with either molybdenum or tungsten at the active site. *J Mol Biol* 299, 593-600, (2000).
- 52 Sawers, R. G. Formate and its role in hydrogen production in *Escherichia coli*. *Biochem Soc Trans* 33, 42-46, (2005).

# **Chapter II**

*Biology and structure of Fdhs*

## II.1 Introduction

Formate dehydrogenases (Fdhs) belong to a heterogeneous group of enzymes found both in prokaryotes and eukaryotes. They catalyze the two-electron oxidation of formate to carbon dioxide according to the half-oxidative reaction:



In aerobic organisms, this reaction is catalyzed by Fdhs dependent on the Nicotinamide Adenine Dinucleotide ( $\text{NAD}^+$ ) cofactor. Figure II.1 shows the active site structure of Fdh from methylotrophic bacterium *Pseudomonas* sp. 101 [1] pointing out the aminoacids residues in the vicinity of the catalytic C4 position of the nicotinamide moiety of  $\text{NAD}^+$ . Ile 122, Asn 146, Arg 284 and His 332 are conserved in  $\text{NAD}$ -dependent Fdhs, they are responsible for substrates orientation favoring the hydride transfer from formate to the C4 of  $\text{NAD}^+$  [2,3].

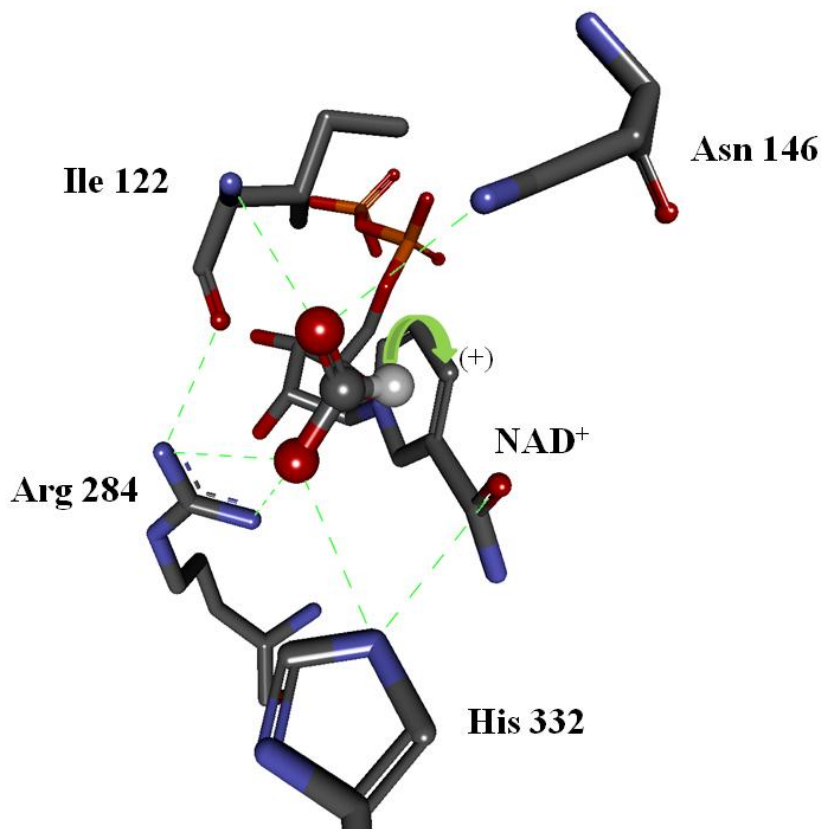


**Figure II.1| NAD-dependent Fdh active site.** Crystal structure of  $\text{NAD}$ -dependent formate dehydrogenase active site from methylotrophic bacterium *Pseudomonas* sp. 101, adapted from reference [1].



Prokaryotes organisms grow under hostile conditions, such as anoxic environments, have developed mechanisms to use electrons from formate for the generation of energy. Under anaerobic conditions, formate can be used as a major electron donor to a variety of inducible respiratory pathways that use as terminal electron acceptors compounds other than molecular oxygen [4,5]. In this case, Fdhs are  $\text{NAD}^+$ -independent enzymes containing redox centers that include transition metals, such as molybdenum or tungsten atoms associated to the pyranopterin guanine dinucleotide (PGD) cofactor and iron in the form of iron-sulfur clusters and/or hemes. *Since this work focus the study of  $\text{NAD}^+$ -independent Fdhs, the following sections will refer to  $\text{NAD}^+$ -independent Fdhs as Fdh.*

The crystal structures of three Fdh proteins have been reported to date, two containing molybdenum and one tungsten. The two Mo-containing enzymes are the Fdh-H [6] and Fdh-N [7] purified from *E. coli*. The W-containing enzyme is the Fdh isolated from the sulfate reducer *D. gigas* [8,9]. The overall structure of all three  $\alpha$  subunits are very similar with many conserved amino acids near the active site among which stand out the selenocysteine (SeCys), an adjacent histidine (His), and an arginine (Arg) that is believed to stabilize the negatively charged substrate in the active site.

The metal ion at the Fdh active site presents a distorted octahedral geometry with four thiol ligands from two pyranopterin guanine dinucleotide (PGD) molecules, one inorganic sulfur (previously proposed as a hydroxyl group), and selenium from the SeCys residue. The gene encoding for the catalytic  $\alpha$  subunit contains an in-frame opaI (UGA) codon specific for SeCys incorporation [10,11]. The mechanism to make a distinction between a selenocysteine insertion into a polypeptide and a termination polypeptide synthesis depends on the presence of a 40-base sequence downstream of the UGA codon [12]. The sequence fold into a stem-loop structure called SECIS element. The SECIS element contains a conserved cytosine, adjacent to the UGA codon, which prevents UGA reading. Furthermore, a bulged thymine, which interacts with a protein homologous to the elongation factor (SelB), is included. In addition to the cytosine and thymine present in the SECIS element, the *selA*, *selB*, *selC* and *selD* gene products are also necessary for selenocysteine insertion in *Ec* Fdh-H [13,14].

II.2 Fdh: an overview of the biochemical and crystallographic characteristics.

II.2.1 Fdh-H from *E. coli*

Fdh-H, one of the components of the formate-hydrogen lyase complex, is a monomeric 79-kDa enzyme containing one [4Fe-4S] cluster and one Mo coordinated by two MGD cofactors, one sulfur (or hydroxyl) group and a SeCys residue (figure II.2) [6,15,16].

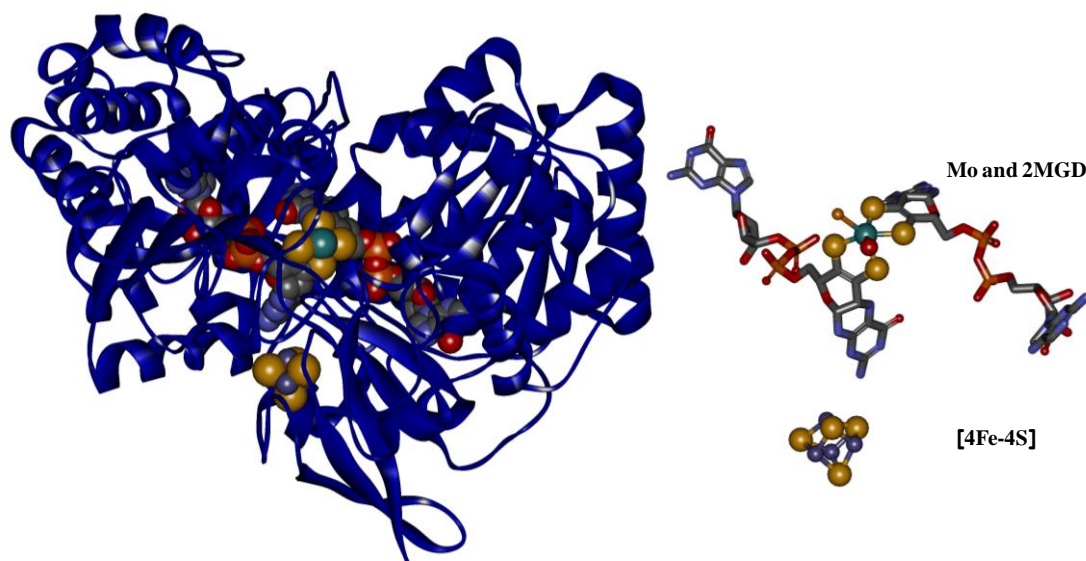


**Figure II.2| *E. coli* formate dehydrogenase H structure [17].** Left: Fdh-H structure at 2.27 Å (PDB code: 2IV2). Right: Redox centers in Fdh-H: molybdenum active site and [4Fe-4S] center.

The crystal structures of oxidized (2.8 Å resolution) and formate-reduced (2.3 Å resolution) forms of *Ec* Fdh-H firstly reported suggested that the sixth ligand was a hydroxyl molecule (figure II.3A and II.3B, respectively) [6]. Later, a re-interpretation of the data obtained from the reduced state of Fdh-H showed that the hydroxyl group refined better as a sulfur atom (=S or –SH instead of H<sub>2</sub>O or -OH) and in addition some differences were found in the amino acids located near to the active site (figure II.3C) [17]. The new interpretation showed that SeCys was not bound to the molybdenum after reduction with formate, being shifted 12 Å away from the active site [17]. These results had important consequences in the reaction mechanism previously proposed, which will be discussed in Chapter IV.

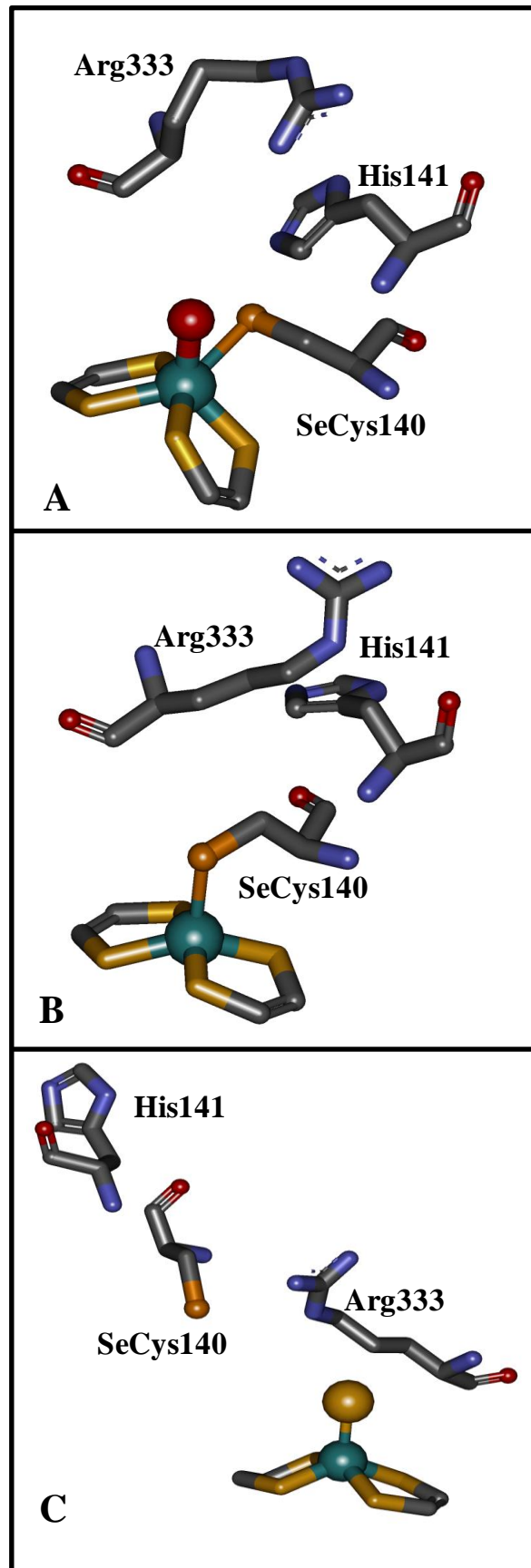


**Figure II.3| Active site of Fdh-H from *E. coli*.** A: Oxidized Fdh-H active site [6]. B: Reduced Fdh-H active site [6]. C: Reduced Fdh-H active site (reinterpretation) [17].

### **II.2.2 Fdh-N from *E. coli***

During the anaerobic growth of *E. coli* in the presence of nitrate, the major electron donor to the nitrate respiration system is formate, a product of the pyruvate degradation catalyzed by pyruvate formate lyase. Under these conditions, two membrane proteins are induced: dissimilatory nitrate reductase (Nar) [4] and formate dehydrogenase-N (Fdh-N, N from nitrate inducible) [7,18]. Fdh-N is supposed to participate in the redox loop of the proton motive force generation across the membrane cell and electron transfer between formate and menaquinone [7,19].

This enzyme is a very large (510 kDa) heterotrimeric complex  $\alpha_3\beta_3\gamma_3$  with subunits of 113, 32 and 21 kDa, respectively (figure II.4) [7].

Similar to Fdh-H, Fdh-N active site is constituted by a Mo atom that is coordinated by two MGD cofactors, one hydroxyl group and one SeCys residue. This active center together with a [4Fe-4S] cluster are harbored in the  $\alpha$  subunit. The  $\beta$  subunit contains four [4Fe-4S] clusters and mediates the electron transfer between the  $\alpha$  and  $\gamma$  subunits. The  $\gamma$  subunit is constituted by four transmembrane helices that anchor the Fdh-N to the membrane and coordinate two heme *b* groups that led the electrons transfer to a menaquinone [7]. The crystal structure indicates that  $\alpha$  and  $\beta$  subunits of Fdh-N are on the periplasmic side of the membrane [19,20]. The catalytic  $\alpha$  subunit is considerably larger than that of Fdh-H but the three-dimensional core is quite similar [21].

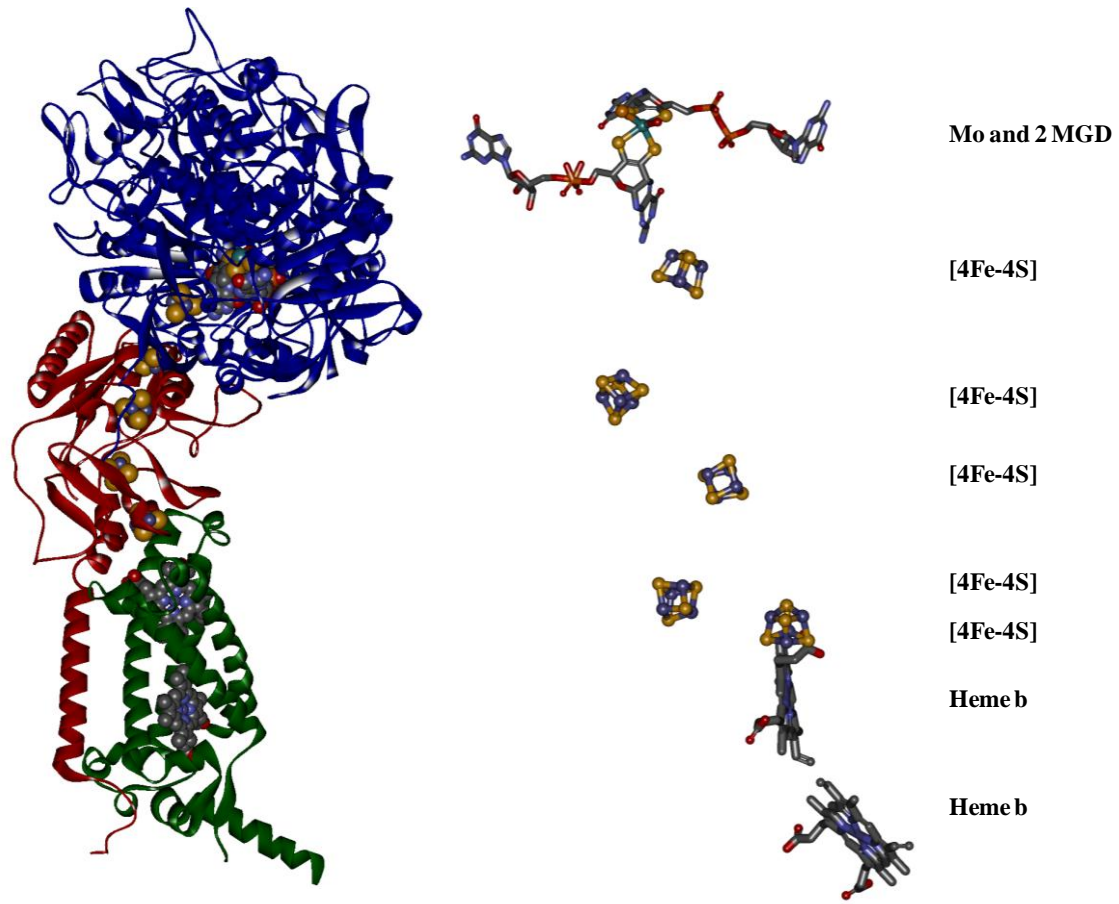


**Figure II.4** | *E. coli* Fdh-N structure[7]. Left: Fdh-N structure at 1.6Å (PDB code:1KQF). Right: Redox centers in Fdh-N: molybdenum active site, [4Fe-4S] centers and type *b* hemes.

### II.2.3 Fdh from *D. gigas*

*Dg* Fdh was the first tungsten-containing enzyme from sulfate reducing bacteria that has been structurally characterized [8,9,22]. The W-Fdh is a heterodimer of 92 and 29 kDa subunits [22]. The large subunit, homologous to *Ec* Fdh-H and  $\alpha$  subunit of Fdh-N, harbors the W active site that is coordinated by two MGD, a SeCys and one sulfur group (SH). Four [4Fe-4S] centers are present in this enzyme: one in the  $\alpha$  subunit and three in the  $\beta$  subunit (figure II.5) [8,9].

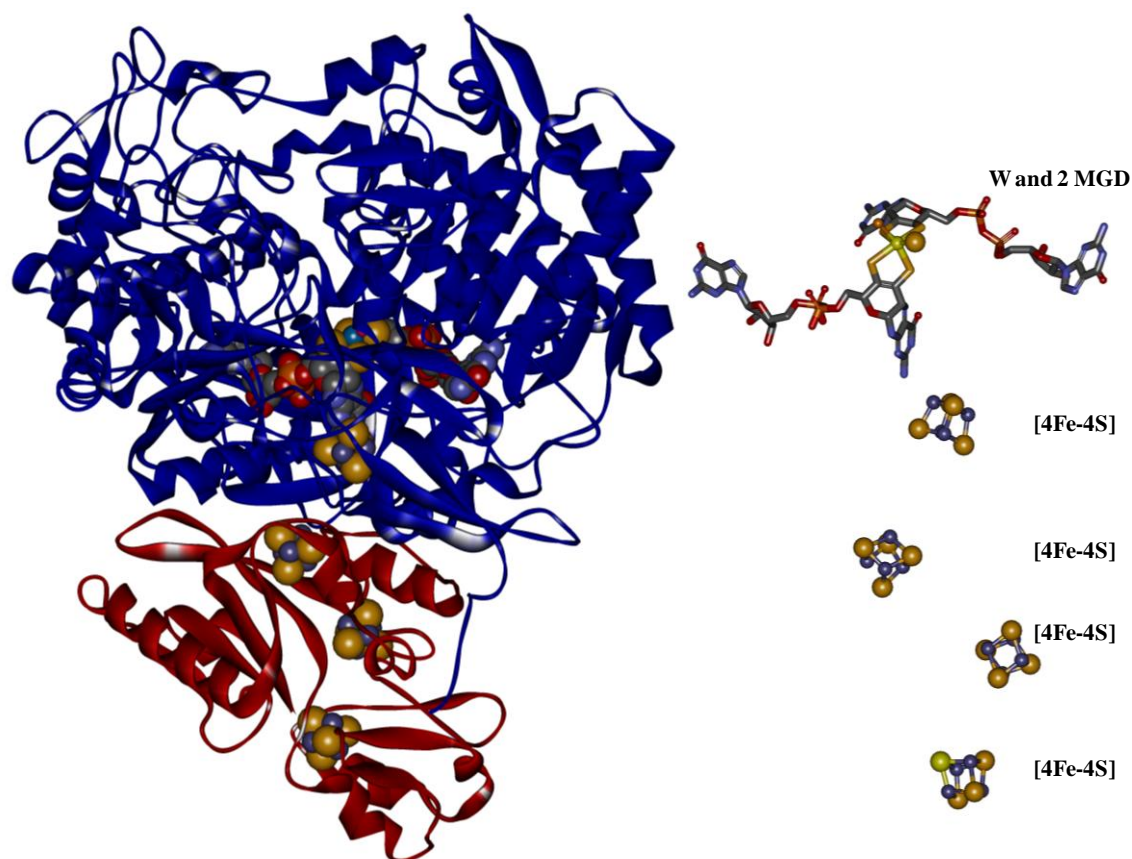


**Figure II.5** | *D. gigas* Fdh structure [9]. Left: Fdh structure at 1.8 Å (PDB code:1H0H). Right: Redox centers in Fdh: tungsten active site and [4Fe-4S] centers.

The structural homology between the  $\alpha$  subunit of Fdhs shows that the essential residues SeCys158, His159, and Arg407 at the active site are conserved [9]. The active site is accessible for substrate via a positively charged tunnel, while product release may be facilitated by a hydrophobic channel for CO<sub>2</sub>, and through buried water molecules and protonable amino acids for H<sup>+</sup> [9].

#### II.2.4 Fdh from *D. desulfuricans*

Although, the Mo-Fdh from *D. desulfuricans* was purified, characterized and deeply studied [23,24], the crystallographic structure was not solved yet. The amino acid sequence of this enzyme is highly similar to the trimeric Fdh from *D. vulgaris* (*loci tag* DVU2809-12). The *Dd* Fdh is a  $\alpha\beta\gamma$  heterotrimer of 88, 29 and 16 kDa, respectively. The large subunit harbours the Mo site (though to be similar to the *Ec* Fdh-H active site, figure II.2) and one [4Fe-4S] center. The  $\beta$  and  $\gamma$  subunits hold three [4Fe-4S] centers and four c-type hemes, respectively.

### II.3 References

- 1 Lamzin, V. S., Dauter, Z., Popov, V. O., Harutyunyan, E. H. & Wilson, K. S. High resolution structures of holo and apo formate dehydrogenase. *J Mol Biol* 236, 759-785, (1994).
- 2 Castillo, R., Oliva, M., Marti, S. & Moliner, V. A theoretical study of the catalytic mechanism of formate dehydrogenase. *J Phys Chem B* 112, 10012-10022, (2008).
- 3 Tishkov, V. I., Matorin, A. D., Rojkova, A. M., Fedorchuk, V. V., Savitsky, P. A., Dementieva, L. A., Lamzin, V. S., Mezentzev, A. V. & Popov, V. O. Site-directed mutagenesis of the formate dehydrogenase active centre: role of the His332-Gln313 pair in enzyme catalysis. *FEBS Lett* 390, 104-108, (1996).
- 4 Richardson, D. J. Bacterial respiration: a flexible process for a changing environment. *Microbiology* 146 ( Pt 3), 551-571, (2000).
- 5 Matias, P. M., Pereira, I. A., Soares, C. M. & Carrondo, M. A. Sulphate respiration from hydrogen in *Desulfovibrio* bacteria: a structural biology overview. *Prog Biophys Mol Biol* 89, 292-329, (2005).
- 6 Boyington, J. C., Gladyshev, V. N., Khangulov, S. V., Stadtman, T. C. & Sun, P. D. Crystal structure of formate dehydrogenase H: catalysis involving Mo, molybdopterin, selenocysteine, and an Fe<sub>4</sub>S<sub>4</sub> cluster. *Science* 275, 1305-1308, (1997).
- 7 Jormakka, M., Tornroth, S., Byrne, B. & Iwata, S. Molecular basis of proton motive force generation: structure of formate dehydrogenase-N. *Science* 295, 1863-1868, (2002).
- 8 Raaijmakers, H., Teixeira, S., Dias, J. M., Almendra, M. J., Brondino, C. D., Moura, I., Moura, J. J. & Romao, M. J. Tungsten-containing formate dehydrogenase from *Desulfovibrio gigas*: metal identification and preliminary structural data by multi-wavelength crystallography. *J Biol Inorg Chem* 6, 398-404, (2001).
- 9 Raaijmakers, H., Macieira, S., Dias, J. M., Teixeira, S., Bursakov, S., Huber, R., Moura, J. J., Moura, I. & Romao, M. J. Gene sequence and the 1.8 Å crystal structure of the tungsten-containing formate dehydrogenase from *Desulfovibrio gigas*. *Structure* 10, 1261-1272, (2002).

- 
- 10 Berg, B. L., Li, J., Heider, J. & Stewart, V. Nitrate-inducible formate dehydrogenase in *Escherichia coli* K-12. I. Nucleotide sequence of the fdnGHI operon and evidence that opal (UGA) encodes selenocysteine. *J Biol Chem* 266, 22380-22385, (1991).
- 11 Stadtman, T. C. Selenocysteine. *Annu Rev Biochem* 65, 83-100, (1996).
- 12 Liu, Z., Reches, M., Groisman, I. & Engelberg-Kulka, H. The nature of the minimal 'selenocysteine insertion sequence' (SECIS) in *Escherichia coli*. *Nucleic Acids Res* 26, 896-902, (1998).
- 13 Zinoni, F., Heider, J. & Bock, A. Features of the formate dehydrogenase mRNA necessary for decoding of the UGA codon as selenocysteine. *Proc Natl Acad Sci U S A* 87, 4660-4664, (1990).
- 14 Bock, A., Forchhammer, K., Heider, J., Leinfelder, W., Sawers, G., Veprek, B. & Zinoni, F. Selenocysteine: the 21st amino acid. *Mol Microbiol* 5, 515-520, (1991).
- 15 Gladyshev, V. N., Khangulov, S. V., Axley, M. J. & Stadtman, T. C. Coordination of selenium to molybdenum in formate dehydrogenase H from *Escherichia coli*. *Proc Natl Acad Sci U S A* 91, 7708-7711, (1994).
- 16 Axley, M. J., Grahame, D. A. & Stadtman, T. C. *Escherichia coli* formate-hydrogen lyase. Purification and properties of the selenium-dependent formate dehydrogenase component. *J Biol Chem* 265, 18213-18218, (1990).
- 17 Raaijmakers, H. C. & Romao, M. J. Formate-reduced *E. coli* formate dehydrogenase H: The reinterpretation of the crystal structure suggests a new reaction mechanism. *J Biol Inorg Chem* 11, 849-854, (2006).
- 18 Jormakka, M., Tornroth, S., Abramson, J., Byrne, B. & Iwata, S. Purification and crystallization of the respiratory complex formate dehydrogenase-N from *Escherichia coli*. *Acta Crystallogr D Biol Crystallogr* 58, 160-162, (2002).
- 19 Richardson, D. & Sawers, G. Structural biology. PMF through the redox loop. *Science* 295, 1842-1843, (2002).
- 20 Jormakka, M., Byrne, B. & Iwata, S. Protonmotive force generation by a redox loop mechanism. *FEBS Lett* 545, 25-30, (2003).
- 21 Moura, J. J., Brondino, C. D., Trincao, J. & Romao, M. J. Mo and W bis-MGD enzymes: nitrate reductases and formate dehydrogenases. *J Biol Inorg Chem* 9, 791-799, (2004).



- 22 Almendra, M. J., Brondino, C. D., Gavel, O., Pereira, A. S., Tavares, P., Bursakov, S., Duarte, R., Caldeira, J., Moura, J. J. & Moura, I. Purification and characterization of a tungsten-containing formate dehydrogenase from *Desulfovibrio gigas*. *Biochemistry* 38, 16366-16372, (1999).
- 23 Rivas, M. G., Gonzalez, P. J., Brondino, C. D., Moura, J. J. & Moura, I. EPR characterization of the molybdenum(V) forms of formate dehydrogenase from *Desulfovibrio desulfuricans* ATCC 27774 upon formate reduction. *J Inorg Biochem* 101, 1617-1622, (2007).
- 24 Costa, C., Teixeira, M., LeGall, J., Moura, J. J. G. & Moura, I. Formate dehydrogenase from *Desulfovibrio desulfuricans* ATCC27774: isolation and spectroscopic characterization of the active sites (heme, iron- sulfur centers and molybdenum). *J Biol Chem* 2, 198-208, (1997).



# Chapter III

*Influence of Mo and W in the expression of Fdh from  
D. alaskensis*

### III.1 Summary

In the present work the influence of Mo and W salts on the production of Fdh by *D. alaskensis* was studied. Two different Fdhs, one containing W (W-Fdh) and a second Fdh that incorporates either Mo or W (Mo/W-Fdh), were purified. Both enzymes were isolated from cells grown in a medium supplemented with 1  $\mu$ M molybdate, whereas only the W-Fdh was purified from cells cultured in medium supplemented with 10  $\mu$ M tungstate. We identified the genes encoding these Fdhs and demonstrated that the genes encoding the Mo/W-Fdh are strongly down-regulated by W and slightly up-regulated by Mo. Effects of metals on the expression level of the genes encoding the W-Fdh were less significant. Furthermore, the expression levels of the genes encoding proteins involved in molybdate and tungstate transport are down-regulated under the experimental conditions evaluated in this work. The molecular and biochemical properties of these enzymes and the selective incorporation of Mo and W are discussed.

### III.2 Introduction

Mo and W have very similar chemical properties, however, in some cases proteins contain exclusively one of these metals in the active site and the unspecific metal incorporation results in inactive enzymes [1-3]. In contrast, some microorganisms have enzymes that can incorporate either Mo or W depending on the growth conditions [4-6]. Fdhs from *Desulfovibrio* species have been isolated as Mo-containing proteins from *D. desulfuricans* [7-9], *D. vulgaris* [10-12], and as W-containing protein from *D. gigas* [13-15]. In contrast *D. alaskensis* grown in medium C [16] produces a mixture of Fdhs each containing a mononuclear Mo or W site[17].

Analysis of the genome of *D. desulfuricans* G20 (genome.jgi-psf.org), closely related to *D. alaskensis* [18-20], shows at least three periplasmic Fdhs are encoded in the chromosome of this organism, corresponding to the *loci* tag *Dde\_3512-Dde\_3514*, *Dde\_0716-Dde\_0718* and *Dde\_0813-0814*, respectively. Amino acid sequence alignment of the proteins coded by these genes show a high identity percentage (48-75%) with the homologous proteins isolated and characterized from other *Desulfovibrio* species. Similar to these proteins, the *D. desulfuricans* G20 Fdhs appear as heterodimeric soluble enzymes composed of alpha and a beta subunit. Three major

features are found in the amino acid sequence of the alpha subunit: a twin-arginine motif (RRXFL/IK) characteristic of Sec-independent export to periplasm [21,22], a molybdopterin dinucleotide-binding region which is in line with the presence of the active site attached to this subunit, and a motif CXXCX<sub>n</sub>CX<sub>m</sub>C, known to coordinate [4Fe-4S] clusters. The beta subunit contains three additional [4Fe-4S] binding motifs, which is in agreement with the [4Fe-4S] centers observed in the crystallographic structure of the homologous *Dg Fdh* [14,15].

Although the synthesis of the MoCo or WCo present in Fdhs and other Mo-enzymes was extensively studied [23-25], the selective incorporation of either Mo or W in the enzyme cofactors is not understood yet. Several proteins are involved in the metal insertion step of this biosynthetic pathway with MoeA being one of them [26,27]. The function proposed for the MoeA protein is to form a complex with the adenylylated metal-binding pterin (MPT), which is hydrolyzed in the presence of molybdate or tungstate to incorporate the metal into the cofactor [28]. The presence of two *moeA* genes sharing approximately 40% of sequence similarity between them in numerous bacterial genomes, gave rise to the hypothesis that these proteins would have Mo or W selective activities [24,29]. The analysis of the *D. desulfuricans* G20 genome also reveals two *moeA*-like genes sharing 32.5% of sequence identity (*Dde\_0230* and *Dde\_3228*, respectively) suggesting that this hypothesis may also be proposed for this organism.

Regarding to the Mo and W incorporation into the cells, as already described in Chapter I (section I.2.1), these metals are transported as molybdate and tungstate ions by proteins belonging to the ABC transporter family [23,30,31]. In *D. desulfuricans* G20, the Mo transport system is encoded by the *mod* genes cluster which contains the *Dde\_3518*, *Dde\_3519* and *Dde\_3520* genes (*modA*, *modB*, and *modC*, respectively). Similarly, the proteins putatively involved in tungstate transport are encoded by the *tup* genes cluster including the *Dde\_0234*, *Dde\_0233* and *Dde\_0232* genes (*tupA*, *tupB* and *tupC*, respectively).

In this chapter, studies aimed to understand the effects of Mo or W supplementation on the expression levels and activity profiles of the different *Da Fdhs* are reported. In addition the effect of molybdate and tungstate on the expression level of the genes encoding proteins involved in Mo and W transport and Mo/W-pterin cofactor insertion was investigated. The results show that the presence of each metal in the culture

medium has remarkable effects on both gene expression and biochemical properties of Fdhs.

### III.3 Experimental procedures

**III.3.1 Bacterial strain, culture media, and growth conditions.** *D. alaskensis* cells were used in all the experiments performed in this work. Since the genome of this subspecies is not reported, the genomic analysis was performed on the basis of the genome of the closely related *D. desulfuricans* G20 strain ([www.tigr.org](http://www.tigr.org)).

*D. alaskensis* was grown at 37°C under anaerobic conditions in medium C adapted from Postgate [16]. The medium used consisted of 3.6 mM  $\text{KH}_2\text{PO}_4$ , 18.7 mM  $\text{NH}_4\text{Cl}$ , 31.7 mM  $\text{Na}_2\text{SO}_4$ , 0.24 mM  $\text{MgSO}_4 \cdot 7\text{H}_2\text{O}$ , 0.27  $\text{CaCl}_2 \cdot 2\text{H}_2\text{O}$ , 0.1% (wt/vol) yeast extract, 14.4  $\mu\text{M}$   $\text{FeSO}_4 \cdot 7\text{H}_2\text{O}$ , 1.02 mM sodium citrate dihydrate, and 0.43 mM  $\text{NaCl}$ . The pH was adjusted to 7.5 with  $\text{NaOH}$ . Different combinations of carbon sources were tested: 30 mM sodium lactate; 29.4 mM sodium lactate + 0.6 mM sodium formate; 29.1 mM sodium lactate + 0.6 mM sodium formate + 0.3 mM sodium acetate; 22.5 mM sodium lactate + 7.5 mM sodium formate; 15 mM sodium lactate + 7.5 mM sodium formate + 7.5 mM sodium acetate and 7.5 mM sodium lactate + 15 mM sodium formate + 7.5 mM sodium acetate. In addition, the following lactate and formate concentrations (mM) were tested: 30:7.5, 27:3, 25.5:4.5, 22.5:7.5, and 19.5:10.

The effect of Mo and W supplementation on the Fdhs production was evaluated by adding to the optimized culture medium (see results, section III.4.1) 45 nM, 100 nM, 500 nM, 1  $\mu\text{M}$  or 10  $\mu\text{M}$  of either  $\text{Na}_2\text{MoO}_4 \cdot 2\text{H}_2\text{O}$  or  $\text{Na}_2\text{WO}_4 \cdot 2\text{H}_2\text{O}$ .

**III.3.2 Soluble extract preparation and activity tests.** Cells from each condition described above were collected at the end of the exponential growth phase (OD 0.5-0.6) by centrifugation ( $7000 \times g$  for 15 min at 4°C) and the pellet was resuspended in 10 mM Tris-HCl buffer (pH 7.60) to a cell density of 0.1 g cells (wet weight) per mL. To prepare soluble extracts, cells suspension was subjected to 4 freeze-thaw cycles and centrifuged at  $7000 \times g$  for 40 minutes to remove cells. Supernatant was subsequently used for activity measurements. Total protein concentration for each extract was determined by using the Bicinchoninic Acid kit from Sigma-Aldrich. In gel Fdh activity

was performed by running equal amounts of total proteins from each soluble extract on 7.5% native polyacrylamide gels under native conditions (10  $\mu\text{g}$  of total proteins for all the conditions except for the Mo-supplementation experiments where 45  $\mu\text{g}$  were loaded). After electrophoresis, the assay was performed at 37°C in anaerobic conditions by bubbling argon in the activity solution. Gels were placed in rubber stoppered tubes containing a 10 mM HCOONa, 130 mM  $\beta$ -mercaptoethanol, and 60 mM TrisHCl buffer (pH 8.00) solution and incubated during 10 minutes. Then, methyl viologen was added (final concentration of 7.5 mM) to development of blue activity bands. Finally, to fix the bands, 2,3,5-triphenyltetrazolium chloride (Sigma-Aldrich) was added to a final concentration of 7.5 mM and the gels were incubated for further 15 minutes. In all the experiments a sample containing active Fdh from *D. desulfuricans* was loaded as positive control.

Steady-state kinetic studies on Fdhs were performed under argon atmosphere at 37 °C by monitoring the benzyl viologen (BV) reduction at 555 nm ( $\epsilon=12 \text{ mM}^{-1}\text{cm}^{-1}$ ) in a 1 cm optical path length cell provided with a magnetic stirrer, as previously described [9]. The reaction mixture (1.1 mL of final volume) contained 60 mM Tris-HCl buffer pH 8.00, 7.50 mM BV, 133 mM  $\beta$ -mercaptoethanol ( $\beta$ -ME), and formate as substrate. Each assay contained 300 nM of Mo/W-Fdh or 10 nM W-Fdh (see Result section). In all assays, the enzyme was incubated with the buffer and  $\beta$ -ME under argon atmosphere during 10 min. In order to activate de enzyme, formate was added and incubated during additional 10 min. The reaction was started by the addition of benzyl viologen. Absorbance at 555 nm was followed using an Agilent 8453 Diode-array spectrophotometer. Under these experimental conditions, one enzymatic unit (U) corresponds to 1  $\mu\text{mol}$  of formate oxidized (2  $\mu\text{mol}$  of BV reduced) *per* min and the specific activity is U/mg of enzyme.

**III.3.3 Enzymes purification.** *D. alaskensis* was anaerobically cultured in modified medium C (final concentration of 25.5 mM lactate, 4.5 mM formate) and either 1  $\mu$ M  $\text{Na}_2\text{MoO}_4 \cdot 2\text{H}_2\text{O}$  or 10  $\mu$ M  $\text{Na}_2\text{WO}_4 \cdot 2\text{H}_2\text{O}$ . Cells were collected by centrifugation at the end of the exponential growth phase. Soluble extracts were obtained from cell resuspended in 10 mM Tris-HCl buffer (pH 7.6) and disrupted with a French press at 9000 psi. Broken cells were centrifuged at  $10\,000 \times g$  for 45 min at 4°C and the supernatants further centrifuged at  $180\,000 \times g$  for 60 min at 4°C.

All purification steps were performed at 4°C and pH 8.0. Soluble fractions were dialyzed overnight against 5 mM Tris-HCl and loaded onto a DE-52 cellulose resin equilibrated with 5 mM Tris-HCl. Elution was performed with a linear gradient (5 mM to 500 mM of Tris-HCl) in 5 column volumes. Soluble extracts from cells cultured under either Mo or W excess conditions showed Fdh activity in fractions eluted at 350 mM Tris-HCl but only the condition corresponding to Mo supplementation showed additional enzyme activity in fractions eluted at 200 mM Tris-HCl. The protein pools containing Fdh were independently concentrated, and loaded onto a Source 15Q column equilibrated with 10 mM Tris-HCl buffer. Elution was performed using a linear gradient to 50 mM Tris-HCl/500 mM NaCl in 10 column volumes. Fractions containing Fdh were pooled, dialyzed, concentrated and loaded into a Resource Q column (6 mL, GE Healthcare) equilibrated with 50 mM potassium phosphate buffer (KPB). Elution was performed using a linear gradient to 50 mM of KPB/ 500 mM of NaCl in 25 column volumes. Fdh active samples were pooled, concentrated and loaded onto a Superdex 200 column equilibrated with 50 mM KPB/150 mM NaCl. After this purification step the enzymes eluted at 350 mM Tris-HCl from the DE-52 were considered pure as judged by SDS-PAGE and UV-visible spectroscopy. Therefore, the total purification procedure used to purify this enzyme consisted in four chromatographic steps.

The highest purity of the Fdh samples eluted at 200 mM Tris-HCl from the DE-52 (see above) was achieved by a fifth purification step that included a MonoQ column (1 mL, GE Healthcare) equilibrated with 50 mM of KPB and eluted to 50 mM KPB/300 mM of NaCl in 25 column volumes.



**III.3.4 Protein and metal content quantification.** Protein quantification was performed using the BCA kit from Sigma-Aldrich with bovine serum albumin as standard. Metal content in the samples and media was determined through Inductively Coupled Plasma Atomic Emission Spectroscopy (ICP-AES) in a Jobin-Yvon (Ultima) instrument. A tungsten standard solution from CRM (Aqueous calibration Solution) was used to quantify this metal and multielements standard solution (Reagecon 23 ICP) was used for molybdenum. The concentration range of both standard solutions was 0.5-15.6  $\mu\text{M}$ .

**III.3.5 Molecular mass and cofactor content determination.** The molecular masses of the pure proteins were determined under non denaturing conditions by gel-filtration chromatography on a Superdex 200 column (GE Healthcare) connected to an HPLC device (AKTA Basic, GE Healthcare). The elution buffer used was 50 mM KPB/ 150 mM NaCl pH 7.00, and the column was calibrated using proteins from 13 kDa to 669 kDa, all from GE Healthcare. Subunit composition and purity of the samples were evaluated by SDS-PAGE, on 12.5% polyacrylamide gel. Molecular-mass standards (Fermentas) were used for calibration, and gels were stained with Coomassie Brilliant Blue G-250 (Merck).

Cofactor content was determined as previously published [32,33]. Briefly, Fdh samples containing sulphuric acid (3% vol/vol) were heated at 95 °C for 10 min, and centrifuged for 5 min at 10 000  $\times$  g. A volume of 100  $\mu\text{L}$  was loaded in reverse phase column (Merck LiChrospher 100, 250.4, RP-18e, 4  $\mu\text{m}$ ) connected to a HPLC device (AKTA BASIC, GE Healthcare). Ammonium acetate 50 mM (pH 6.80) was used as eluent at a flow rate of 1 mL/min and nucleotides were detected at 254 nm. Quantitative determinations were performed by loading fresh solutions of known mononucleotides amounts (Sigma-Aldrich) previously submitted to identical acid/heating treatment.

**III.3.6 Determination of the N-terminal sequence of Fdhs from D. alaskensis.** Fdh samples (600 pmol) were electrophoresed on a 12.5% SDS-polyacrylamide gel. Gel pieces containing each subunit were excised and incubated in 500  $\mu\text{L}$  of Millipore water at 4 °C during 36 h. After that, gel was removed and the solution was concentrated until 50  $\mu\text{L}$  in a speedvac centrifuge (UniEquip -Martinsried, Germany- model UNIVAPO 100H) equipped with a refrigerated aspirator vacuum pump model Unijet II. Subunits were sequenced by Edman degradation reaction, in a Protein Sequencer (Applied

Biosystems, model 491). Sequences were compared with deduced amino acid sequences from the *D. desulfuricans* G20 genome ([www.tigr.org](http://www.tigr.org)).

**III.3.7 Quantitative real-time PCR (qRT-PCR).** *D. alaskensis* cells were cultured at 37°C under anaerobic conditions in 100 mL of modified medium without metal addition (control) and modified medium C supplemented either with 1 µM of Na<sub>2</sub>MoO<sub>4</sub>·2H<sub>2</sub>O or 10 µM of Na<sub>2</sub>WO<sub>4</sub>·2H<sub>2</sub>O. Once the optical density at 600 nm (OD<sub>600nm</sub>) reached 0.5-0.6, cells were chilled on ice for 10 min, harvested by centrifugation at 8000 × g for 20 min at 4°C and washed once with 1 mL of 0.1 M Tris 10 mM (pH 8.0). The pellets were subsequently used for RNA extraction and quantitative real-time PCR experiments.

For total RNA isolation, cell pellets were resuspended in 200 µL of 10 mM Tris-HCl, 1 mM EDTA (pH 8.0) RNase-free buffer. Total RNA was isolated by using the High Pure RNA Isolation Kit (Roche Diagnostics) according to the manufacturer's instructions with an extra DNase I digestion step in order to eliminate contaminating DNA. RNAs quality was checked by electrophoresis on agarose gel and the absence of DNA contamination was confirmed by PCR. RNAs was quantified spectrophotometry at 260 nm (NanoDrop 1000 ThermoScience). For cDNA synthesis, 10 µg of total RNA and 3 µg of random primers (Invitrogen) were mixed, heated to 70°C for 3 min and placed in ice. The cDNA synthesis mix [50 mM Tris-HCl (pH 8.3), 40 mM KCl, 6 mM MgCl<sub>2</sub>, 10 mM DTT, and 0.3 mM dNTPs] was then added. The reaction mix (30 µL) was incubated for 5 min at 25°C and 300 units of Superscript II reverse transcriptase (Invitrogen) was then added. The reaction mix was incubated for 5 min at 25°C, then 1 h at 42°C and finally for 15 min at 70°C for heat inactivation. The reaction mixture volume was then adjusted to 100 µL with ultra-pure water. cDNAs were prepared from three independent cultures and were further used for quantitative Real-Time PCR (qRT-PCR).

Quantification of the cDNAs was carried out with the LightCycler System using the LightCycler FastStart DNA master<sup>plus</sup> SYBR greenI kit (Roche), according to the manufacturer's instructions. Primers based on the *D. desulfuricans* G20 genome ([www.tigr.org](http://www.tigr.org)) were designed to specifically amplify a portion of each targeted gene (table 1). The LightCycler was programmed for an initial step at 95°C for 480 sec, followed by 45 thermal cycles at 95°C for 12 sec, 59°C for 6 sec and 72°C for 20 sec. Specificities of accumulated products were verified by using the melting-curve analysis.

The Relative Expression Software Tool (REST) was used to calculate the relative expression of each gene in each condition [34], using the 16S RNA gene as reference for normalization. Quantification was performed in triplicate on each cDNA preparation.

**Table III.1|** Primers used for the qRT-PCR experiments.

<b>Primer</b>	<b>Sequence*</b>	<b>Target gene/Locus Tag</b>
Dde0717Left	5' GATGCACAAGGAGCAGTTCA	<i>Fdh2A/ Dde_0717</i>
Dde0717Right	5' CGTCTTGATGTCGGAAGGAT	
Dde3513left	5' TTCACCGTTCAGGGAAAAAC	<i>Fdh1A/ Dde_3513</i>
Dde3513right	5'GTGTCGGCCTTGCGTATATT	
Dde0813left	5' TGTACTGCGCTTCGTACACC	<i>Fdh3A/ Dde_0813</i>
Dde0813right	5' GTACGTCGCCTGTCCATTTT	
Dde3518right	5' CAGTTTGCCTGTGGAGGAAT	<i>modA / Dde_3518</i>
Dde3518left	5' ATGCTGTCACGTCTGTACGC	
Dde0234right	5' GTCGCAGTTTTACCCATTT	<i>tupA / Dde_0234</i>
Dde0234left	5' AGCACCGGTTCTTATGATGG	
Dde3519right	5' ATCAGCCGTTTCGTTGAAAAC	<i>modB / Dde_3519</i>
Dde3519left	5' TAGCAGACCCGCTGTACCTT	
Dde0233right	5' GCAGGGCATAGACGATAAGC	<i>tupB / Dde_0233</i>
Dde0233left	5' CGGTAACCACCATGTCTGTG	
Dde0230right	5' ATAACTTCGTCTCCGGTGGGA	<i>moeA1/ Dde_0230</i>
Dde0230left	5' CCGTTGAAATACGCAAATCC	
Dde3328right	5' AAATGTGGGGGAGGAAAAAC	<i>moeA2/ Dde-3228</i>
Dde3228left	5' CAAGCGCAATGTCTACCTGA	

\* Sequences were based on the closely related *D. alaskensis* G20 genome ([www.tigr.org](http://www.tigr.org)).

## III.4 Results

## III.4.1 Carbon source and optimal metal concentration for Fdh production.

In order to optimize the Fdh production, *D. alaskensis* cells were cultured in different media based on medium C [16] but differing in their carbon source. Lactate, the most commonly used carbon and energy source, was partially replaced by formate and/or acetate and effects on Fdhs expression were evaluated by analysing the Fdh activity on native gels. Since biomass and enzyme production does not seem to depend on the presence of acetate in the medium (figure III.1A), additional tests were performed to optimize the formate concentration leading to the highest enzyme production. This study showed considerable Fdh activity in a medium containing 25.5 mM and 4.5 mM of lactate and formate, respectively (figure III.1B). This medium, which showed to be the more appropriated to Fdh production, is hereafter named modified medium C.

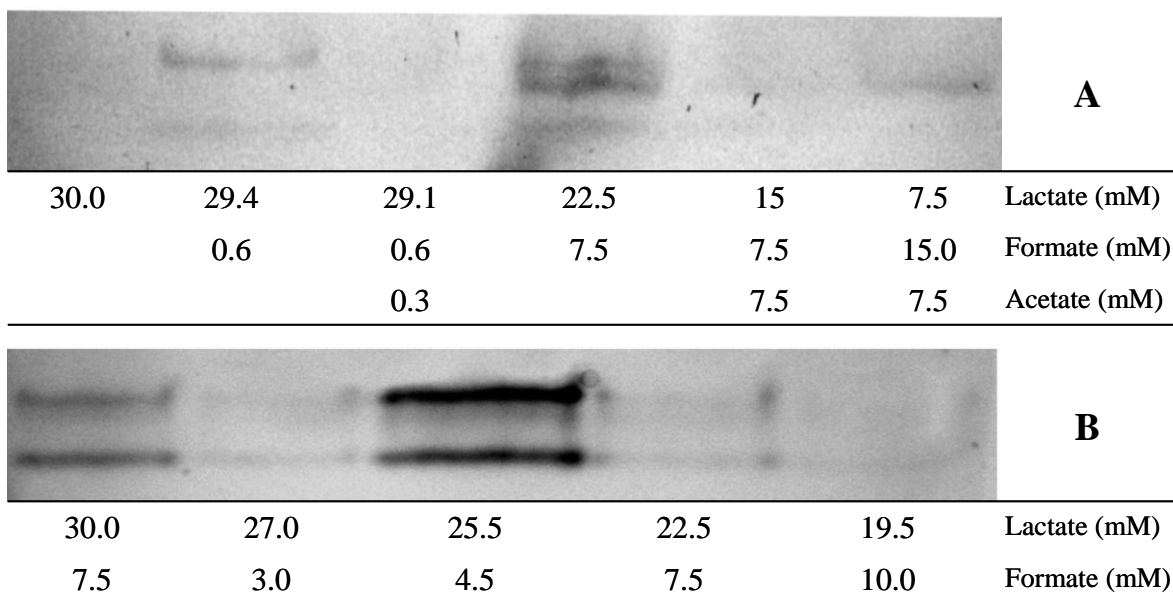


**Figure III.1| In gel Fdh activity test of *D. alaskensis* cells grown in medium C [16] with different carbon sources.** Cells cultured until the end of the exponential phase ( $OD_{600}=0.5-0.6$ ) in medium C [16] with different carbon sources, harvested and subjected to the procedure described in Material and Methods section to obtain the soluble fraction. The amount of total proteins loaded in each lane was 10  $\mu$ g. Panel (A) shows the effect of the partial replacement of lactate by formate and/or acetate, and panel (B) the optimization of formate concentration for maximal in-gel specific Fdh activity. Concentrations of lactate, acetate and formate in the culture medium for each growth condition are indicated below the respective lanes.

The influence of Mo and W ions on Fdh activity was evaluated by addition of  $\text{Na}_2\text{MoO}_4 \cdot 2\text{H}_2\text{O}$  or  $\text{Na}_2\text{WO}_4 \cdot 2\text{H}_2\text{O}$  to the modified culture medium C. It is important to note that the modified medium C without Mo/W addition contains  $0.27 \pm 0.12 \mu\text{M}$  W and no detectable Mo concentrations (ICP-AES detection limit 10 nM). The gel activity pattern of W-supplemented cell cultures showed two Fdh activity bands of similar intensity (figure III.2A). In contrast, cells cultured in modified medium C supplemented with Mo showed an upper activity band more intense than the lower band (Figure III.2B). The maximal Fdh activity was detected in the media supplemented with 10  $\mu\text{M}$  of  $\text{Na}_2\text{WO}_4 \cdot 2\text{H}_2\text{O}$ , whereas the media supplemented with Mo yielded the maximal activity using  $\text{Na}_2\text{MoO}_4 \cdot 2\text{H}_2\text{O}$  concentrations in the range of 0.045 to 1  $\mu\text{M}$  (figure 2). The media containing the highest concentration of metal (Mo and W) were chosen for the studies described below. These conditions guarantee the probable synthesis of MoCo over WCo (or viceversa) and the excess of Mo over W in the case of the molybdenum-supplemented medium (note that the modified medium C contains W of the order of 200 nM).

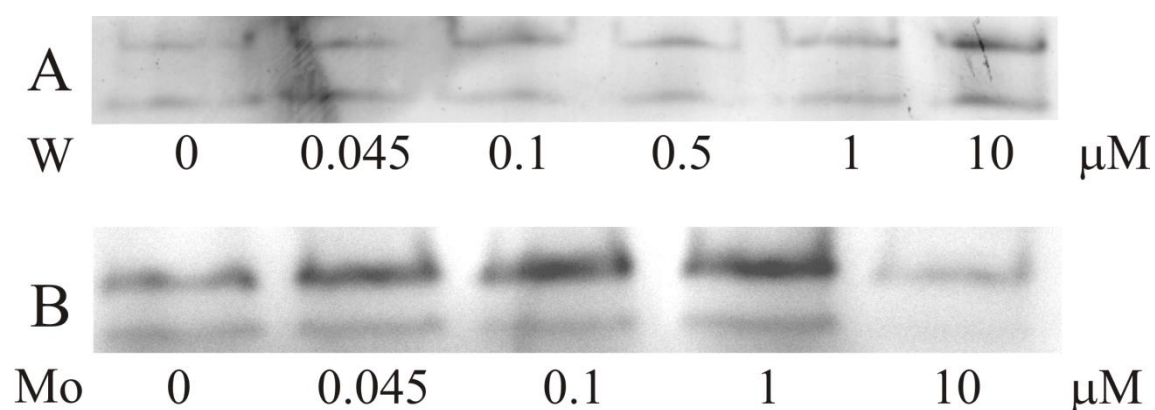


**Figure III.2| Influence of W and Mo on the Fdh activity of soluble extract of *D. alaskensis*.**

The soluble extracts were obtained as described in the Material and Methods section from cells grown until the end of the exponential phase ( $\text{OD}_{600}=0.5-0.6$ ) in modified medium C supplemented with different concentrations of  $\text{Na}_2\text{WO}_4 \cdot 2\text{H}_2\text{O}$  (A) or  $\text{Na}_2\text{MoO}_4 \cdot 2\text{H}_2\text{O}$  (B). Total amount of proteins loaded in each lane in tungstate and molybdate supplementation conditions was 10  $\mu\text{g}$  and 45  $\mu\text{g}$ , respectively.

#### ***III.4.2 Protein purification, identification and biochemical characterization.***

The differences found in the Fdh expression pattern suggested the production of more than one enzyme (figure III.2). In order to identify and characterize the different Fdhs produced by *D. alaskensis*, the enzymes were isolated from cells cultured in modified medium C supplemented with either 1  $\mu$ M molybdate or 10  $\mu$ M tungstate. As already stated in experimental procedures (section III.3), whatever Mo or W supplementation, Fdh activity was found in fractions eluted at 350 mM Tris-HCl from the first DE-52 cellulose chromatography column under Mo or W supplementation conditions. Nevertheless, when the culture medium was supplemented with Mo, an additional fraction that eluted at 200 mM Tris-HCl from the first chromatographic column exhibited Fdh activity.

From cells cultured in the presence of W, a sample containing pure Fdh was isolated as judged by SDS-PAGE (figure III.3, inset gel A, lane 1) and the  $A_{400\text{ nm}}/A_{280\text{ nm}}$  ratio of the UV-Vis spectrum (figure III.3, black line). The total yield from this purification process was 5 mg of pure protein per 300 L of cell culture. This enzyme contains  $1.1 \pm 0.1$  of W atoms per heterodimer (no Mo was detected) and has a specific activity of  $94 \pm 6$  U/mg. The as-purified protein (hereafter W-Fdh) has a molecular mass of approximately 290 kDa as determined by gel-filtration chromatography. This result together with the determination of the molecular mass of the subunits suggest that this protein is a dimer of heterodimer composed of two subunits of approximately 109 kDa (alpha subunit) and 27 kDa (beta subunit) (table III.2 and lane 1 in gel A, inset on figure III.3).

The N-terminal sequence of alpha and beta subunits showed that W-Fdh is encoded by the *Dde\_0716-0717* and *Dde\_0718* genes (hereafter called *W-fdhA* and *W-fdhB*, respectively). It is important to note that the gene encoding the alpha subunit contains a UGA codon that is specifically decoded by the selenocysteine insertion machinery. This codon was annotated as a stop codon in the *D. desulfuricans* G20 genome, which explains the reason why the *W-fdhA* gene is split into two genes (*Dde\_0716* and *Dde\_0717*). The gel activity pattern of the pure W-Fdh showed two bands (lane 1 in gel C, inset on figure III.3). To determine whether this activity pattern was an artifact or not, the bands were analyzed by SDS-PAGE and the N-terminal sequence of the isolated alpha and beta subunits of both bands was determined. The results showed that the alpha and beta subunits of both bands are coded by the *W-fdhA* and *W-fdhB* genes, respectively, indicating that the gel activity profile is an artifact, likely due to the

electrophoresis conditions. This W-Fdh was also isolated from the cells grown in medium supplemented with Mo.

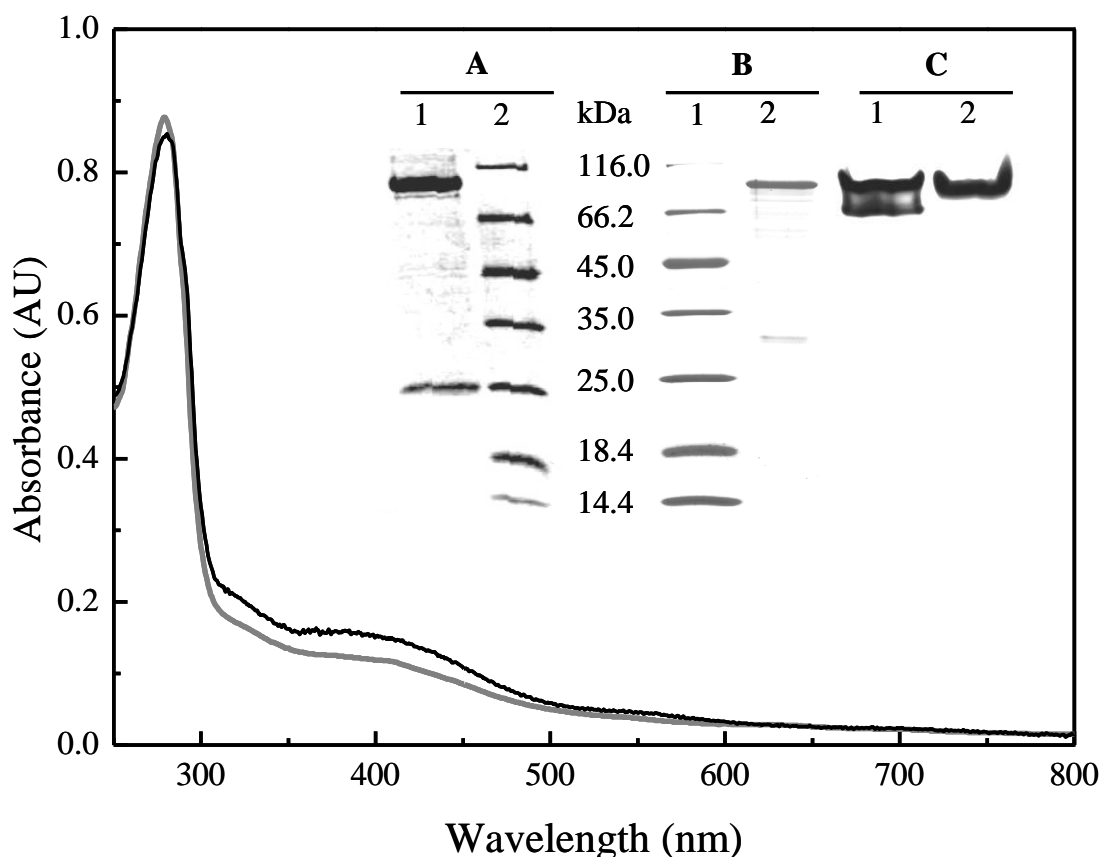


**Figure III.3| UV-visible spectrum and electrophoresis gels.** UV-visible spectrum of W-Fdh (black line) and Mo/W-Fdh (gray line) isolated from *D. alaskensis* cells. Inset: (A) SDS-PAGE of W-Fdh (lane 1, 2  $\mu$ g) and molecular weight markers (lane 2); (B) SDS-PAGE of molecular weight markers (line 1) and Mo/W-Fdh (lane 2, 1  $\mu$ g); (C) in-gel activity of the as-purified W-Fdh (lane 1, 2  $\mu$ g) and Mo/W-Fdh (lane 2, 9  $\mu$ g).

As mentioned above, cells cultured in the presence of Mo yielded an extra Fdh activity fraction that eluted at lower ionic strength (200 mM Tris HCl) from the first chromatographic column. The purification protocol described in the section III.3.3 allowed the isolation of 5.5 mg of Fdh from a 300 L cell culture. This enzyme had a specific activity of  $4.65 \pm 0.07$  U/mg and was isolated as a heterodimer of approximately 146 kDa constituted by an alpha and a beta subunit (lane 2 in gel B, inset on figure III.3). Activity gels of this enzyme showed a unique band (lane 2 in gel C, inset on figure III.3) and metal content analysis detected  $0.35 \pm 0.02$  Mo atoms and  $0.53 \pm 0.03$  W atoms per heterodimer. This Fdh is hereafter named Mo/W-Fdh. Amino acid

sequence of the alpha and beta subunit matched with the translated amino acid sequence of the *Dde\_3512-3513* and *Dde\_3514* genes (hereafter called *Mo/W-fdhA* and *Mo/W-fdhB*, respectively). As for the W-Fdh, the Mo/W-Fdh contains a selenocysteine, explaining the genome annotation (*Dde\_3512* and *Dde\_3513*) for the alpha subunit. The molecular weight of the alpha and beta subunits calculated from the translated amino acid sequences were 109 and 28 kDa, respectively (table III.2). The biochemical properties of this enzyme indicated that corresponds to the Fdh isolated by Brondino *et al* [17].

**Table III.2|** Biochemical properties of Fdhs isolated from *D. alaskensis*.

	Mo/	W/	MW (as isolated, kDa)	Subunits (kDa)*		Specific activity (U/mg)
	molecule	molecule		$\alpha$	$\beta$	
Mo/W-Fdh	0.35±0.02	0.53±0.03	146	109	28	4.65±0.07
W-Fdh	n.d.	1.1±0.1	290	109	27	94±6

*n.d* (not detected)

\* Molecular weights calculated from the amino acid sequence.

Both Mo/W-Fdh and W-Fdh proteins contain the guanidine form of the pyranopterin cofactor and exhibit UV-visible spectra with a shoulder at 320 nm and an absorbance band at 400 nm typical of proteins containing [4Fe-4S] metal clusters (figure III.3). The isoelectric points calculated from the translated amino acid sequence were 6.92 and 7.84 for the W-Fdh and the Mo/W-Fdh, respectively. The differences between the pI values can explain the complete separation of both proteins by the anionic exchange chromatography column used as the first purification step. The biochemical properties of both Fdhs are summarized in table III.2.

The third soluble Fdh encoded by the *Dde\_0812-Dde\_0813* genes (hereafter called *fdh3*) was not detected under the growth condition tested in this study.



### ***III.4.3 Gene expression analysis***

The production of the enzymes was also evaluated at the transcriptional level by qRT-PCR. The expression levels of the genes *Mo/W-fdhA*, *W-fdhA* and *fdh3A* were measured in *Desulfovibrio alaskensis* grown in modified medium C without metal supplementation (control) and in the presence of 1  $\mu\text{M}$  Mo or 10  $\mu\text{M}$  W. When cells were grown in modified medium C without metal supplementation, transcripts corresponding to both *W-fdhA* and *Mo/W-fdhA* genes were detected. However, the amount of *Mo/W-fdhA* transcripts was found about 6-fold lower than that of *W-fdhA* (data not shown). These results are in line with the concentration of W found in the modified medium C.

In contrast, cells cultured in modified medium C supplemented with Mo showed a slight up-regulation of the *Mo/W-fdhA* gene (figure III.4), which is in agreement with the detection of a Mo/W-Fdh different to the W-Fdh isolated from cells cultured under W-supplementation conditions. Under these Mo-excess conditions, it was observed a down-regulation of the *W-fdhA* gene of about 4 times (figure III.4). On the other hand, addition of tungstate to the culture medium induced a strong down-regulation of *Mo/W-fdhA* gene (about 60 times) and no significant effect on *W-fdhA* gene (figure III.4). No significant amounts of transcripts could be detected for the *fdh3A* gene under the growth conditions tested, which suggests that this gene was not expressed or expressed at a very low level.

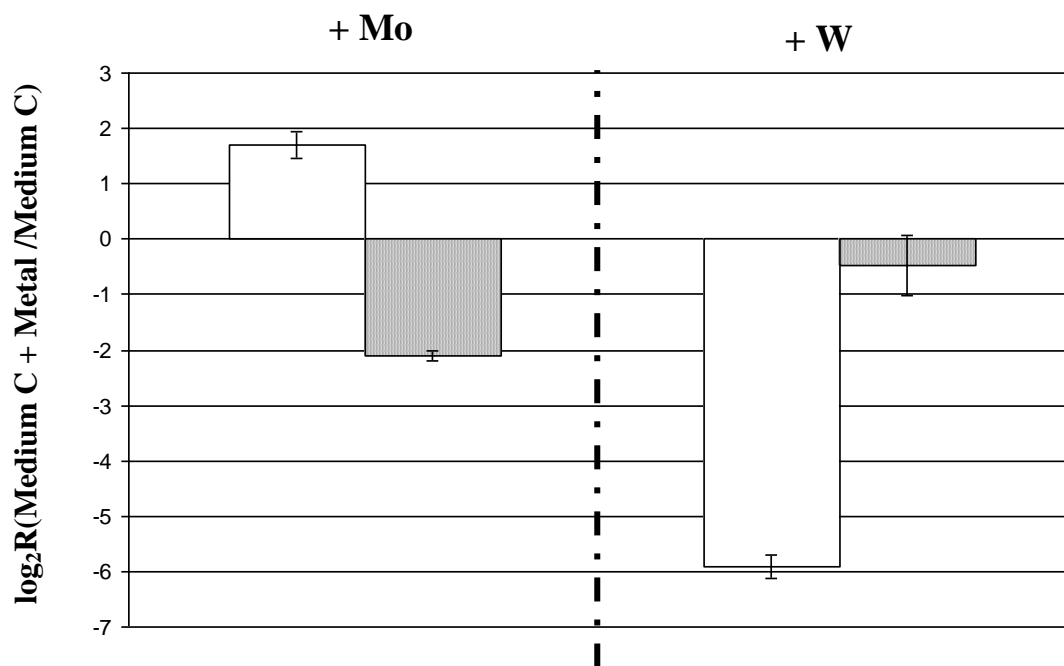


**Figure III.4| Influence of metal in Fdh expression.** Relative gene expression of *Mo/W-fdh* and *w-fdh* depending on metal supplementation. Ratio of transcripts abundance of *Mo/W-fdhA* (*Dde\_3513*) (□) or *W-fdhA* (*Dde\_0717*) (▨) from *D. alaskensis* cultured in modified medium C supplemented with either 1μM molybdate or 10μM tungstate *versus* culture in modified medium C without metal supplementation.

The expression levels of genes involved in molybdate transport (*modA* and *modB*) and tungstate (*tupA* and *tupB*) were also evaluated in the growth conditions tested. When cells were cultured in modified medium C without metal supplementation, the expression level of *modA* and *modB* genes were similar. In contrast, the expression level of *tupA* and *tupB* genes was strongly different, with *tupA* being about 230-fold more expressed than *tupB* (data not shown). These data suggest that *modA* and *modB* genes belong to the same transcriptional unit (*modABC*) as commonly is predicted for these gene clusters. In contrast, the different expression level of *tupA* and *tupB* genes indicated that they do not belong to the same transcriptional unit, as also predicted by *in silico* analysis. In light of these results, we decided to use *modB* and *tupB* as markers for the expression level of the molybdate and tungstate transport systems, respectively.

Comparison of *modB* and *tupB* expression in cells cultured in modified medium C without metal supplementation revealed that *modB* gene was about 22-fold less expressed than *tupB* gene (data not shown). Addition of molybdate to the culture medium induced a down-regulation of *modB* gene (6-fold) while *tupB* gene expression

was only very slightly affected (figure III.5). In contrast, a strong repression of both genes was observed upon tungstate addition, with *modB* being the most repressed gene (figure III.5).

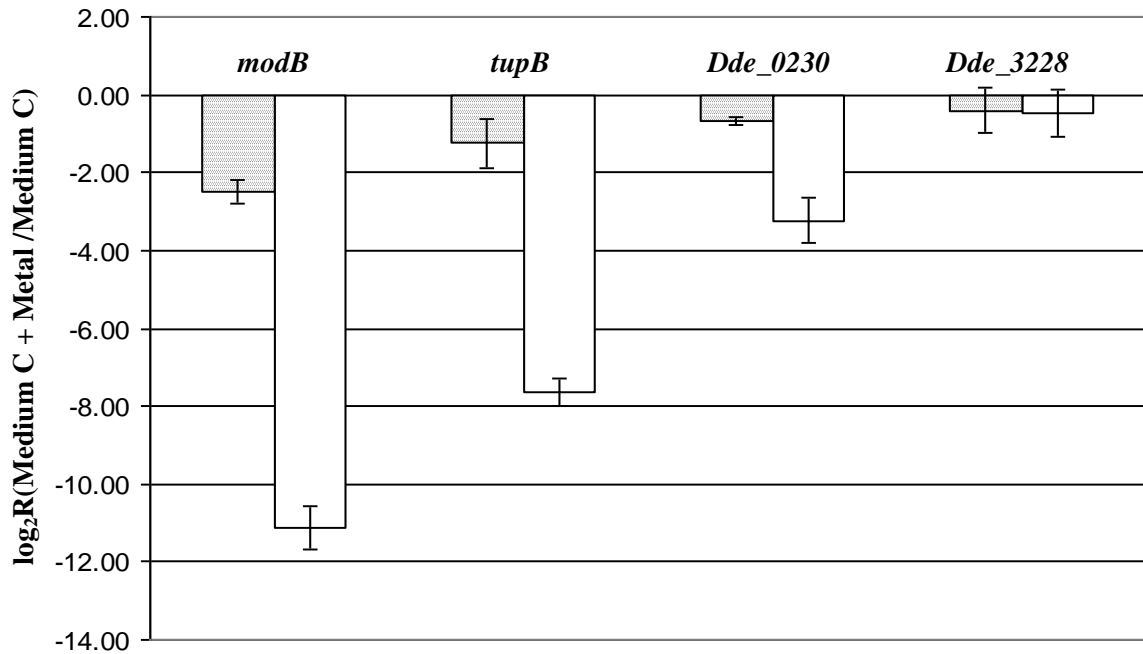


**Figure III.5| Influence of metal in transporters and MoeA expression.** Relative expression of *modB* (*Dde\_3519*) and *tupB* (*Dde\_0233*) genes encoding proteins responsible for Mo and W transport and *moeA1* (*Dde\_0230*) and *moeA2* (*Dde\_3228*) genes putatively involved in the selective incorporation of Mo or W in the cofactor [24,29] as determined by using quantitative real-time PCR. The abundance of transcripts was determined from *D. alaskensis* cells cultured until the end of the exponential phase ( $OD_{600}=0.5-0.6$ ) in modified medium C supplemented with either 1  $\mu$ M Mo (▨) or 10  $\mu$ M W (□) and in modified medium C without metal addition.

The effects of both ions on the expression levels of genes coding for putative MoeA proteins (*moeA1/Dde\_0230* and *moeA2/Dde\_3228*), which are proposed to be involved in incorporation of the metal into the Fdh cofactor, were also tested. The results showed that *moeA1* was significantly down-regulated in the presence of tungstate, whereas the expression level of the *moeA2* was not significantly affected upon Mo or W supplementation (figure III.5).

**III.5 Discussion**

Molybdenum and tungsten occurrence in the active site of Fdhs is a very interesting issue in this family of enzymes. In this sense, despite the fact that these metal atoms share similar chemical properties, it is still unknown why highly homologous enzymes catalyzing the same reaction and that are isolated from closely related organisms preferentially incorporate either Mo or W in the active site [3,7,9,13,35].

Analysis of the genome of *D. desulfuricans* G20 revealed that this organism encodes for at least three Fdhs, all of them composed of one alpha and one beta subunit (figure III.6). In this work we showed that *D. alaskensis* grown in modified medium C supplemented with W produces one of these Fdhs, the W-Fdh encoded by the *W-fdh* genes. Cells cultured in Mo-supplemented medium produce, in addition to the W-Fdh, the Mo/W-Fdh encoded by the *Mo/W-fdh* genes. Remarkably, Mo/W-Fdh from *D. alaskensis* was the first Fdh example able to incorporate either Mo or W [17].

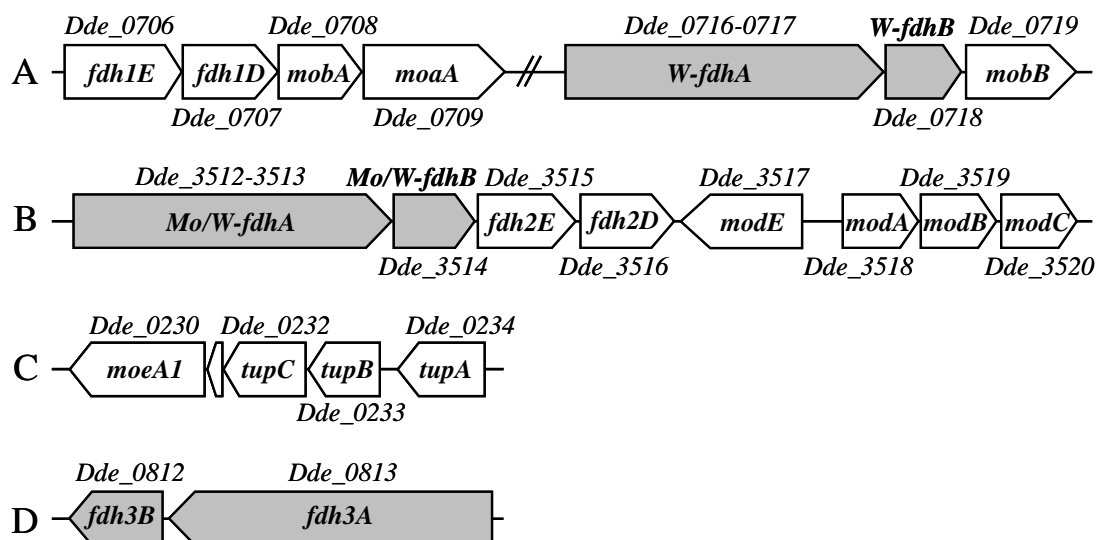


**Figure III.6 Organization of the *fdh* genes, elements putatively involved in molybdenum transport and metal cofactor biosynthesis and incorporation present in the *fdh* genes surrounding area.** (A) *fdh1E* and *fdh1D* genes encode for proteins probably involved in Fdh formation, *MobA* gene codes for a protein that catalyzes the conversion of MPT to MGD, *moaA* gene codes for a protein that catalyzes the conversion of GTP into cyclic pyranopterin monoPhosphate (precursor Z), *W-fdhA* and *W-fdhB* genes encoding the alpha and beta subunits of the W-Fdh, respectively. *Dde\_0719* gene encodes a protein homologous to MobB which binds GTP and has weak GTPase activity [36]. (B) *Mo/W-fdhA* and *Mo/W-fdhB* genes encoding the alpha and beta subunits of the Mo/W-Fdh. The *modABC* genes encode the molybdate uptake transport system. The *modE* encodes a protein that regulates the *modABC* operon expression [30,37,38]. (C) *Dde\_0230* gene encodes a homologous MoeA protein involved in Mo/W insertion into the MPT. *Dde\_0232-Dde\_0234* genes codify for an ABC-type tungstate transport system (TupA, TupB, and TupC) similar to the *modABC* gene cluster. (D) *fdh3A* and *fdh3B* genes encoding a third putative periplasmic Fdh.

The slight up-regulation of the *Mo/W-fdh* genes on Mo-supplementation (figure III.4) suggests that the Mo/W-Fdh enzyme, despite the W incorporation, should preferentially work with Mo. This hypothesis is supported by the strong down-regulation of the *Mo/W-fdh* genes in cells grown under W-supplementation conditions (figure III.4). Therefore, the fact that tungsten is also detected in the Mo/W-Fdh could be due to a constitutive synthesis of the W-cofactor and an unspecific incorporation into the enzyme. In line with the latter, the W-Fdh was also found in cells grown in modified medium C supplemented with Mo, showing that the W-cofactor is even synthesized despite the molybdenum excess. The specific activity of the Mo/W-Fdh ( $4.65 \pm 0.07$

U/mg) is at least one order of magnitude smaller than those determined for Mo-Fdhs from other *Desulfovibrio* species [7,9,10], which indicates a low efficiency for catalysis. In contrast to the Mo/W-Fdh, the enzyme encoded by the *W-fdh* gene incorporates exclusively W. This is supported by the fact that only tungsten was detected in the as-purified enzyme independently of the metal added to the culture medium, and also by the down-regulation of the *W-fdh* gene observed in the presence of an excess of Mo. The specific activity determined for the W-Fdh ( $94 \pm 6$  U/mg) is comparable with that determined for the homologous *D. gigas* W-Fdh (77 U/mg).

The hypothesis that the MoeA proteins are involved in the selective incorporation of Mo or W [24,29] was analyzed by measuring the expression levels of *moeA1* and *moeA2* genes under the conditions optimized to produce Mo/W-Fdh and W-Fdh. The results did not give clear clues on the selectivity of MoeA proteins for a given metal ion (figure III.5). Nevertheless, taking into account the mechanism of Mo cofactor biosynthesis and insertion [23,24,29,39], one may hypothesize that the complexes MoaB/MoeA/M (M= Mo or W) interact with the protein-chaperone complex, likely FdhA/FdhD, in the last step of Fdh maturation. A more specific interaction between MoaB/MoeA/W and W-FdhA/FdhD would lead to the selective incorporation of the W-cofactor, which would not be the case of Mo/W-Fdh. Although the chaperone encoded by *fdhE*, also present in the *fdh* genes surrounding area (figure III.6), was demonstrated to interact with the catalytic subunit of respiratory Fdhs from *E. coli* [40], this gene is only linked to periplasmic Tat-targeted enzymes [41-44]. Since Moco containing Fdhs can also be located in the cytoplasm, it is unlikely that FdhE plays a specific and relevant role in metal insertion.

The Mo and W transport systems in *D. desulfuricans* G20 are encoded by the *mod* and *tup* genes (figure III.6). Analysis of the gene expression levels in *D. alaskensis* showed that both *mod* and *tup* genes are down-regulated in the presence of either molybdate or tungstate in the culture medium (figure III.5). However, *tup* genes appeared to be more expressed than *mod* genes in modified medium C without metal addition (data not shown). This differential gene expression is more important when the culture medium is supplemented with W. These data are in agreement with the biochemical results, which showed that W-Fdh was produced in all cases analyzed in this paper.

The down-regulation of *mod* and *tup* genes on metal supplementation is also in line with the regulation of the *modABC* operon reported for *E. coli* [30]. In this organism, the

expression of such operon is repressed under micromolar concentrations of molybdate and only induced under conditions of molybdate starvation.

Formate dehydrogenases from *D. alaskensis* represent an interesting system to study the genes involved in the biosynthesis and incorporation of the Mo and W cofactors in enzymes (table III.3 shows a list of annotated proteins, from *D. desulfuricans* G20 genome, putatively involved in Mo-cofactor biosynthesis). In the present work it was demonstrated that although the production of Fdh isoforms is influenced by the Mo or W concentration in the culture medium, metal incorporation seems to be independent of the presence of any of these metal ions. This differential gene regulation of genes encoding respiration processes and genes involved in Mo/W transport and cofactor biosynthesis are in line with data reported for *E. coli* [38]. The interaction of the cofactor biosynthesis proteins with the apoenzyme-chaperone complex could be the key for specific or unspecific Mo/W insertion.

**Table III.3** | Proteins (putatively) involved in Mo-cofactor biosynthesis annotated in the genome of *D. desulfuricans* G20.

<b>Putative Protein</b>	<b>Locus Tag</b>	<b>Proposed Function</b>
MoaA	Dde_0709	Conversion of GTP into cPMP <sup>1</sup> (precursor Z)
MoaC	Dde_0249	Conversion of GTP into cPMP <sup>1</sup> (precursor Z)
MoaB	Dde_1390	Adenylation of MPT for Mo/W insertion
MoeB	Dde_2459	Adenylation of the MoaD
	Dde_0229	Phosphoesterase: Probable MogA <sup>2</sup> -like function
MoeA	Dde_0230	Mo/W insertion into the MPT <sup>3</sup>
MoeA	Dde_3228	Mo/W insertion into the MPT <sup>3</sup>
MobA	Dde_3547	Conversion of MPT to MGD <sup>4</sup>
	Dde_3116	Nucleotidyltransferase activity
MobB	Dde_0719	GTP binding protein. Weak GTPase activity
	Dde_3538	MoCo cytidyltransferase: MCD <sup>5</sup> synthesis

<sup>1</sup> Cyclic Pyranopterin MonoPhosphate.<sup>2</sup> MogA: protein involved in Adenylation of MPT for Mo/W insertion.<sup>3</sup> Metal-binding pterin.<sup>4</sup> Molybdopterin Guanosine Dinucleotide.<sup>5</sup> Molybdopterin Cytidine Dinucleotide.



## III.6 References

- 1 May, H. D., Patel, P. S. & Ferry, J. G. Effect of molybdenum and tungsten on synthesis and composition of formate dehydrogenase in *Methanobacterium formicum*. J Bacteriol 170, 3384-3389, (1988).
- 2 Afshar, S., Kim, C., Monbouquette, H. G. & Schroder, I. I. Effect of tungstate on nitrate reduction by the hyperthermophilic archaeon *pyrobaculum aerophilum*. Appl Environ Microbiol 64, 3004-3008, (1998).
- 3 Sevcenco, A. M., Bevers, L. E., Pinkse, M. W., Krijger, G. C., Wolterbeek, H. T., Verhaert, P. D., Hagen, W. R. & Hagedoorn, P. L. Molybdenum incorporation in tungsten aldehyde oxidoreductase enzymes from *Pyrococcus furiosus*. J Bacteriol 192, 4143-4152, (2010).
- 4 Stewart, L. J., Bailey, S., Bennett, B., Charnock, J. M., Garner, C. D. & McAlpine, A. S. Dimethylsulfoxide reductase: an enzyme capable of catalysis with either molybdenum or tungsten at the active site. J Mol Biol 299, 593-600, (2000).
- 5 Bertram, P. A., Schmitz, R. A., Linder, D. & Thauer, R. K. Tungstate can substitute for molybdate in sustaining growth of *Methanobacterium thermoautotrophicum*. Identification and characterization of a tungsten isoenzyme of formylmethanofuran dehydrogenase. Arch Microbiol 161, 220-228, (1994).
- 6 Hochheimer, A., Hedderich, R. & Thauer, R. K. The formylmethanofuran dehydrogenase isoenzymes in *Methanobacterium wolfei* and *Methanobacterium thermoautotrophicum*: induction of the molybdenum isoenzyme by molybdate and constitutive synthesis of the tungsten isoenzyme. Arch Microbiol 170, 389-393, (1998).
- 7 Costa, C., Teixeira, M., LeGall, J., Moura, J. J. G. & Moura, I. Formate dehydrogenase from *Desulfovibrio desulfuricans* ATCC27774: isolation and spectroscopic characterization of the active sites (heme, iron- sulfur centers and molybdenum). J Biol Chem 2, 198-208, (1997).
- 8 George, G. N., Costa, C., Moura, J. J. G. & Moura, I. Observation of Ligand-Based Redox Chemistry at the Active Site of a Molybdenum Enzyme. J Am Chem Soc 121, 2625-2626, (1999).

- 9 Rivas, M. G., Gonzalez, P. J., Brondino, C. D., Moura, J. J. & Moura, I. EPR characterization of the molybdenum(V) forms of formate dehydrogenase from *Desulfovibrio desulfuricans* ATCC 27774 upon formate reduction. *J Inorg Biochem* 101, 1617-1622, (2007).
- 10 Sebban, C., Blanchard, L., Bruschi, M. & Guerlesquin, F. Purification and characterization of the formate dehydrogenase from *Desulfovibrio vulgaris* Hildenborough. *FEMS Microbiol Lett* 133, 143-149, (1995).
- 11 ElAntak, L., Dolla, A., Durand, M. C., Bianco, P. & Guerlesquin, F. Role of the tetrahemic subunit in *Desulfovibrio vulgaris* hildenborough formate dehydrogenase. *Biochemistry* 44, 14828-14834, (2005).
- 12 Sebban-Kreuzer, C., Dolla, A. & Guerlesquin, F. The formate dehydrogenase-cytochrome c553 complex from *Desulfovibrio vulgaris* Hildenborough. *Eur J Biochem* 253, 645-652, (1998).
- 13 Almendra, M. J., Brondino, C. D., Gavel, O., Pereira, A. S., Tavares, P., Bursakov, S., Duarte, R., Caldeira, J., Moura, J. J. & Moura, I. Purification and characterization of a tungsten-containing formate dehydrogenase from *Desulfovibrio gigas*. *Biochemistry* 38, 16366-16372, (1999).
- 14 Raaijmakers, H., Macieira, S., Dias, J. M., Teixeira, S., Bursakov, S., Huber, R., Moura, J. J., Moura, I. & Romao, M. J. Gene sequence and the 1.8 Å crystal structure of the tungsten-containing formate dehydrogenase from *Desulfovibrio gigas*. *Structure* 10, 1261-1272, (2002).
- 15 Raaijmakers, H., Teixeira, S., Dias, J. M., Almendra, M. J., Brondino, C. D., Moura, I., Moura, J. J. & Romao, M. J. Tungsten-containing formate dehydrogenase from *Desulfovibrio gigas*: metal identification and preliminary structural data by multi-wavelength crystallography. *J Biol Inorg Chem* 6, 398-404, (2001).
- 16 Postgate, J. The sulphate-reducing bacteria. 2nd edn, Vol. 130 (Cambridge University Press, 1984).
- 17 Brondino, C. D., Passeggi, M. C., Caldeira, J., Almendra, M. J., Feio, M. J., Moura, J. J. & Moura, I. Incorporation of either molybdenum or tungsten into formate dehydrogenase from *Desulfovibrio alaskensis* NCIMB 13491; EPR assignment of the proximal iron-sulfur cluster to the pterin cofactor in formate

- dehydrogenases from sulfate-reducing bacteria. *J Biol Inorg Chem* 9, 145-151, (2004).
- 18 Rivas, M. G., Carepo, M. S., Mota, C. S., Korbas, M., Durand, M. C., Lopes, A. T., Brondino, C. D., Pereira, A. S., George, G. N., Dolla, A., Moura, J. J. & Moura, I. Molybdenum induces the expression of a protein containing a new heterometallic Mo-Fe cluster in *Desulfovibrio alaskensis*. *Biochemistry-Us* 48, 873-882, (2009).
- 19 Chhabra, S. R., He, Q., Huang, K. H., Gaucher, S. P., Alm, E. J., He, Z., Hadi, M. Z., Hazen, T. C., Wall, J. D., Zhou, J., Arkin, A. P. & Singh, A. K. Global analysis of heat shock response in *Desulfovibrio vulgaris* Hildenborough. *J Bacteriol* 188, 1817-1828, (2006).
- 20 Wall, J. & Krumholz, L. Uranium reduction. *Annu Rev Microbiol* 60, 149-166, (2006).
- 21 Sargent, F., Bogsch, E. G., Stanley, N. R., Wexler, M., Robinson, C., Berks, B. C. & Palmer, T. Overlapping functions of components of a bacterial Sec-independent protein export pathway. *EMBO J* 17, 3640-3650, (1998).
- 22 Berks, B. C., Sargent, F., De Leeuw, E., Hinsley, A. P., Stanley, N. R., Jack, R. L., Buchanan, G. & Palmer, T. A novel protein transport system involved in the biogenesis of bacterial electron transfer chains. *Biochim Biophys Acta* 1459, 325-330, (2000).
- 23 Schwarz, G., Mendel, R. R. & Ribbe, M. W. Molybdenum cofactors, enzymes and pathways. *Nature* 460, 839-847, (2009).
- 24 Bevers, L. E., Hagedoorn, P. L. & Hagen, W. R. The bioinorganic chemistry of tungsten. *Coordin Chem Rev* 253, 269-290, (2009).
- 25 Mendel, R. R. Biology of the molybdenum cofactor. *J Exp Bot* 58, 2289-2296, (2007).
- 26 Nichols, J. D. & Rajagopalan, K. V. In vitro molybdenum ligation to molybdopterin using purified components. *J Biol Chem* 280, 7817-7822, (2005).
- 27 Nichols, J. & Rajagopalan, K. V. *Escherichia coli* MoeA and MogA. Function in metal incorporation step of molybdenum cofactor biosynthesis. *J Biol Chem* 277, 24995-25000, (2002).
- 28 Llamas, A., Otte, T., Multhaup, G., Mendel, R. R. & Schwarz, G. The Mechanism of nucleotide-assisted molybdenum insertion into molybdopterin. A

- novel route toward metal cofactor assembly. *J Biol Chem* 281, 18343-18350, (2006).
- 29 Bevers, L. E., Hagedoorn, P. L., Santamaria-Araujo, J. A., Magalon, A., Hagen, W. R. & Schwarz, G. Function of MoaB proteins in the biosynthesis of the molybdenum and tungsten cofactors. *Biochemistry* 47, 949-956, (2008).
- 30 Grunden, A. M. & Shanmugam, K. T. Molybdate transport and regulation in bacteria. *Arch Microbiol* 168, 345-354, (1997).
- 31 Maupin-Furlow, J. A., Rosentel, J. K., Lee, J. H., Deppenmeier, U., Gunsalus, R. P. & Shanmugam, K. T. Genetic analysis of the modABCD (molybdate transport) operon of *Escherichia coli*. *J Bacteriol* 177, 4851-4856, (1995).
- 32 Gremer, L. & Meyer, O. Characterization of xanthine dehydrogenase from the anaerobic bacterium *Veillonella atypica* and identification of a molybdopterin-cytosine-dinucleotide-containing molybdenum cofactor. *Eur J Biochem* 238, 862-866, (1996).
- 33 Frunzke, K., Heiss, B., Meyer, O. & Zumft, W. G. Molybdopterin Guanine Dinucleotide Is the Organic Moiety of the Molybdenum Cofactor in Respiratory Nitrate Reductase from *Pseudomonas stutzeri*. *FeMS Microbiol Lett* 113, 241-246, (1993).
- 34 Pfaffl, M. W. A new mathematical model for relative quantification in real-time RT-PCR. *Nucleic Acids Res* 29, e45, (2001).
- 35 Boyington, J. C., Gladyshev, V. N., Khangulov, S. V., Stadtman, T. C. & Sun, P. D. Crystal structure of formate dehydrogenase H: catalysis involving Mo, molybdopterin, selenocysteine, and an Fe<sub>4</sub>S<sub>4</sub> cluster. *Science* 275, 1305-1308, (1997).
- 36 Eaves, D. J., Palmer, T. & Boxer, D. H. The Product of the Molybdenum Cofactor Gene *mobB* of *Escherichia Coli* is a GTP-Binding Protein. *Eur J Biochem* 246, 690-697, (1997).
- 37 Grunden, A. M., Ray, R. M., Rosentel, J. K., Healy, F. G. & Shanmugam, K. T. Repression of the *Escherichia coli* modABCD (molybdate transport) operon by ModE. *J Bacteriol* 178, 735-744, (1996).
- 38 Rech, S., Deppenmeier, U. & Gunsalus, R. P. Regulation of the molybdate transport operon, modABCD, of *Escherichia coli* in response to molybdate availability. *J Bacteriol* 177, 1023-1029, (1995).

- 39 Vergnes, A., Gouffi-Belhabich, K., Blasco, F., Giordano, G. & Magalon, A. Involvement of the molybdenum cofactor biosynthetic machinery in the maturation of the *Escherichia coli* nitrate reductase A. *J Biol Chem* 279, 41398-41403, (2004).
- 40 Luke, I., Butland, G., Moore, K., Buchanan, G., Lyall, V., Fairhurst, S. A., Greenblatt, J. F., Emili, A., Palmer, T. & Sargent, F. Biosynthesis of the respiratory formate dehydrogenases from *Escherichia coli*: characterization of the FdhE protein. *Arch Microbiol* 190, 685-696, (2008).
- 41 Berks, B. C., Palmer, T. & Sargent, F. The Tat protein translocation pathway and its role in microbial physiology. *Adv Microb Physiol* 47, 187-254, (2003).
- 42 Mandrand-Berthelot, M. A., Couchoux-Luthaud, G., Santini, C. L. & Giordano, G. Mutants of *Escherichia coli* specifically deficient in respiratory formate dehydrogenase activity. *J Gen Microbiol* 134, 3129-3139, (1988).
- 43 Palmer, T., Sargent, F. & Berks, B. C. Export of complex cofactor-containing proteins by the bacterial Tat pathway. *Trends Microbiol* 13, 175-180, (2005).
- 44 Turner, R. J., Papish, A. L. & Sargent, F. Sequence analysis of bacterial redox enzyme maturation proteins (REMPs). *Can J Microbiol* 50, 225-238, (2004).



# Chapter IV

*The mechanism of formate oxidation by Fdh.*

## IV.1 Summary

The active site of metal-dependent Fdh from prokaryotic organisms in the oxidized state comprises Mo or W ion, in a distorted octahedral geometry, hexacoordinated by four sulfur atoms from two pyranopterin molecules, selenium from a selenocysteine residue, and a sulfur atom that was formerly proposed to be an oxo or hydroxo leaving group. Using this structural model, the catalytic mechanism of Fdh has been calculated through DFT tools. This simulated mechanism was correlated with the experimental kinetic properties of both three different Fdh isolated from three different *Desulfovibrio* species and data available in the literature. Our studies indicate that the formate C-H bond break is an event involved in the rate-limiting step of the catalytic cycle and that changing Mo for W in the active site does not affect the turnover rates. Furthermore, the roles of conserved amino acids residues near the active site have been studied and discussed on the basis of theoretical and experimental results.

## IV.2 Introduction

Although several reaction mechanisms based on crystal structures and other experimental data were proposed, the catalytic mechanism of Mo- and W-enzymes remains unclear. To date, two hypothesis were postulated differing in the occurrence of a direct coordination [1] or not [2] of a SeCys residue to the molybdenum metal during catalysis.

The first crystal structure of both oxidized and reduced Fdh-H suggested that the oxidized Mo(VI) form is hexacoordinated by four sulfur atoms from the pyranopterins a selenium from the SeCys140 residue and a hydroxyl group. In the reduced Mo(IV) form, the bond with the hydroxyl group is broken yielding a pentacoordinated molybdenum site. The oxidized Mo(VI) form in complex with a nitrite inhibitor molecule shows that the oxygen atom from nitrite is coordinated to Mo and hydrogen bonded to the positive conserved Arg333 residue (figure IV.1) [1]. Although the structure of a reduced Fdh was only determined for *Ec* Fdh-H, spectroscopic studies performed in the Fdh from *D. desulfuricans* ATCC 27774 suggest that all Mo-dependent Fdh present similar characteristics in their oxidized and reduced states [3,4].



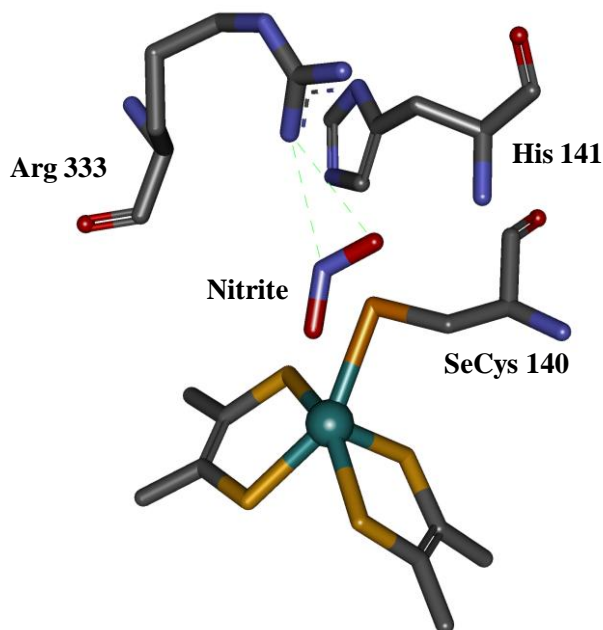


**Figure IV.1|***E. coli* Fdh-H active site in the presence of nitrite. Fdh structure at 2.9Å (PDB code:1FDI) [1].

According with crystallographic data, Boyington *et al* proposed the reaction mechanism showed in figure IV.2A [1]. The catalysis starts with the coordination of the oxygen atom from the formate molecule to molybdenum, replacing the OH ligand. Weak interactions are established between the formate and the nearby residues His141 and Arg333. The selenium atom abstracts the proton by cleaving the C-H bond in the substrate and two electrons are transferred to the Mo ion. This step of the mechanism is supported by kinetic and spectroscopic data [1,5]. Upon oxidation, the proton is most likely transferred from the SeCys140 to the His141 residue. The Mo(VI) form is restored by another step, transferring the two electrons to the [4Fe-4S] cluster through the MGD moiety.

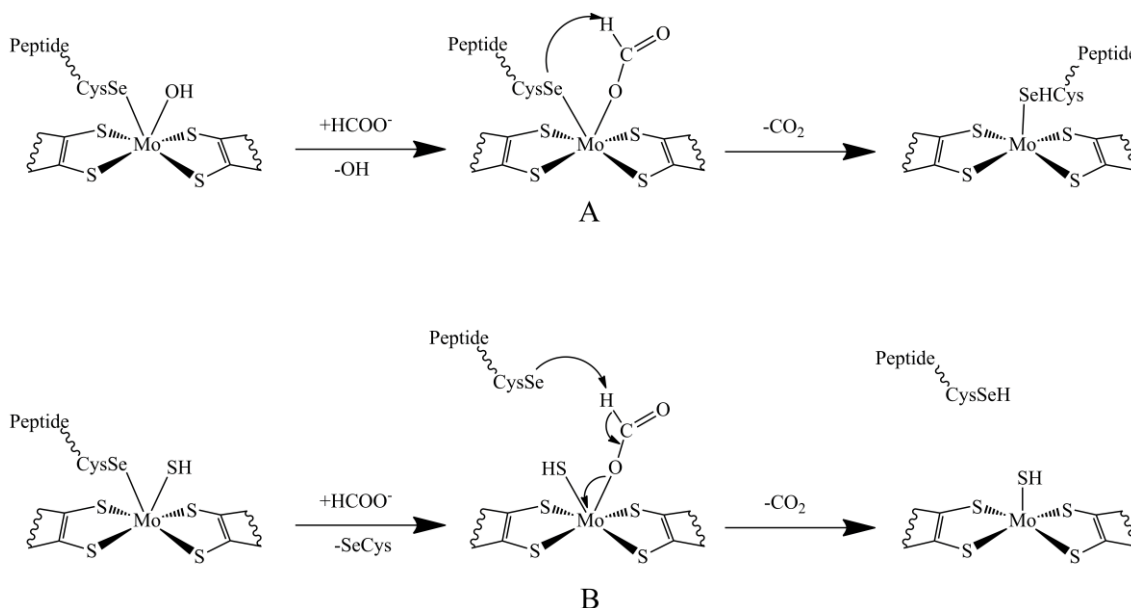


**Figure IV.2| Reaction mechanisms proposed for the oxidation of formate to carbon dioxide by Fdhs.** (A) Mechanism proposed by Boyington *et al* where the SeCys remains bonded to the Mo atom during the catalysis [1]. (B) Mechanism proposed by Raaijmakers *et al* where the SeCys bond is replaced by a formate molecule in the first step of the reaction[2].

To study the Se relevance on formate oxidation, SeCys was replaced for a Cys by directed mutagenesis [6]. Kinetic studies demonstrated that reaction rate decreases in the Fdh-H mutant and that the formate reduced enzyme is completely inactivated when is incubated with iodoacetamide [6]. In addition, the inactivation of the enzyme was demonstrated to be pH-dependent and the pH value at which the enzyme is inactive correlates with the *pKa* value of the ionized selenol [6]. All these results demonstrated that Se is essential in the formate reduction by Fdhs.

More recently, the crystal structure of the formate-reduced *Ec* Fdh-H was reinterpreted by Raaijmakers *et al* [2]. In this structure, the selenium atom from SeCys140 residue is unbound from molybdenum (12 Å away from the metal atom) and the positive charge from the Arg333 stabilizes the negative selenol group. In addition, a SH group (or  $\text{S}^{2-}$ ) is identified as the apical ligand of the Mo ion instead of a hydroxyl/water ligand [2].

Taking into account these new data, Raaijmakers *et al* proposed a new mechanism for the formate oxidation which is reported in figure IV.2B [2]. In this proposal, the formate binding displaces the SeCys ligand which is stabilized by the Arg333 residue. Then, the SeCys abstract the formate proton, the  $\text{CO}_2$  is released and two electrons are transferred to the Mo yielding a pentacoordinated species. Electrons are then transferred from Mo

(IV) to the proximal [4Fe-4S] cluster and the catalytic site is regenerated. The crucial role of the SeCys is supported by experimental data previously referred [6].

Both mechanisms were assessed by Leopoldini *et al* using theoretical and computational means [7]. These authors concluded that the SeCys residue is the proton accepting group during the formate oxidation and that the reaction of proton transfer from the substrate to the Se atom is kinetic and thermodynamically more favorable when the SeCys residue is not coordinated to the Mo ion (19 kcal/mol) compared to the mechanism in which it was considered that the SeCys residue remain bound to the Mo ion (36 kcal/mol) [1,7]. However, Leopoldini *et al* only studied the proton abstraction reaction, and avoided in their analysis essential aspects for the catalysis such as the role of the conserved histidine and arginine residues, as well as the processes of substrate binding and product release.

In the present chapter, the catalytic mechanism of Fdh has been simulated using DFT tools and correlated with experimental kinetic data from several Fdhs isolated from *Desulfovibrio* species. This procedure allowed us to address how the interaction enzyme-substrate is performed, the role of amino acid residues close to the active site, the conformational changes experienced by the metal site, and the relevance of the metal ion, Mo or W, in catalysis.

### IV.3 Experimental procedures

**IV.3.1 Bacterial strain, culture media, and growth conditions.** *D. desulfuricans*, *D. gigas*, and *D. alaskensis* cells were respectively grown in lactate-nitrate [8], lactate-sulfate [9], and in a modified medium C from Postgate [10]. Cells were grown under anaerobic conditions at 37°C and collected by centrifugation at the end of the exponential phase.

**IV.3.2 Enzymes purification.** Soluble extracts were obtained as described in Chapter III (section III.3.1) and dialyzed overnight against 10 mM Tris-HCl pH 7.60. All these steps were performed at 4 °C.

Molybdenum-containing Fdh from *D. desulfuricans* was purified as described by Rivas *et al* [4]. W-containing Fdh from *D. alaskensis* was purified as described in Chapter III (section III.3.3).

W-containing Fdh from *D. gigas* was purified with a method different to that reported before [11]. The soluble extract was loaded into a column with DE-52 resin (Whatman) equilibrated with 10 mM Tris-HCl. Elution was performed using a linear gradient from 10 to 500 mM Tris-HCl in 5 column volumes. The fractions containing Fdh were dialyzed and loaded into a Source 15Q column (GE Healthcare) equilibrated with 5 mM Tris-HCl and eluted using a linear gradient until 300 mM Tris-HCl in 10 column volumes. The fractions containing Fdh activity were pooled and loaded into a hydroxyapatite column equilibrated with 1 mM potassium phosphate buffer (KPB) and eluted using a linear gradient until 300 mM KPB in 10 column volumes. Finally, the fraction containing Fdh was concentrated by ultrafiltration in a centricon system (Amicon) and loaded into a Superdex 200 equilibrated with 300 mM Tris-HCl. All the purification steps were performed at 4°C and pH 7.60.

**IV.3.3 Enzyme Kinetic Assays.** Steady-state kinetic studies of all Fdh were performed as described in Chapter III (section III.3.2). Enzyme and substrate concentrations were in the range of 10 to 35 nM and 5 to 500 μM, respectively.

For the study of the primary isotopic effect, sodium formate was replaced by sodium formate labeled with deuterium in the alpha position (Cambridge Isotopes).

### IV.3.4 Theoretical calculations.

**IV.3.4A The configuration of the active site.** The model chosen to study the catalytic mechanism of Fdh includes a molybdenum (or tungsten) bis-dimethyl dithiolene complex, in which the ligands represent a portion of the pyranopterinic cofactor. The coordination sphere of the Mo (or W) center was completed with a sulfur atom, and a SeCH<sub>3</sub> group that was chosen to mimic the SeCys140 residue. The model was subsequently completed with the conserved His141, Arg333 and Val139 residues (amino acid numbering corresponding to Fdh-H from *E. coli*)[1,2,12-14]. For the calculations, the position of the atoms marked with an F letter in figure IV.3 were frozen in order to keep the optimized structures close to the X-ray structure.

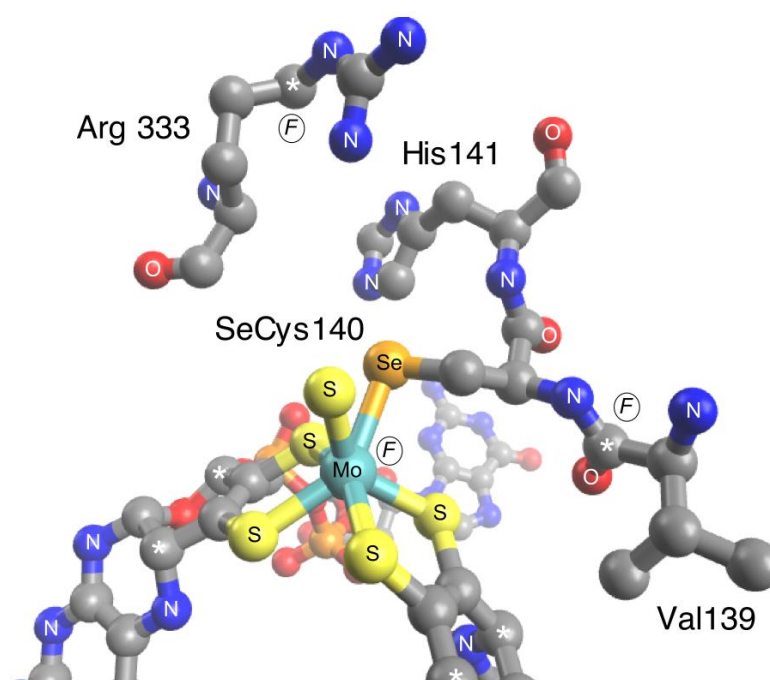


**Figure IV.3| Fdh model.** Model used to study the catalytic mechanism of formate dehydrogenase (frozen atoms are marked with the F letter and the truncation of the residues marked with a white asterisk).

**IV.3.4B Methods used.** The starting coordinates were taken from the 2.80 Å resolution X-ray structure of the oxidized form of Fdh from *E. coli* (PDB code: 1fdo) where the oxygen ligand to the Mo ion was replaced by a sulfur atom. All geometry optimizations were performed with Gaussian 03 [15], applying density functional theory methods and the 6-31G(d) basis set. Becke's three-parameter exchange functional was used together with the functional of Lee *et al* (B3LYP) as implemented in Gaussian [16-19]. In all geometry optimizations, we first searched for the transition state starting from a

structure similar to the reactants model. This was generally obtained with a scan where the reaction coordinate that we were interested in, was shortened or stretched. Once the transition state was located, the reactants and the products, associated with it, were determined through internal reaction coordinate (IRC) calculations. In all cases, the geometry optimizations and the stationary points were obtained with standard Gaussian convergence criteria. The transition state structures were all verified by vibrational frequency calculations, having exactly one imaginary frequency with the correct transition vector, even using frozen atoms, which shows that the frozen atoms are almost free from steric strain.

The final electronic energies were calculated using the all-electron 6-311++G(3df,2pd) basis set. Zero-point corrections, thermal, and entropic effects ( $T = 310.15$  K,  $P = 1$  bar) were added to all calculated energies, with the 6-31G(d) basis set [20]. To estimate solvation effects of the rest of the enzyme, single point calculations on the optimized geometries were performed with the conductor-like polarizable continuum model (CPCM), as implemented in Gaussian 03 [15], with the B3LYP/6-311++G(3df,2pd) level. This feature is of particular importance to the study of enzymatic catalysis because the use of a continuum model is normally taken as an approximation to the effect of the global enzyme environment in a reaction. A dielectric constant of  $\epsilon=4$  was chosen to describe the protein environment of the active site in accordance with previous suggestions [7,21-23]. The atomic spin-density distributions were calculated at the B3LYP level by employing a Mulliken population analysis, using the basis set 6-31G(d).

## IV.4 Results

### IV.4.1 Steady-state kinetic studies.

The Fdhs used in this studies needed to be reduced with substrate before the addition of electron acceptor in order to activate the enzyme and yield the maximal specific activity in the kinetic assay as we can see in figure IV.4.

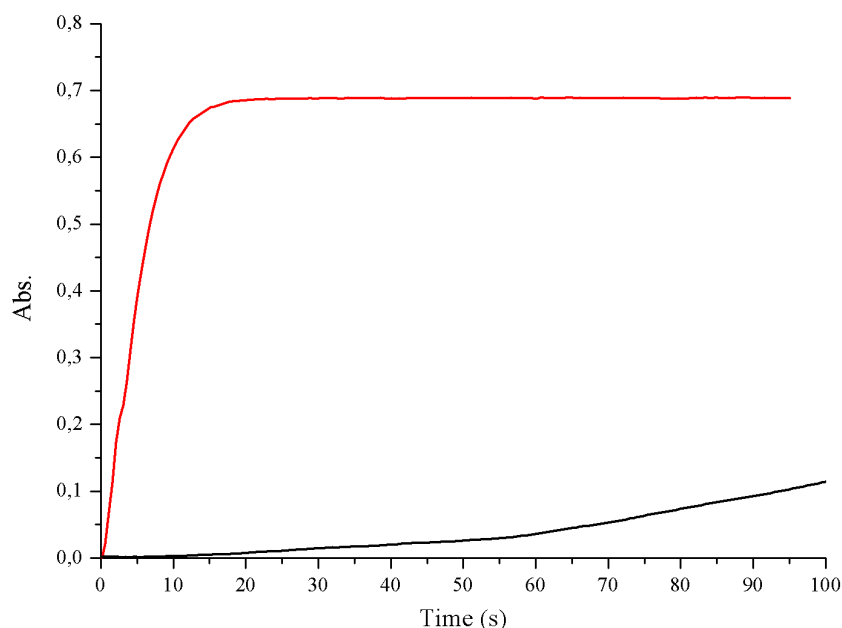


**Figure IV.4| Enzyme activation.** Kinetic timescan of the reduction of benzyl viologen monitored at 555 nm catalyzed by Mo-dependent Fdh from *D. desulfuricans*. **Red:** with activation, Fdh (35 nM) was incubated with 10 mM of sodium formate in 60 mM Tris-HCl buffer pH 8.0 and 133 mM  $\beta$ -mercaptoethanol at 37 °C. The reaction was started adding 7.5 mM benzyl viologen. **Black:** without activation, Fdh (35 nM) was incubated with 7.5 mM benzyl viologen in 60 mM Tris-HCl buffer pH 8.0 and 133 mM  $\beta$ -mercaptoethanol at 37 °C. The reaction was started adding 10 mM sodium formate. All assays were performed in Argon atmosphere in stoppered quartz cell.

The Michaelis-Menten behavior of Fdh with formate or deuteuroformate is showed in figure IV.5. The kinetic parameters of the three Fdh isolated from sulfate-reducing bacteria are given in table IV.1 together with those of Fdh-H isolated from *E. coli* K12. The  $K_M$  and  $k_{cat}$  values of both the Mo- and W-Fdh enzymes isolated from *Desulfovibrio* species are of the same order of magnitude, suggesting that the enzyme as a whole rather than the type of metal in the active site (Mo or W) is responsible for the turnover rate and specificity. This is in line with DFT calculations that confirmed that

changing Mo for W in the active site model does not significantly affect either the  $E_a$  or the  $E_r$  values of the rate-limiting step of the catalytic mechanism (not shown) and that will not be discussed further in this work.

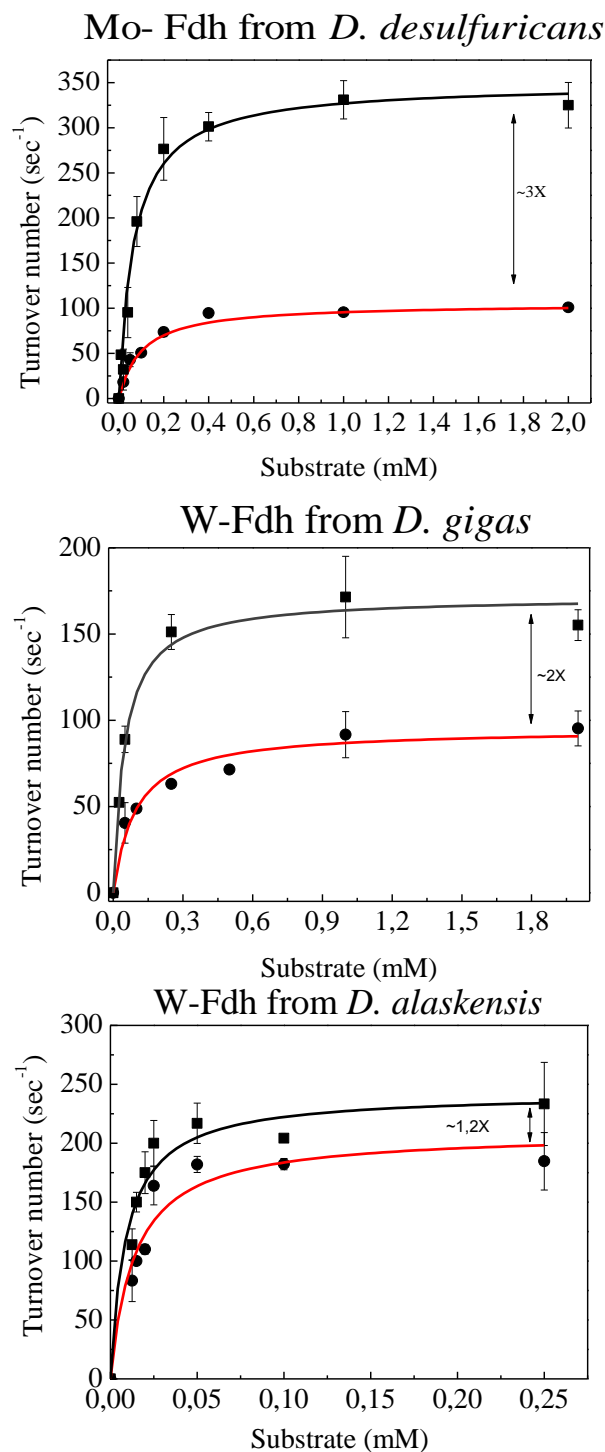


**Figure IV.5| Michaelis-Menten behavior from Fdh.** Michaelis-Menten plots of the steady-state kinetic assays performed in the three Fdh enzymes studied. Black and red lines are the fitting of the experimental values obtained with  $^1\text{HCOO-Na}$  (squares) and  $^2\text{HCOO-Na}$  (circles) as substrates.



As also shown in table IV.1, when formate with natural isotope composition was replaced by formate enriched with  $^2\text{H}$  at the alpha position, the  $k_{\text{cat}}$  values obtained with the enzymes studied here dropped  $\sim 2$ -3 times, without remarkably variations of the  $K_{\text{M}}$  values. This indicates that the transfer of the alpha-proton of the formate to the accepting group is involved in the rate-limiting step of the catalytic mechanism, in a clear contrast with the kinetic data of *Ec* Fdh-H (see kinetic parameters in table IV.1). The differences of our data with those obtained in *Ec* Fdh-H are due to the presence of the strong inhibitor azide in the Fdh-H preparations used by Axley *et al* [24], as we observed that azide addition to *Dd* Fdh results in similar  $k_{\text{Cat}}$  values using either  $^1\text{HCOO}^-$  or  $^2\text{HCOO}^-$  (not shown). This experimental conclusion derived from the kinetic studies will be analyzed below with DFT studies.

**Table IV.1| Kinetic parameters of Fdhs.** Kinetic parameters obtained through steady-state enzyme kinetic studies on several Mo and W containing Fdhs.

	$k_{\text{Cat}} (\text{s}^{-1})$		$K_{\text{M}} (\mu\text{M})$		$k_{\text{Cat}}/K_{\text{M}}$		Reference
	$\text{HCOO}^-$	$\text{DCOO}^-$	$\text{HCOO}^-$	$\text{DCOO}^-$	$\text{HCOO}^-$	$\text{DCOO}^-$	
Mo-Fdh <i>D.desulfuricans</i>	347	104	64	81	5.4	1.3	This Work
W-Fdh <i>D.gigas</i>	174	96	51	66	3.4	1.5	This Work
W-Fdh <i>D.alaskensis</i>	241	191	10	9	24.1	21.2	This Work
Mo-Fdh H <i>E.coli</i> K12	1367	1133	13300	49500	0.1	0.02	[24]

## IV.4.2 DFT calculations.

### IV.4.2.1 Structure and oxidation state of the active site.

In metal coordination environments rich in sulfur ligands such as the one studied here for the Mo ion, it is difficult to determine the formal oxidation state of the atoms comprising the model. For this reason, it was assumed that each dimethyl dithiolate ligand ( $[\text{H}_6\text{C}_4\text{S}_2]^{2-}$ ) has a net charge of -2, the Se-CH<sub>3</sub> of -1, and that the inorganic sulfur ( $\text{S}_i$ ) of -2.

Since molybdenum (or tungsten) can be found in these types of enzymes in three different oxidation states ( $\text{Mo}^{4+}$ ,  $\text{Mo}^{5+}$  or  $\text{Mo}^{6+}$ ), our first task was to determine the formal oxidation state of the metal ion in the X-ray structures of the oxidized and reduced forms of Fdh. For this purpose, the hexacoordinated model of the active site

described in materials and methods section was optimized assuming IV (charge = -3, multiplicity =1), V (charge = -2, multiplicity =2) and VI (charge = -1, multiplicity =1) formal oxidation states of the Mo. The resulting structures obtained after optimization are depicted in figure IV.6.

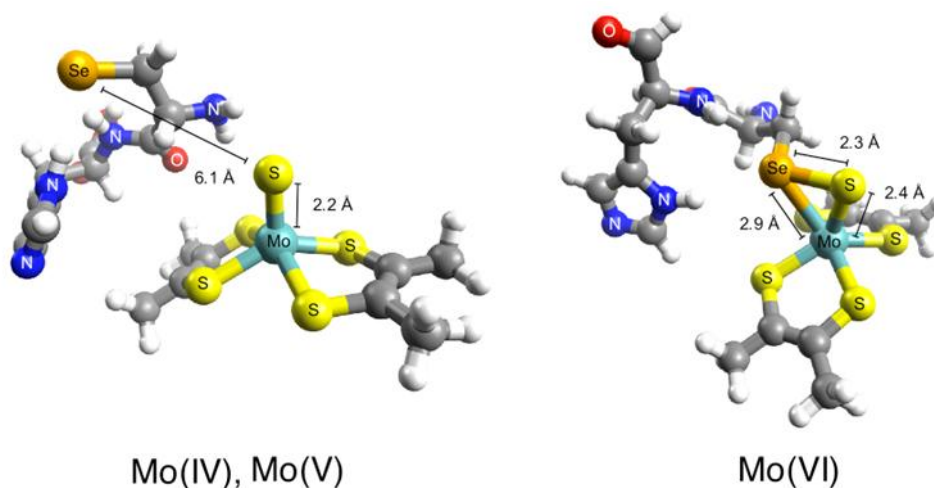


**Figure IV.6| Fdh active site structures.** Optimized structure of the active site of the models of Fdh assuming  $\text{Mo}^{4+}$ ,  $\text{Mo}^{5+}$  and  $\text{Mo}^{6+}$  formal oxidation states.

The calculations revealed that the structures optimized assuming  $\text{Mo}^{4+}$  and  $\text{Mo}^{5+}$  ions are very similar (figure IV.6). In both cases, the Se atom is found *c.a.* 6.1 Å apart from the  $\text{S}_i$ , which remains bound to the Mo ion with a bond length of *c.a.* 2.2 Å. These observations are in agreement with the X-ray structure of the formate-reduced Fdh-H (PDB code: 2iv2), where the SeCys residue is not coordinating the Mo ion, being at 11 Å from the Mo ion and stabilized with a neighboring arginine by H-bonds[2]. Only when the formal oxidation state  $\text{Mo}^{6+}$  is assumed, the Se atom remains bound to the Mo ion and to the  $\text{S}_i$  ligand at *c.a.* 2.9 Å and 2.3 Å, respectively (figure IV.6).

The different conformational arrangements of the SeCys residue observed in the three models can be explained taking into account the charge distribution. The total negative charge of the system is higher in the  $\text{Mo}^{4+}$  and  $\text{Mo}^{5+}$  models. A Mulliken population analysis reveals that the charge is mainly located at the Se atom (-0.71 a.u. for  $\text{Mo}^{4+}$  and -0.67 a.u. for  $\text{Mo}^{5+}$ ), the  $\text{S}_i$  (-0.68 a.u. for  $\text{Mo}^{4+}$  and -0.47 a.u. for  $\text{Mo}^{5+}$ ) and at the dimethyl dithiolenes (-0.9 a.u. for  $\text{Mo}^{4+}$  and -0.4 a.u. for  $\text{Mo}^{5+}$ ). This charge distribution creates a repulsive environment between Se and  $\text{S}_i$  ligands that produces the dissociation of the SeCys residue. In fact, DFT calculations performed to evaluate the

formation of the enzyme-substrate (ES) complex with the  $\text{Mo}^{4+}$  and  $\text{Mo}^{5+}$  models yielded activation energies of *c.a.* 50 kcal/mol, which rules out that the catalysis starts with the enzyme in the  $\text{Mo}^{4+}$  and  $\text{Mo}^{5+}$  forms.

The Mulliken population analysis in the  $\text{Mo}^{6+}$  model reveals that the negative charge is distributed in the dimethyl dithiolene ligands (-0.4 a.u.) and at the Mo ion (-0.4 a.u.). In contrast with the other two models, the  $\text{S}_i$  ligand is neutral (0.05 a.u.) which, as will be seen below, favors the interaction substrate with the active site.

The charge distribution in the three models determines the type of interaction that the  $\text{S}_i$  ligand has with the molybdenum atom. The smaller bond length (2.2 Å) observed in the  $\text{Mo}^{4+}$  and  $\text{Mo}^{5+}$  models suggests that  $\text{S}_i$  ligand might be double bonded to the Mo, while in the  $\text{Mo}^{6+}$  model the distance (2.4 Å) suggest that  $\text{S}_i$  ligand is single bonded to the Mo ion and to the SeCys residue (figure IV.6).

#### IV.4.2.2 *Formation of enzyme-substrate complex: selenium-sulfur shift.*

Taking into account the results described above, it can be assumed that the formal oxidation state  $\text{Mo}^{6+}$  represents the oxidized X-ray structure (figures IV.5 and IV.6). However, in the course of this study it was found that formate binds the active site only if the Se- $\text{S}_i$  bond is previously broken. This is achieved increasing the Se- $\text{S}_i$  distance from 2.25 Å to 3.56 Å, which requires 15.5 kcal/mol and is endothermic in 7.5 kcal/mol (figure IV.7). The transition state for this reaction is characterized by one imaginary frequency at  $75.72i \text{ cm}^{-1}$ . After this rearrangement, both atoms remain bound to the Mo ion but with different bond lengths (Se-Mo: from 2.39 Å to 2.59 Å,  $\text{S}_i$ -Mo: from 2.91 Å to 2.16 Å). At this stage, the partial interaction of the formate anion produces a redistribution of the charge in the metal complex. This is observed because the charges at the  $\text{S}_i$  and the Mo-bis(dimethyl dithiolene) change from -0.26 a.u. to -0.60 a.u. and -0.62 a.u. to -0.08 a.u., respectively.

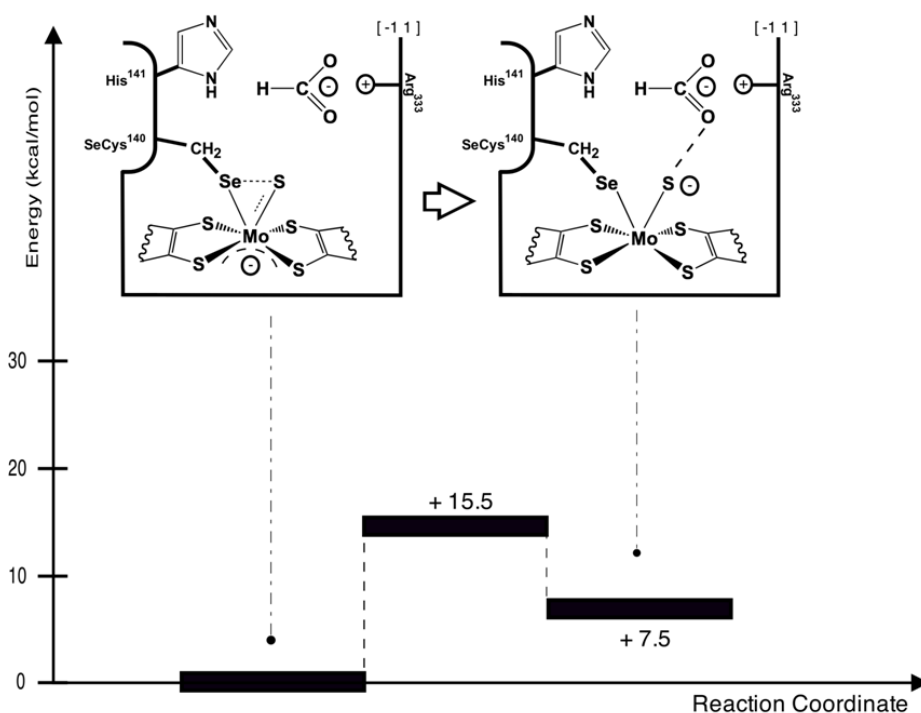


**Figure IV.7| Enzyme activation.** General overview of the energies involved in the activation of the enzyme (the total charge and multiplicity of the system are between brackets).

Experimental evidence from EPR spectroscopy and X-ray crystallography suggests that the formate molecule reacts with the Mo ion [1,2,4,5]. The  $\text{Mo}^{6+}$  model obtained in this study has however revealed that the Se- $\text{S}_i$ -Mo complex does not show an available binding site for the formate to bind the Mo, indicating that the formation of the ES complex is not a straightforward process. Our studies showed that when the oxygen of the formate molecule moves toward the  $\text{S}_i$  ligand (-0.53 a.u.), it pushes the  $\text{S}_i$  ligand to the position originally occupied by the Se atom, forcing the dissociation of the SeCys residue from the Mo ion (Mo-Se: from 2.72 to 4.11 Å). In this process, Arg333 has a key role driving the formate molecule next to the  $\text{S}_i$  ligand through two strong hydrogen bonds (1.74 Å). Because of the repulsive environment generated by the approximation of the formate anion to the negatively charged metallic complex, this reaction requires 20.0 kcal/mol (figure IV.8). However, this high energetic barrier is compensated as the reaction is exothermic (-5.7 kcal/mol) and ends with the formate molecule bound to the Mo ion by a single bond (2.14 Å). The  $\text{S}_i$  also remains single-bonded to the Mo at 2.50 Å and loses its negative charge (-0.06 a.u.). At this stage, the SeCys residue dissociates from the Mo, but remains covalently bound to the  $\text{S}_i$  (2.26 Å).

The transition state of this reaction (characterized by one imaginary frequency at  $119.62i \text{ cm}^{-1}$ ) clearly demonstrates the feasibility of three events in one step: i) dissociation of the SeCys residue from the Mo ion (selenium-shift), ii) conformational rearrangement of S<sub>i</sub> (sulfur-shift) and, iii) coordination of the formate molecule to the Mo ion.

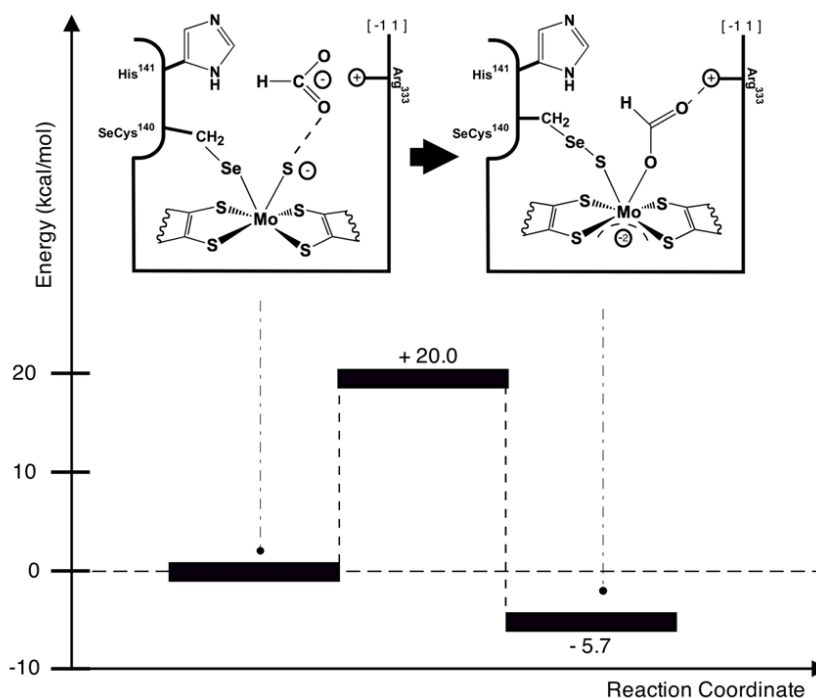


**Figure IV.8| Formation of the ES complex.** General overview of the energies involved in the formation of the ES complex (the total charge and multiplicity of the system is between brackets).

This reaction is only possible due to the presence of the Mo-dithiolene complex and the conserved Arg333 that act buffering the negative charge of the formate anion (Mo-dithiolenes charge change from  $-0.13$  to  $-0.72$  a.u.). This type of the behavior was also proposed in the catalytic mechanism of the periplasmic nitrate reductase, where the nitrate anion binds a similar negatively charged active site [25]. These results suggest that one of the roles of the pyranopterin cofactors in these enzymes might be, in addition to provide an electron transfer pathway [26,27], to cushion the electrostatic repulsion produced by the negative charge of formate, which in turns lower the activation energy barrier for the formation of the ES complex.

#### IV.4.2.3 Formation of selenide anion and formate oxidation.

The oxidation of the formate molecule into carbon dioxide involves the transfer of either a proton or a hydride from the formate to a neighboring residue/atom. Two atoms could accomplish this function: the Se atom from the SeCys residue or the inorganic sulfur atom  $S_i$ . Our results revealed that this step is only possible with the participation of SeCys residue. Moreover, it was observed that His141 is also very important for this reaction, since the exclusion of His141 yielded an activation energy value *c.a.* 45 kcal/mol.

Computational results including His141 in the model indicated that formate oxidation occurs via the formation of a selenide anion, which implies that the Se- $S_i$  bond must be broken in a reaction that is not energetically favorable owing the instability of the product. In this sense, the reaction of SeCys residue dissociation requires an  $E_a = 18.4$  kcal/mol and is endothermic in 16.7 kcal/mol (figure IV.9). In the reactants, the Se atom is covalently bound to  $S_i$  (2.65 Å), which is also bound to the Mo ion (2.24 Å). As the Se- $S_i$  bond length is stretched, the Se atom forms a H-bond with one NH group of the imidazole ring of the conserved His141 which lower  $E_a$ . In the optimized structure of the transition state (40i  $\text{cm}^{-1}$ ), Se atom is almost dissociated from  $S_i$  (3.20 Å), and at the same time His141 undergoes a conformational rearrangement in which the NH group is aligned with the Se atom to form the H-bond. In the product of the reaction, the Se- $S_i$  bond is broken (4.44 Å), and the Se anion (with a charge of -0.83 a.u.) is formed. It is worthy to mention that in this stage of the reaction the NH from the histidine imidazole is at 2.56 Å from the Se atom, indicating the important role of the conserved His141 in stabilizing the Se anion that will perform the proton abstraction. It was also tested the hypothesis of the proton transfer between the formate molecule and the Se atom in one concerted step, i.e. with the Se atom binding the  $S_i$  ligand. However,  $E_a$  values of *c.a.* 45 kcal/mol were obtained.

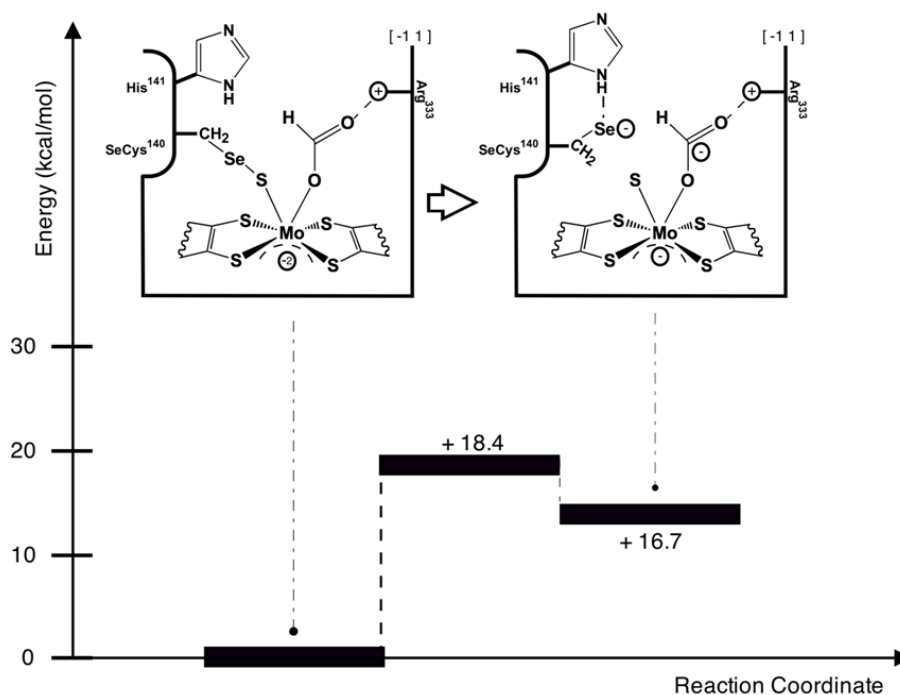


**Figure IV.9| SeCys dissociation.** General overview of the energies involved in the dissociation of the SeCys (the total charge and multiplicity of the system is between brackets).

The next step, which comprises the formate oxidation *per se*, starts with the Se anion positioned at 3.84 Å from the  $H_{\text{formate}}$  (figure IV.10). During the search of the transition state for this reaction, it became clear that when the  $\text{Se-H}_{\text{formate}}$  distance gets reduced, the  $\text{S}_i\text{-C}_{\text{formate}}$  also decreases. This is evident in the transition state of this reaction ( $589.48i\text{ cm}^{-1}$ ) in which the Se atom is found at 1.89 Å from the  $H_{\text{formate}}$ , and the  $\text{S}_i$  at 2.15 Å from the  $\text{C}_{\text{formate}}$  (3.30 Å in the reactants).

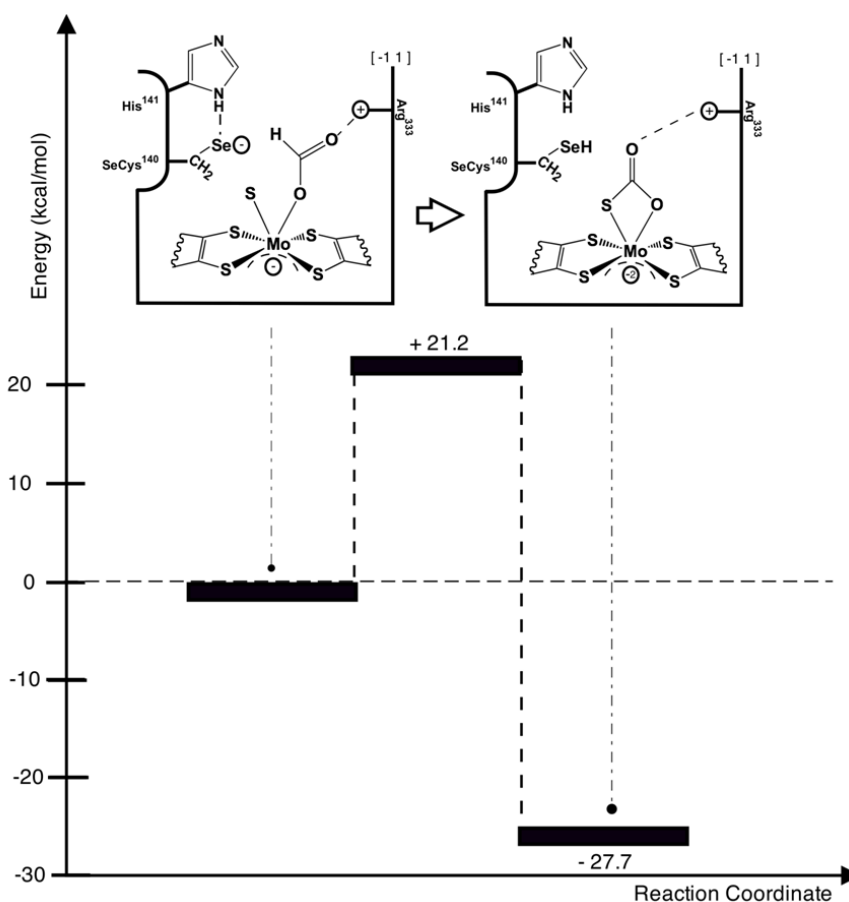


**Figure IV.10| Proton transfer.** General overview of the energies involved in the Proton transfer (the total charge and multiplicity of the system are between brackets).

The optimized structure of the transition state also revealed that it is a proton with charge +0.81 a.u. and not a hydride what is transferred to the SeCys residue, which is in agreement with the results reported by Leopoldini *et al.*[7] It is possible that  $S_i$  has some responsibility in the proton transfer between the formate and SeCys residue since the  $S_i$ - $H_{\text{formate}}$  distance found in the transition state of the reaction of figure IV.10 is as low as 2.35 Å.

In the product of the reaction depicted in figure IV.10, the SeCys residue is protonated and moves away from the active site (Mo-Se distance 7.66 Å). Consequently, the H-bond between the Se and His141 residues is broken and a new H-bond between the  $S_i$  and His141 is formed (2.53 Å). The carbon from the  $-\text{CO}_2$  group is now bound to  $S_i$  at a distance of 1.78 Å, and one of the oxygen from the  $-\text{CO}_2$  remains bound to the Mo ion (figure IV.11).



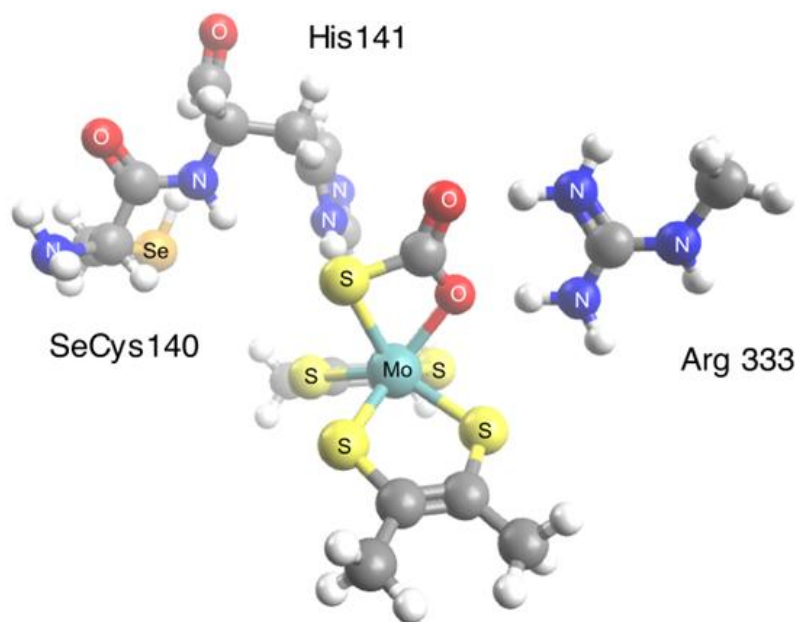


**Figure IV.11| Active site after proton transfer.** Product obtained after finishing the proton transfer from the formate to the SeCys140.

The proton transfer reaction requires 21.2 kcal/mol and is exothermic in -27.7 kcal/mol (figure IV.10), indicating that despite the relatively high activation energy barrier of the two steps, this reaction is feasible. It is important to mention that a high  $E_a$  value was expected for this step owing the primary isotopic effect observed with deuterium-labeled sodium formate in the enzyme kinetic studies mentioned before (table IV.1).

#### IV.4.2.4 Carbon dioxide release.

The next step of the catalytic cycle involves the release of carbon dioxide and the two-electron oxidation of the active site. This can be accomplished through two different ways: i) The carbon dioxide is released before the oxidation of the active site or, ii) the active site is oxidized to promote the product release.

In the first case, the dissociation of the  $\text{CO}_2$  requires the two steps depicted in figure IV.12. Firstly, the Mo-O bond is broken (Mo-O distance changes from 2.21 Å to 3.81 Å) producing the intermediate stage where the  $\text{CO}_2$  still remains attached to the active site through the  $\text{S}_i\text{-C}$  bond. After the break of the Mo-O bond, the Mo- $\text{S}_i$  bond length decreases from 2.54 to 2.34 Å. The charge distribution is conserved during the reaction being mainly localized at the dimethyldithiolene ligands (-1.33 a.u.) and around the  $\text{-CO}_2$  group (-0.75 a.u.). This reaction needs an  $E_a = 13.3$  kcal/mol, is endothermic ( $E_r =$

7.2 kcal/mol) and yielded a transition state characterized by one imaginary frequency at  $67i\text{ cm}^{-1}$ .

To complete the product release, the  $S_i$ -C bond must be broken. This happens when the  $S_i$ -C<sub>formate</sub> distance increases from 1.89 Å in the reactants to 2.20 Å in the transition state ( $123i\text{ cm}^{-1}$ ). In the product, the  $\text{CO}_2$  molecule can be found at 3.81 Å ( $S_i$ -C distance) as a neutral molecule (charge -0.05 a.u.). This reaction yielded an  $E_a = 4.5\text{ kcal/mol}$  and  $E_r = -7.8\text{ kcal/mol}$ , indicating the two-step process of  $\text{CO}_2$  release is almost thermoneutral ( $-0.6\text{ kcal/mol}$ ).

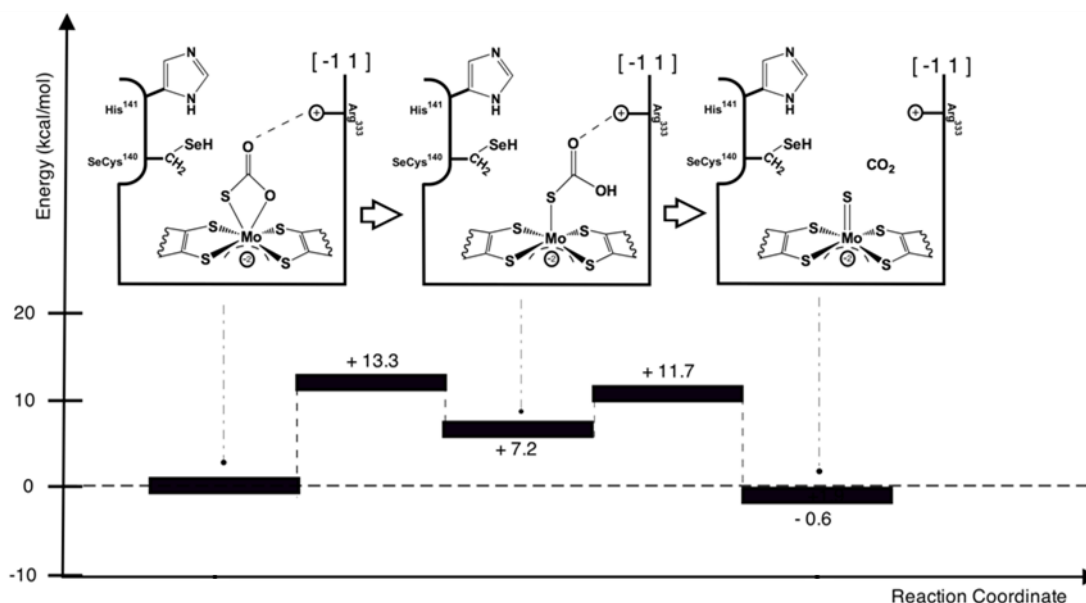


**Figure IV.12| Carbon dioxide release.** The mechanism of the carbon dioxide release prior (top) and after (bottom) the electron transfer (the total charge and multiplicity of the system is enclosed in brackets).

In the second case (not shown), it was assumed that after the transfer of the proton of the formate to SeCys residue, two electrons would be immediately transferred to the redox centers included in the electron transfer pathway of the protein [26,27]. This implies the two-electron oxidation of the active site for what was necessary to manually adjust the charge of the model to +1. Comparing with the model previous to these modifications, the only changes are the  $\text{Mo-S}_i$  and  $\text{Mo-O}_{\text{formate}}$  bond lengths, both decreasing from 2.54 to 2.39 Å and 2.21 to 2.15 Å, respectively. The negative charge remains located in the  $-\text{CO}_2$  group while the dithiolene ligands becomes positively charged.

In the transition state (imaginary frequency at  $127.91i\text{ cm}^{-1}$ ) it can be noted that both the Mo-O and the  $S_i$ -C bonds are simultaneously broken at the same time that the Mo- $S_i$  bond length is stretched to 2.12 Å. In the products of this reaction the dissociation of the  $\text{CO}_2$  molecule is accomplished and similarly to what happens in the first hypothesis, the  $S_i$  becomes double bonded to the Mo. This reaction requires an activation energy of 25.6 kcal/mol and is exothermic in -16.6 kcal/mol.

Analyzing the activation energy profiles for the two hypotheses tested for  $\text{CO}_2$  release, the first hypothesis emerges as more probable, even though it needs two steps to release the product.

#### IV.4.2.5 *Regeneration of the active site to the initial state*

On the basis of the complex obtained after  $\text{CO}_2$  release, the last steps of the proposed catalytic mechanism would involve the transfer of the proton attached to the SeCys residue, oxidation of the active site from Mo(IV) to Mo(VI), and binding of the SeCys residue to the Mo ion. The proton transfer process could be assisted with solvent molecules or with some neighboring amino acid residues. However, because there is no experimental data about how this is accomplished, the only thing that we were able to model was the binding of the resulting anionic SeCys residue to the Mo(VI) ion in the oxidized active site. In this sense, it is expected that the loop in which the SeCys residue is located undergoes a conformational rearrangement.

To model this reaction, the proton of the SeCys residue was manually deleted and the charge of the system was adjusted to obtain a Mo ion in the +6 formal oxidation state to emulate the reoxidation of the active site. As expected, the overall charge of the active site became more positive. The charge of  $S_i$  ligand changed from -0.63 to 0.19 a.u. without Mo- $S_i$  bond length modification (from 2.15 to 2.14 Å). The anionic Se atom with a charge of -0.71 a.u. is 3.52 Å apart from the  $S_i$  ligand and interacts very closely with His141 (2.64 Å) through a H-bond with the imidazole NH group. From this point, two pathways that will depend on the presence or absence of a substrate molecule near the active site can be drawn. For the first pathway, the active site structure in the absence of formate returns to the initial state, in which both Se atom and  $S_i$  ligand are bound to the Mo(VI) ion. The computational results indicate that this process requires two steps and is energetically feasible (figure IV.13). The first step implies the binding of the Se atom to the  $S_i$  ligand. This process yielded an  $E_a = 2$  kcal/mol and is

exothermic in -18 kcal/mol. The optimized geometry of the transition state (imaginary frequency at  $33i\text{ cm}^{-1}$ ) reveals that the Se atom is  $2.25\text{ \AA}$  from the  $S_i$  ligand and  $3.35\text{ \AA}$  from the Mo ion. In the product of this reaction, the Mo- $S_i$  bond-length increases from  $2.14$  to  $2.35\text{ \AA}$ , indicating that the Mo- $S_i$  double bond become single upon Se atom binding. In spite of this rearrangement, the Se atom does not bind the Mo ion remaining  $3.94\text{ \AA}$  apart. The charge distribution remains almost unaltered ( $-0.67$  a.u. in each dithiolene ligand,  $-0.34$  a.u. in the  $S_i$ , and  $-0.24$  a.u. in the Se). After Se- $S_i$  bond formation, the SeCys residue binds the Mo(VI) ion and the  $S_i$  as in the initial state. The calculations yielded an  $E_a = 3.2\text{ kcal/mol}$  and  $E_r = 1.2\text{ kcal/mol}$ . The optimized geometry of the transition state (imaginary frequency at  $37.68i\text{ cm}^{-1}$ ) shows that the Se atom approaches to the Mo ion (from  $3.94$  to  $3.35\text{ \AA}$ ) and that the charge distribution and the Mo- $S_i$  and Se- $S_i$  bond-lengths remain unaltered. In the product, the SeCys residue binds the Mo ion and the  $S_i$  ligand through single bonds ( $2.96$  and  $2.26\text{ \AA}$ , respectively).

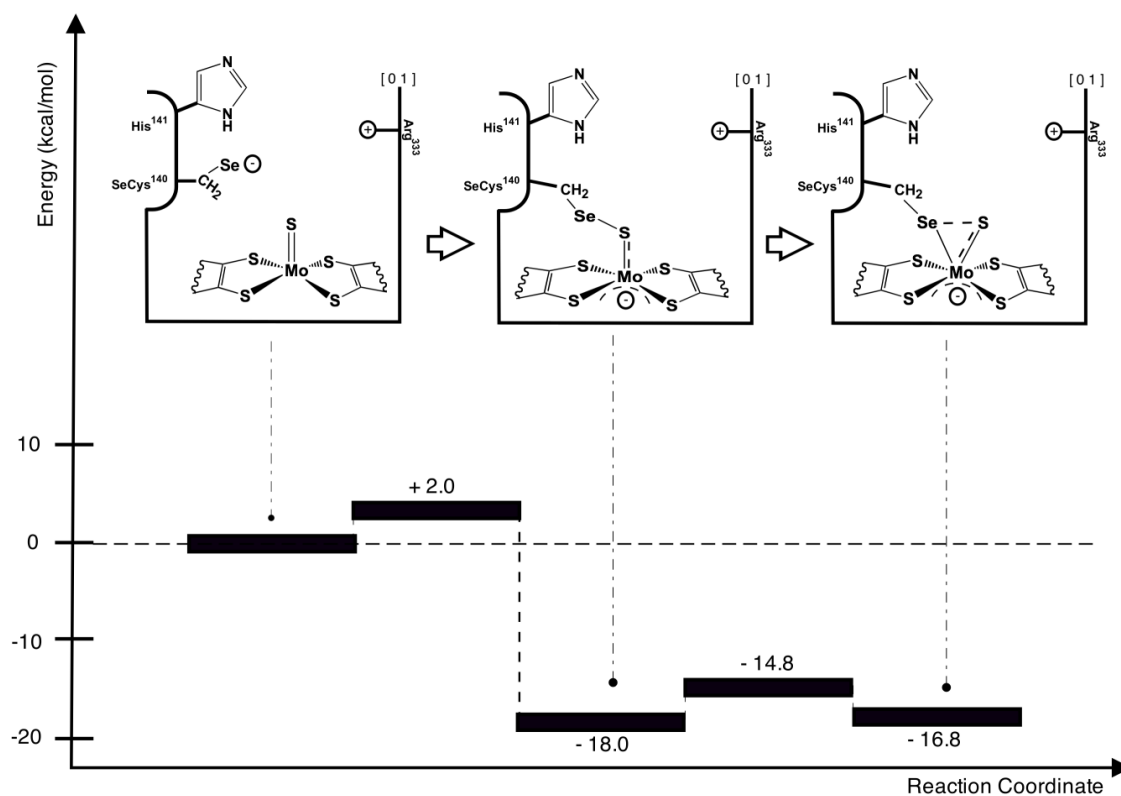


**Figure IV.13| Active site regeneration.** Regeneration of the active site to the initial oxidized state (the total charge and multiplicity of the system are between brackets).

The second pathway is summarized in figure IV.14. The computational results showed that binding a new formate molecule to the oxidized active site (as found in the starting

species of figure IV.13) is a one-step process requiring only  $E_a = 6.1$  kcal/mol and  $E_r = 2.7$  kcal/mol (figure IV.14). In the transition state (imaginary frequency at  $45i$   $\text{cm}^{-1}$ ) the Mo-S<sub>i</sub> bond-length is unaltered but the S<sub>i</sub> ligand is pushed aside opening space for the incoming formate molecule (Mo-O<sub>formate</sub> bond-length 3.03 Å). In the product of the reaction the formate binds the Mo ion (Mo-O<sub>formate</sub> bond-length 2.21 Å) and the S<sub>i</sub> ligand gains negative charge (-0.62 a.u.). Similar to what was observed before, the conserved Arg333 has a key role in this reaction driving and stabilizing the formate anion by H-bonds. However, there is a striking difference when the formate anion binds the active site with the SeCys residue bound or not to the S<sub>i</sub> ligand. The energy cost of binding a new substrate molecule is 14 kcal/mol less, which is due to the different charge distribution and steric hindrance of the complex when SeCys residue binds the S<sub>i</sub> ligand. This result indicates that the catalytic cycle may follow this pathway instead of regenerating the active site as in the initial state.

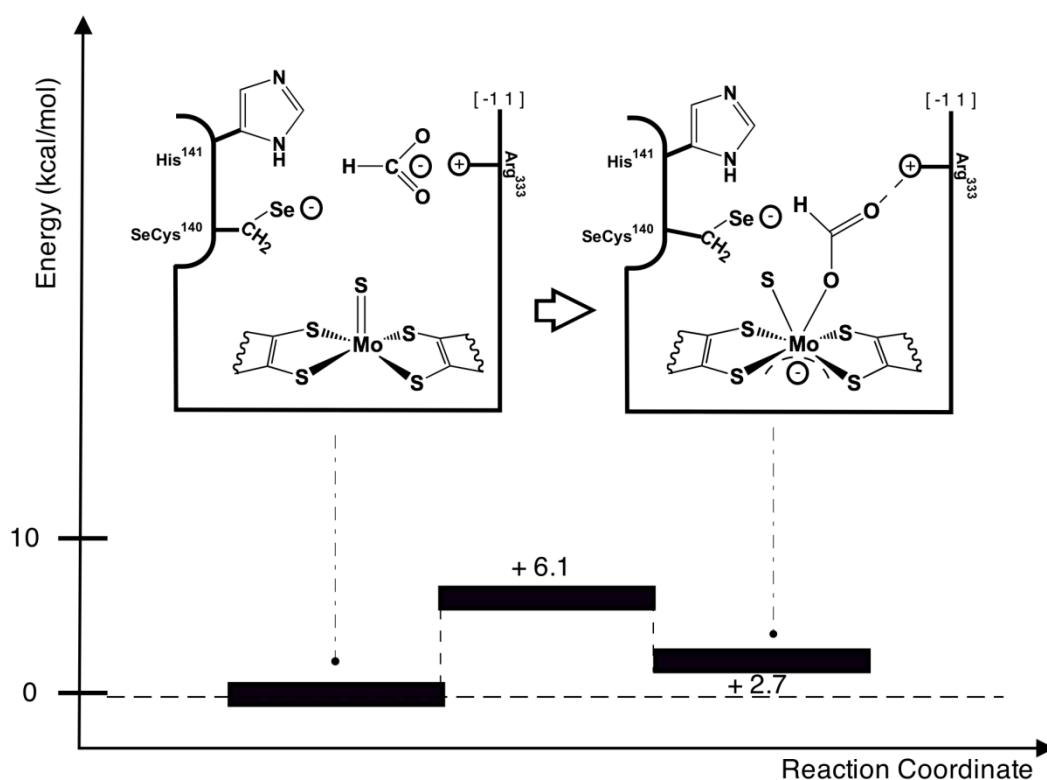


**Figure IV.14| Turnover in presence of formate.** Formate binding to an intermediate species produced after oxidation of the active site (the total charge and multiplicity of the system are between brackets).

## IV.5 Discussion

Figure IV.15 summarizes the main conclusions on the general catalytic mechanism of metal-dependent Fdh evaluated through DFT tools. The first part of this study demonstrated that the hexacoordinated Mo ion of the crystallographic structure is in the +6 oxidation state (figure IV.5, figure IV.15A). Previous studies in Fdh from *D. desulfuricans* demonstrated that this state represents an inactive form of the enzyme resulting from the aerobic purification procedure of an enzyme that works physiologically under strict anaerobic conditions [4]. This is corroborated with all the Fdh studied in this work, as they needed to be incubated with the substrate prior to the addition of the electron acceptor in order to obtain the maximal specific activity in the kinetic assay (figure IV.4). This activation step implies that the enzyme performs at least one complete turnover resting in a Mo(VI) state (figure IV.15H) different to the initial one (figure IV.15A). The reaction proceeds with the formate molecule binding the active site in a state where the Mo(VI) ion has an available binding position. This is indicated by the results summarized in figure IV.14, where the binding of the formate to the pentacoordinated Mo(VI) ion has an  $E_a = 6.1$  kcal/mol (figure IV.15, step H-D). In summary, the three initial steps with high activation energy values of 15.0 kcal/mol, 20.0 kcal/mol and 18.4 kcal/mol would represent the activation route necessary to perform the first cycle of the catalytic mechanism starting from the aerobically inactive enzyme (figure IV.15, steps A-B, B-C and C-D). The step B-C of figure IV.15, which involves the process identified as sulfur-shift, is very similar to that proposed for the catalytic mechanism of periplasmic nitrate reductase where the role of the SeCys residue is carried out by a Cys residue [25,28]. This may indicate that the sulfur-shift could be a common mechanism by which these enzymes enable a free coordinating position on the metal ion for substrate coordination.

The formate oxidation process also involves the participation of amino acids that are conserved in all metal-dependent Fdh characterized so far. Our DFT calculations indicate that the side chain of the arginine residue interacts with both substrate and product of the reaction guiding the substrate to the active site, stabilizing it, and driving the product release. In this sense, the positively charged side chain of arginine cancels the negative charge of the formate anion, facilitating its interaction with the active site.

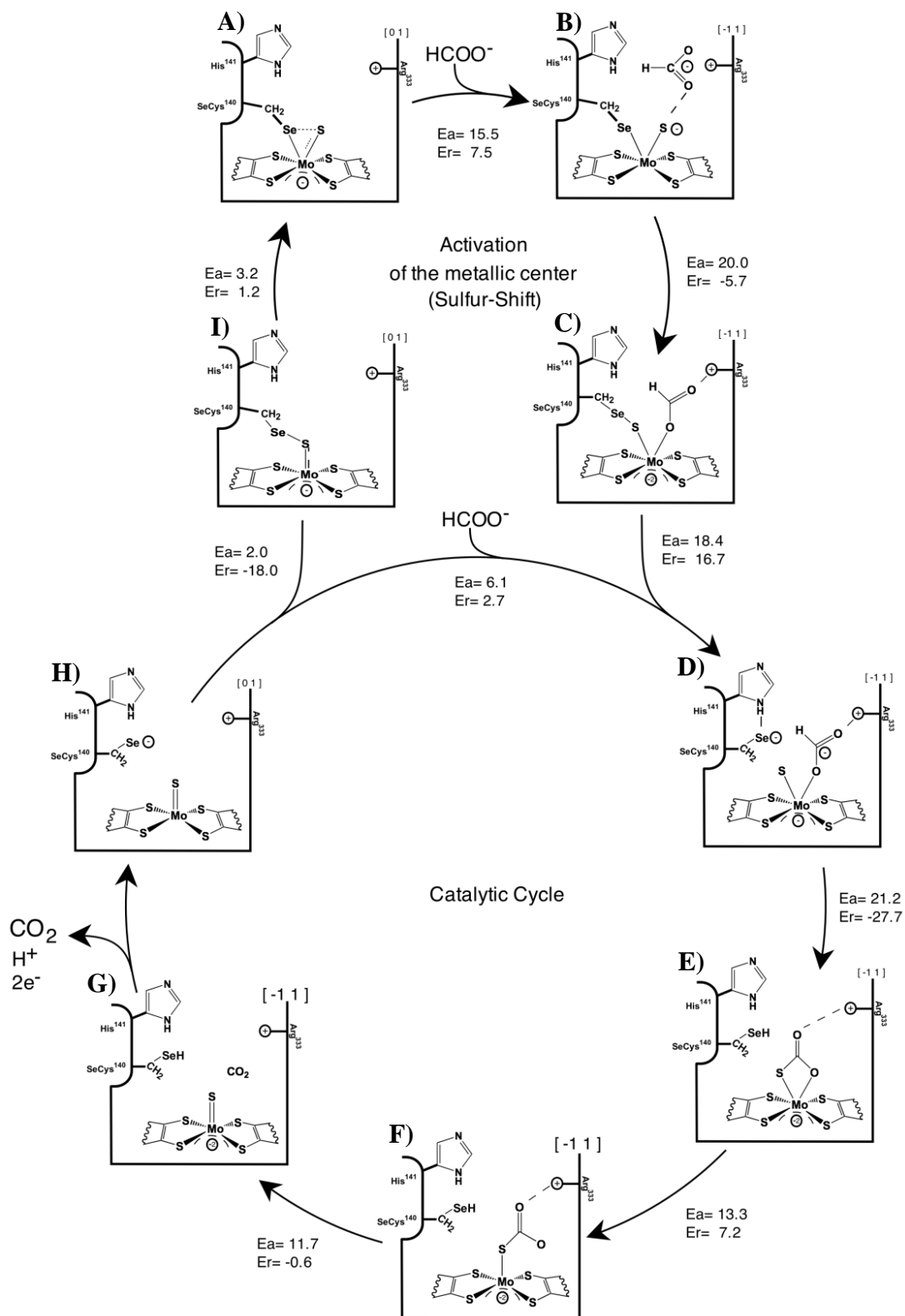


Figure IV.15| Global scheme of formate oxidation by Fdh. Global view of the catalytic mechanism of formate dehydrogenase.

One of the most intriguing roles to unveil was that of the conserved histidine residue. In a previous report, Khangulov *et al* proposed that this amino acid might be involved in the deprotonation of the SeCys following the proton transfer reaction from the substrate to the Se anion [5]. In contrast, our calculations indicate that a NH group of the imidazole ring of His stabilizes the Se anion through H-bonds (figure IV.9). This role is also supported by the fact that, when the conserved His is not included in the model, the formation of the Se anion yield an unstable transition state which results in a very high activation energy ( $E_a \sim 45$  kcal/mol). These results also suggest why metal-dependent Fdh contain a SeCys residue instead of a regular Cys residue, as found in periplasmic nitrate reductases. The SeCys and Cys side chains show pKa of 5.2 and 8.2, respectively. This indicates that under physiological conditions (pH  $\sim 7.00$ ) the Se atom of the SeCys residue can be found in the anionic form after breaking the bond with the S<sub>i</sub> ligand bound to the Mo ion. Owing to the high pKa of the sidechain of a Cys residue, the presence of a stable cysteinate at physiological pH is unlikely. This statement receives strong experimental support from early studies performed in *Ec* Fdh-H, in which was demonstrated that mutating the SeCys to a Cys almost inactivate the enzyme, lowering the  $k_{cat}$  more than two orders of magnitude (from  $2800\text{ s}^{-1}$  to  $9\text{ s}^{-1}$ ) [6].

The kinetic studies of the enzyme with the isotopically enriched  $^2\text{HCOONa}$  clearly indicate that the C-H bond break is involved in the rate-limiting step of the catalytic mechanism. Analyzing the activation energy values for every step of the simulated mechanism, and having in mind that the three initial steps of the mechanism (figure IV.15, A-B, B-C and C-D) do not take part in the enzymatic catalytic cycle, it can be noted that the highest activation energy barrier involves the transfer of the proton from the substrate to the selenium (21.2 kcal/mol, figure IV.15, step D-E) suggesting that, in agreement with the experimental results, this is the rate-limiting event of the catalytic mechanism.

Comparing metal-dependent Fdhs versus eukaryotic  $\text{NAD}^+$ -dependent Fdhs, it is evident a key difference in the enzymatic mechanism of formate oxidation to carbon dioxide. Metal-dependent Fdh catalyze the transfer of a proton from the substrate to the enzyme while, according to the currently accepted mechanism,  $\text{NAD}^+$ -dependent Fdh catalyze the transfer of a hydride to the  $\text{NAD}^+$  cofactor in order to produce a NADH [29]. Our results indicate that this fundamental difference results from the nature of the



group that accepts the H-ion from the substrate, i.e. a nucleophilic Se anion versus a  $\text{NAD}^+$  cation.

Some steps of the catalytic mechanism yield relatively high activation energy values. It is remarkable that all the reactions with high  $E_a$  involve the interaction between two atoms generating important electrostatic repulsion. This  $E_a$  values could be considerably lowered by including in the model some amino acids residues that provide hydrogen bonds to the  $S_i$  ligand bound to the Mo ion. Namely, the NH from the backbone amide binding the highly conserved Gly334 and Gln335 forms a H-bond with the  $S_i$  ligand. This interaction can be observed in the crystallographic structures of *Ec* Fdh-H, *Ec* Fdh-N and also in the W-containing *Dg* Fdh, where Gln335 of *Ec* Fdh-H is replaced by His and Glu in *Ec* Fdh-N and *Dg* Fdh, respectively [1,13,14] (figure IV.16). Moreover, this interaction is also present in the reduced form of Fdh-H, suggesting that this specific H-bond might have an important role in the enzymatic mechanism [2]. This interaction was not included in the model used here. However, with the use of QM/MM methods it will be possible to study the function of such type of interactions to lower the activation energies, and possibly the mechanism of deprotonation of the SeCys residue.

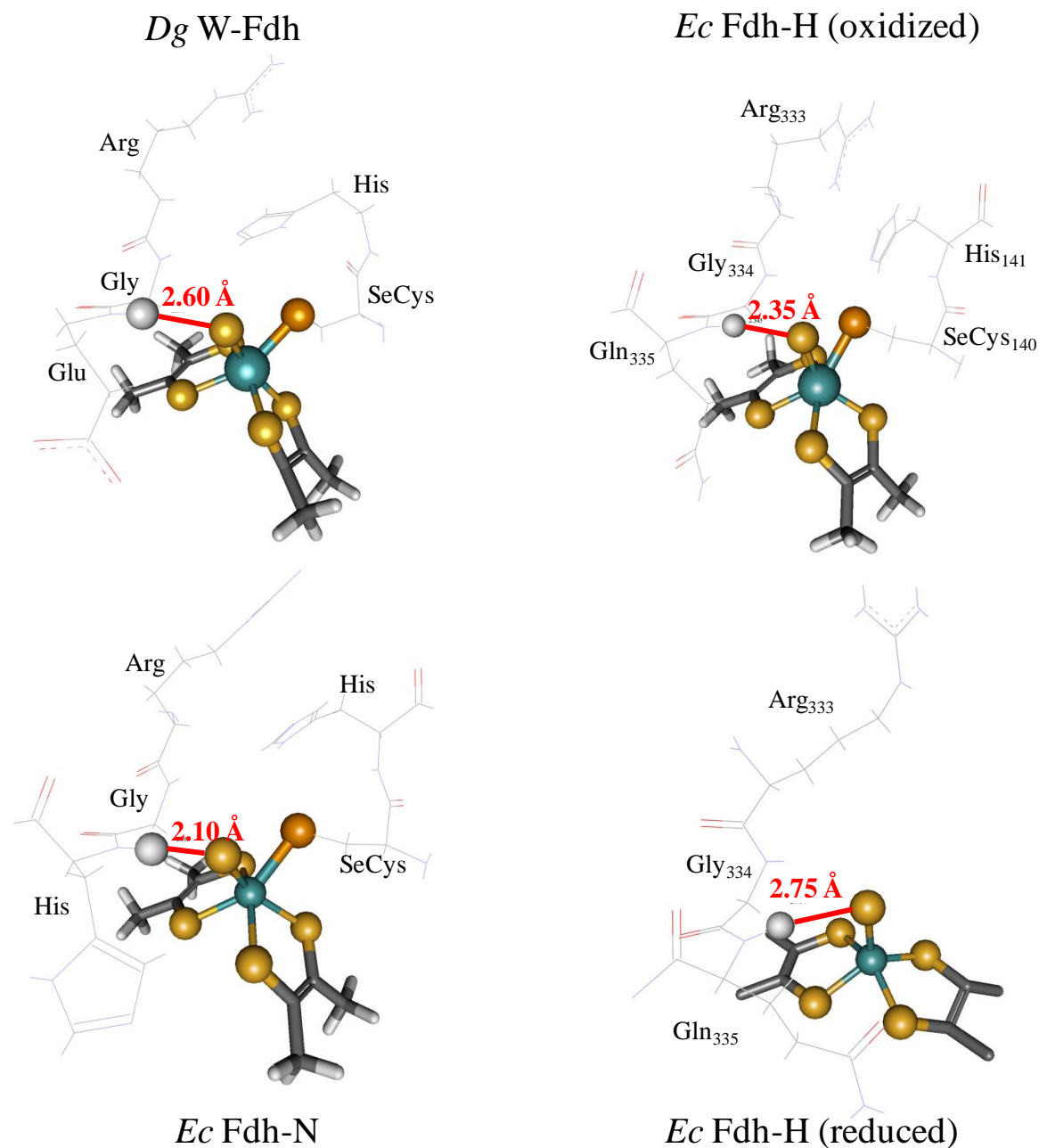


**Figure IV.16| Mo- and W-dependent Fdhs active site-core.** Close-up view of the active site of Mo- and W-dependent formate dehydrogenases. The H-S<sub>i</sub> distance is written in red and the relevant aminoacids in black. Atom color code: white, hydrogen; yellow, sulfur; dark yellow, selenium; cyan, molybdenum.

## IV.6 References

- 1 Boyington, J. C., Gladyshev, V. N., Khangulov, S. V., Stadtman, T. C. & Sun, P. D. Crystal structure of formate dehydrogenase H: catalysis involving Mo, molybdopterin, selenocysteine, and an Fe<sub>4</sub>S<sub>4</sub> cluster. *Science* 275, 1305-1308, (1997).
- 2 Raaijmakers, H. C. & Romao, M. J. Formate-reduced E. coli formate dehydrogenase H: The reinterpretation of the crystal structure suggests a new reaction mechanism. *J Biol Inorg Chem* 11, 849-854, (2006).
- 3 Costa, C., Teixeira, M., LeGall, J., Moura, J. J. G. & Moura, I. Formate dehydrogenase from *Desulfovibrio desulfuricans* ATCC27774: isolation and spectroscopic characterization of the active sites (heme, iron- sulfur centers and molybdenum). *J Biol Chem* 2, 198-208, (1997).
- 4 Rivas, M. G., Gonzalez, P. J., Brondino, C. D., Moura, J. J. & Moura, I. EPR characterization of the molybdenum(V) forms of formate dehydrogenase from *Desulfovibrio desulfuricans* ATCC 27774 upon formate reduction. *J Inorg Biochem* 101, 1617-1622, (2007).
- 5 Khangulov, S. V., Gladyshev, V. N., Dismukes, G. C. & Stadtman, T. C. Selenium-containing formate dehydrogenase H from *Escherichia coli*: a molybdopterin enzyme that catalyzes formate oxidation without oxygen transfer. *Biochemistry* 37, 3518-3528, (1998).
- 6 Axley, M. J., Bock, A. & Stadtman, T. C. Catalytic properties of an *Escherichia coli* formate dehydrogenase mutant in which sulfur replaces selenium. *Proc Natl Acad Sci U S A* 88, 8450-8454, (1991).
- 7 Leopoldini, M., Chiodo, S. G., Toscano, M. & Russo, N. Reaction mechanism of molybdoenzyme formate dehydrogenase. *Chemistry* 14, 8674-8681, (2008).
- 8 Liu, M. C. & Peck, H. D., Jr. The isolation of a hexaheme cytochrome from *Desulfovibrio desulfuricans* and its identification as a new type of nitrite reductase. *J Biol Chem* 256, 13159-13164, (1981).
- 9 Legall, J., Mazza, G. & Dragoni, N. [Cytochrome C3 of *Desulfovibrio Gigas*.]. *Biochim Biophys Acta* 99, 385-387, (1965).
- 10 Mota, C. S., Durand, M.-C., Gonzalez, P. J., Brondino, C. D., Moura, J. J. G., Moura, I., Dolla, A. & Rivas, M. G. Effects of molybdate and tungstate in the

- genes expression levels and biochemical characteristics of formate dehydrogenases produced by *Desulfovibrio alaskensis*. Submitted, (2010).
- 11 Almendra, M. J., Brondino, C. D., Gavel, O., Pereira, A. S., Tavares, P., Bursakov, S., Duarte, R., Caldeira, J., Moura, J. J. & Moura, I. Purification and characterization of a tungsten-containing formate dehydrogenase from *Desulfovibrio gigas*. *Biochemistry* 38, 16366-16372, (1999).
  - 12 Jormakka, M., Tornroth, S., Abramson, J., Byrne, B. & Iwata, S. Purification and crystallization of the respiratory complex formate dehydrogenase-N from *Escherichia coli*. *Acta Crystallogr D Biol Crystallogr* 58, 160-162, (2002).
  - 13 Jormakka, M., Tornroth, S., Byrne, B. & Iwata, S. Molecular basis of proton motive force generation: structure of formate dehydrogenase-N. *Science* 295, 1863-1868, (2002).
  - 14 Raaijmakers, H., Macieira, S., Dias, J. M., Teixeira, S., Bursakov, S., Huber, R., Moura, J. J., Moura, I. & Romao, M. J. Gene sequence and the 1.8 Å crystal structure of the tungsten-containing formate dehydrogenase from *Desulfovibrio gigas*. *Structure* 10, 1261-1272, (2002).
  - 15 Gaussian 03 v. Gaussian 03 v.revision D.01/D.02 (Gaussian, Inc., Pittsburgh, Pa, 2003).
  - 16 Becke, A. D. Density-functional thermochemistry. III. The role of exact. *J Chem Phys* 98, 5648-5652, (1993).
  - 17 Lee, C. T., Yang, W. T. & Parr, R. G. Development of the Colle-Salvetti Correlation-Energy Formula into a Functional of the Electron-Density. *Phys Rev B* 37, 785-789, (1988).
  - 18 Stephens, P. J., Devlin, F. J., Chabalowski, C. F. & Frisch, M. J. Ab-Initio Calculation of Vibrational Absorption and Circular-Dichroism Spectra Using Density-Functional Force-Fields. *J Phys Chem* 98, 11623-11627, (1994).
  - 19 Vosko, S. H., Wilk, L. & Nusair, M. Accurate Spin-Dependent Electron Liquid Correlation Energies for Local Spin-Density Calculations - a Critical Analysis. *Can J Phys* 58, 1200-1211, (1980).
  - 20 Ramos, M. J. & Fernandes, P. A. Computational Enzymatic Catalysis. *Acc Chem Res*, (2008).

- 21 Cerqueira, N. M., Fernandes, P. A., Eriksson, L. A. & Ramos, M. J. Dehydration of ribonucleotides catalyzed by ribonucleotide reductase: the role of the enzyme. *Biophys J* 90, 2109-2119, (2006).
- 22 Cerqueira, N. M. F. S. A., Fernandes, P. A., Eriksson, L. A. & Ramos, M. J. New insights into a critical biological control step of the mechanism of Ribonucleotide reductase. *J Mol Struct: Teochem* 709, 53-65, (2004).
- 23 Himo, F. Quantum chemical modeling of enzyme active sites and reaction mechanisms. *Theor Chem Acc* 116, 232-240, (2006).
- 24 Axley, M. J. & Grahame, D. A. Kinetics for formate dehydrogenase of *Escherichia coli* formate-hydrogenlyase. *J Biol Chem* 266, 13731-13736, (1991).
- 25 Cerqueira, N. M., Gonzalez, P. J., Brondino, C. D., Romao, M. J., Romao, C. C., Moura, I. & Moura, J. J. The effect of the sixth sulfur ligand in the catalytic mechanism of periplasmic nitrate reductase. *J Comput Chem* 30, 2466-2484, (2009).
- 26 Moura, J. J., Brondino, C. D., Trincao, J. & Romao, M. J. Mo and W bis-MGD enzymes: nitrate reductases and formate dehydrogenases. *J Biol Inorg Chem* 9, 791-799, (2004).
- 27 Brondino, C. D., Rivas, M. G., Romao, M. J., Moura, J. J. & Moura, I. Structural and electron paramagnetic resonance (EPR) studies of mononuclear molybdenum enzymes from sulfate-reducing bacteria. *Acc Chem Res* 39, 788-796, (2006).
- 28 Najmudin, S., Gonzalez, P. J., Trincao, J., Coelho, C., Mukhopadhyay, A., Cerqueira, N. M., Romao, C. C., Moura, I., Moura, J. J., Brondino, C. D. & Romao, M. J. Periplasmic nitrate reductase revisited: a sulfur atom completes the sixth coordination of the catalytic molybdenum. *J Biol Inorg Chem* 13, 737-753, (2008).
- 29 Castillo, R., Oliva, M., Marti, S. & Moliner, V. A theoretical study of the catalytic mechanism of formate dehydrogenase. *J Phys Chem B* 112, 10012-10022, (2008).



# **Chapter V**

*Inhibition studies on Fdhs*

## V.1 Summary

The kinetics properties of Fdh from three *Desulfovibrio* species in presence of inhibitors were studied. Nitrate inhibits the formate oxidation in a competitive way with  $K_{ic}$  values of  $0.6 \pm 0.2$  mM,  $2.6 \pm 0.4$  mM and  $4.7 \pm 0.1$  mM for *Dd*, *Dg*, and *Da* Fdh, respectively. Azide is a strong inhibitor of these enzymes and presents a mixed inhibition behavior for the three Fdhs studied ( $K_{ic}=0.030 \pm 0.003$  mM and  $K_{iuc}=0.200 \pm 0.003$  mM for *Dd* Fdh,  $K_{ic}=0.3 \pm 0.1$  mM and  $K_{iuc}=0.5 \pm 0.2$  mM for *Dg* Fdh, and  $K_{ic}= 0.20 \pm 0.03$  mM and  $K_{iuc}= 0.4 \pm 0.1$  mM for *Da* Fdh). Cyanide inhibits only the Mo-Fdh from *D. desulfuricans* in a mixed way with  $K_{ic}=0.40 \pm 0.03$  mM and  $K_{iuc}= 1.6 \pm 0.2$  mM.

A multiple sequence alignment between the W-Fdhs from *D. gigas* and *D. alaskensis* and the Mo-Fdh from *D. desulfuricans* revealed high similarity for the corresponding  $\alpha$  and  $\beta$  subunits. The only relevant differences between them are the metal present in the active site (Mo or W) and the presence of a  $\gamma$  subunit in the *Dd* Mo-Fdh. The kinetic properties of different Fdhs in presence of inhibitors are discussed based on the structural characteristics of each enzyme.

## V.2 Introduction

Inhibitors are substances that decrease the rate of an enzyme-catalysed reaction. These substances can be grouped in two main classes: reversible or irreversible inhibitors. Irreversible inhibitors are substances that inactivate the enzyme by covalent bonding or degradation of the active site. In contrast, reversible inhibition is suggested when inhibitors form dynamics complexes with the enzyme that result in a different catalytic behaviour from those of the uncombined enzyme [1].

Three common inhibitors of Mo and W enzymes were tested as inhibitors of Fdh: azide, cyanide and nitrate. The strong inhibitor properties of azide and cyanide were demonstrated not only for several Fdhs [2-5] but also for other Mo-enzymes such as xanthine oxidase from bovine milk, xanthine dehydrogenase from chicken liver, aldehyde oxidase from rabbit liver [6], periplasmatic nitrate reductases (Nap) from *D. desulfuricans* and *P. denitrificans* [7,8], respiratory nitrate reductase from *E. coli* [9] and formylmethanofuran dehydrogenases from *M. barkeri*, *M. thermoautotrophicum* and *M. wolfei* [10]. Studies on the Mo-containing Fdh-H from *E. coli* showed a



competitive inhibition pattern by nitrate and a noncompetitive inhibition by azide [3]. Although the Mo-Fdh from *D. desulfuricans* was also found to be inhibited in a competitive way by nitrate, azide and cyanide inhibits the enzyme in a mixed manner [2]. Regarding to the coordination geometry of the Fdh active site in presence of inhibitors, it was proposed an active site rearrangement for the reaction mechanism in presence of azide [2,11,12].

Nitrate is predicted to be a inhibitor or a substrate of Fdhs due to the high similarity between the catalytic subunits and active sites of Fdh and periplasmic nitrate reductases from bacteria. A comparison of the active sites and the structure in the nearest-neighbours shows some differences in the aminoacids composition with relevant function on the enzyme catalysis. In this sense, in periplasmic nitrate reductases there are respectively a metionine and a cysteine instead of the histidine and SeCys present in Fdhs (figure V.1) [13].

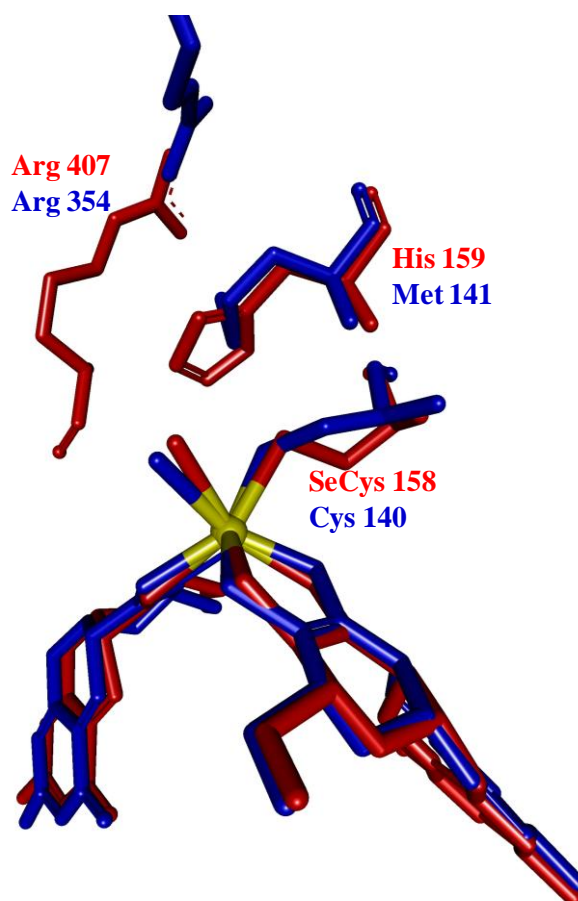


**Figure V.1| Comparison of the Nap and Fdh active site-core.** Superposition of W-Fdh from *D. gigas* (red) and NapA (blue) from *D. desulfuricans* (PDBs: 1H0H and 2JIM).

This chapter reports inhibition studies of the heterotrimeric Mo-Fdh from *D. desulfuricans* ATCC 27774 and the heterodimeric W-Fdhs isolated from *D. gigas* and *D. alaskensis*. The main objectives are to compare the catalytic properties of these enzymes in the presence of inhibitors to obtain information about the mechanisms of inhibition and to evaluate the relevance of some aminoacids in the active site-core during formate oxidation.

### V.3 Experimental procedures

**V.3.1 Bacterial strain, culture media, and growth conditions.** *D. desulfuricans* cells were grown in lactate-nitrate medium as described by Liu Peck [14], *D. gigas* cells were cultured in lactate-sulfate medium [15] and *D. alaskensis* cells were grown in a modified medium C from Postgate supplemented with 10  $\mu$ M of Na<sub>2</sub>WO<sub>4</sub>·2H<sub>2</sub>O as described in the experimental procedures section from chapter III (section III.3.1). In all cases, cells were grown under anaerobic conditions at 37°C and collected by centrifugation at the end of the exponential phase.

**V.3.2 Enzymes purification.** Soluble extracts were obtained as described in Chapter III (section III.3.3) and dialyzed overnight against 5 mM Tris-HCl pH 7.60. All soluble extract preparation and purification were performed at 4 °C.

*Dd* Mo-Fdh, *Da* W-Fdh and *Dg* W-Fdh were purified as described in Rivas *et al* [2], experimental procedures from chapter III (section III.3.3) and chapter IV (section IV.3.2), respectively.

**V.3.3 Fdhs sequences and three-dimensional structures alignments.** Clustal-W from [www.expasy.org](http://www.expasy.org) was used to analyze and align the Fdhs sequences. Swiss-PDB viewer v4.0.1 was used to modulate and to perform 3D alignments of the structures. Figures were drawn in Discovery Studio Visualizer v2.5.1.9167.

**V.3.4 Enzyme inactivation test.** *D. desulfuricans* Fdh (3  $\mu$ M) in 60 mM Tris-HCl (pH 8.0) was incubated with 10 mM potassium cyanide or 10 mM sodium azide in a final volume of 250  $\mu$ L during 2 hours at 4°C. To remove the inhibitors, the buffere was exchanged to 60 mM Tris-HCl, pH 8.0, using a 30 kDa cut-off Centricon (GE

Healthcare). Enzyme activity was measured before incubation with inhibitors, after incubation and after the inhibitor removal.

**V.3.5 Enzyme kinetic assays.** Steady-state kinetic studies on Fdhs were performed as described in Chapter III (section III.32). Enzyme and substrate concentrations were in the range of 10 to 35 nM and 5 to 500 μM, respectively. Inhibition studies were performed adding potassium nitrate, sodium azide and potassium cyanide together with the electron acceptor (0.25 to 10 mM of inhibitor).

**V.3.6 Analysis of initial rate data.** Initial rates vs. substrate concentration were plotted and fitted using the Michaelis-Menten equation (eq. 5.1). Kinetic parameters  $K_M$  (Michaelis constant) and  $V$  (maximum rate) were calculated using the Direct Linear Plot method as described by Cornish-Bowden (eq. 5.2) [1].

(equation 5.1)

$$v = \frac{Va}{K_M + a}$$

(equation 5.2)

$$V = v + \frac{v}{a}K_M$$

Where  $v$  is the initial rate, and  $a$  the substrate concentration.

The experimental data obtained from inhibition assays were plotted and fitted with a Michaelis-Menten model that describes the effect of competitive and mixed inhibitions mechanisms (eq. 5.3 and 5.4, respectively).

(equation 5.4)

$$v = \frac{Va}{K_M \left(1 + \frac{i}{K_{ic}}\right) + a}$$

(equation 5.3)

$$v = \frac{Va}{K_M \left(1 + \frac{i}{K_{ic}}\right) + a \left(1 + \frac{i}{K_{iuc}}\right)}$$

Where  $v$  is the initial rate,  $V$  is the maximal rate,  $a$  is the substrate concentration,  $K_M$  is the Michaelis-Menten constant,  $i$  is the inhibitor concentration,  $K_{ic}$  is the competitive inhibition constant, and  $K_{iuc}$  is the uncompetitive inhibition constant.

Direct linear plots were used to identify the type of inhibition. The determination of  $K_{ic}$  and  $K_{iuc}$  were performed using Dixon and Cornish plots, as described by Cornish-Bowden [1].

## V.4 Results

### V.4.1 Inhibition studies

#### V.4.1.1 Inhibition by nitrate.

Figure V.2 shows the dependence of the initial rates using a fixed substrate concentration versus nitrate concentration for the three Fdhs studied. The initial rates decrease when the nitrate concentration increases, revealing that this molecule is an inhibitor of the three Fdhs studied.

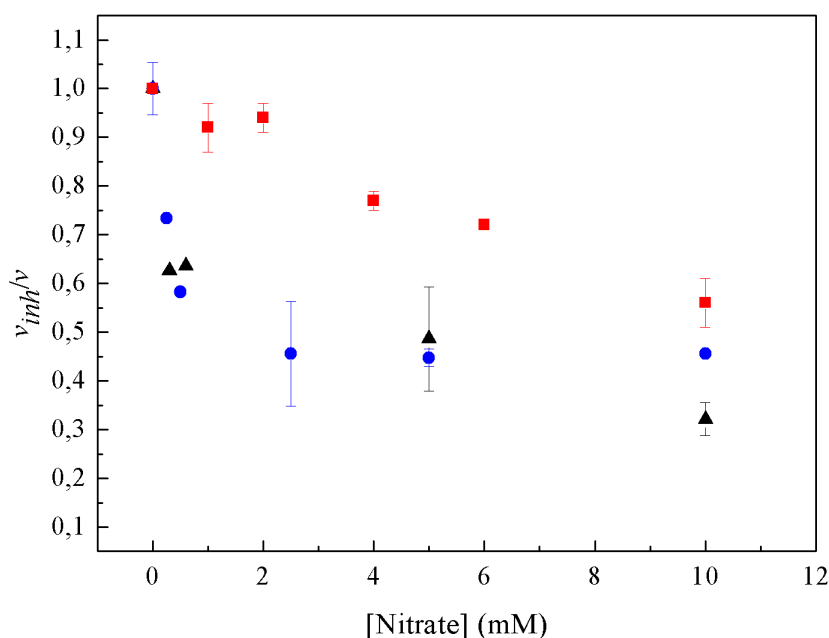


**Figure V.2| Normalized initial rates vs. nitrate concentration.** (■): Fdh from *D. desulfuricans* (35 nM); (▲): Fdh from *D. gigas* (35 nM); (●): Fdh from *D. alaskensis* (10 nM).

Conditions used as described in section V.3.5, 10 mM of formate was used.

The inhibition type and the determination of the inhibition constants using nitrate are shown in figures V.3, V.4 and V.5 for the Fdh from *D. desulfuricans*, *D. gigas* and *D. alaskensis*, respectively.

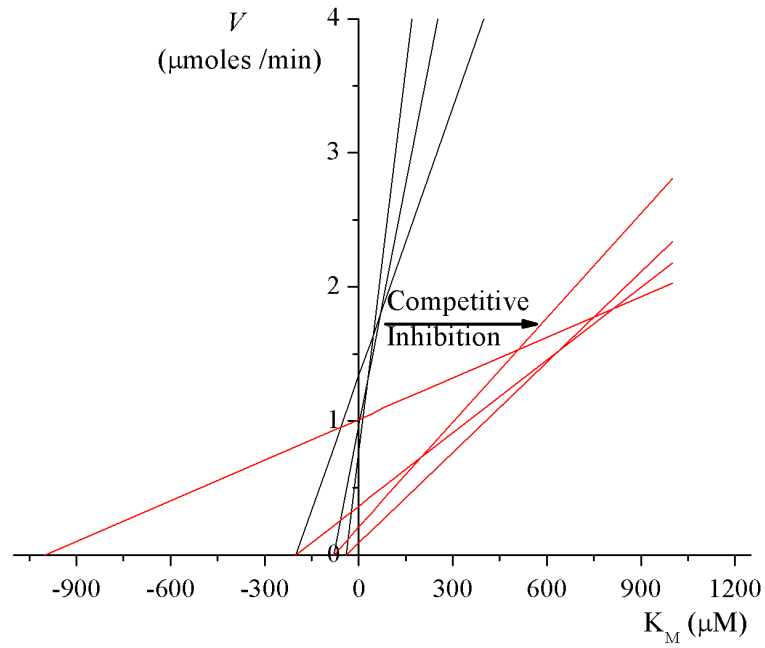


**Figure V.3| Inhibition type characterization of Fdh from *D. desulfuricans* by nitrate.**

Direct linear plot showing competitive inhibition. Black and red lines correspond to the experiments in absence and presence of 20 mM of nitrate, respectively; Inhibition constant ( $K_{ic}$ ) determined by Rivas *et al* [16].

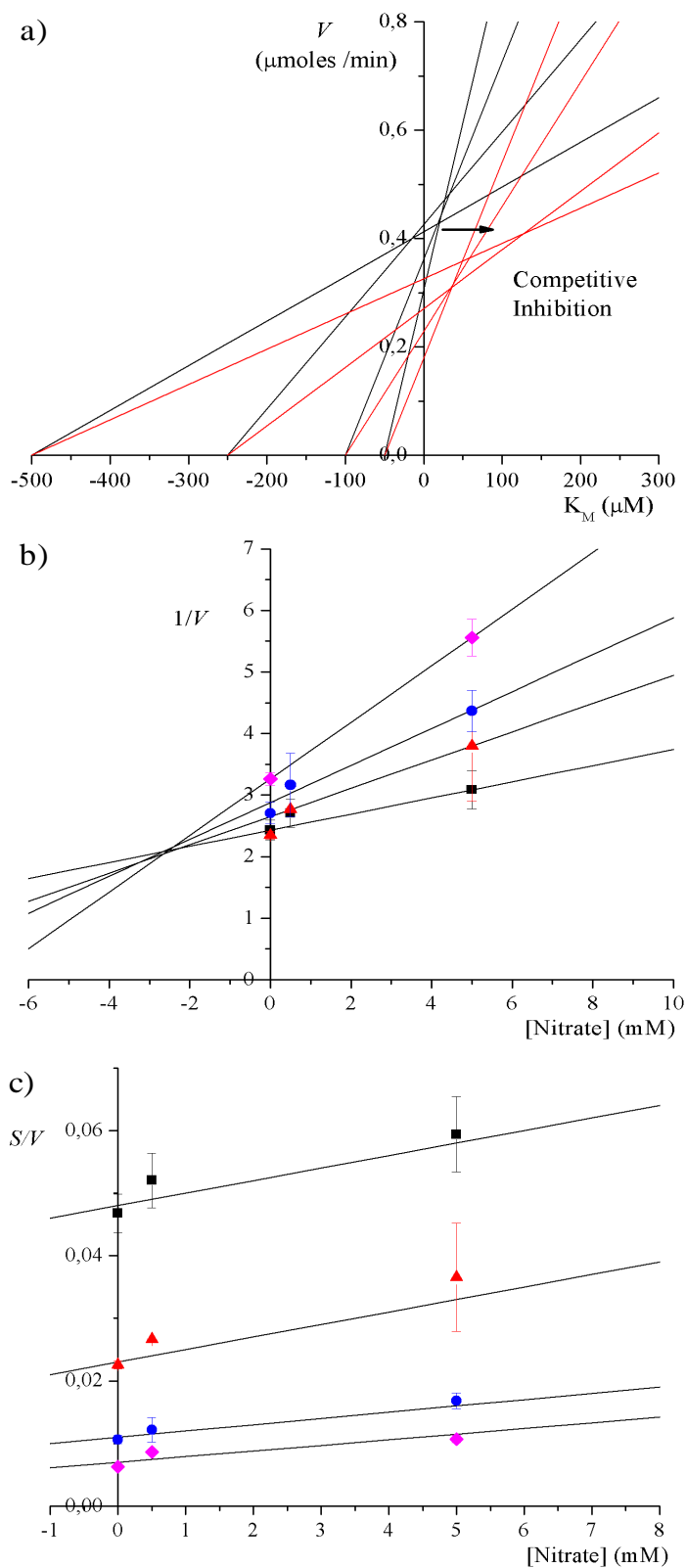


**Figure V.4 Inhibition type characterization of *Dg Fdh* by nitrate.** (a) Direct linear plot showing competitive inhibition. Black and red lines correspond to the experiments in absence and presence of 10 mM of nitrate, respectively; (b) Dixon plot used to calculate  $K_{ic}$ . (c) Parallel pattern of Cornish-Bowden plot showing competitive inhibition. Formate concentrations used:

(■) 500  $\mu\text{M}$ , (▲) 250  $\mu\text{M}$ , (●) 100  $\mu\text{M}$  and (◆) 50  $\mu\text{M}$ .

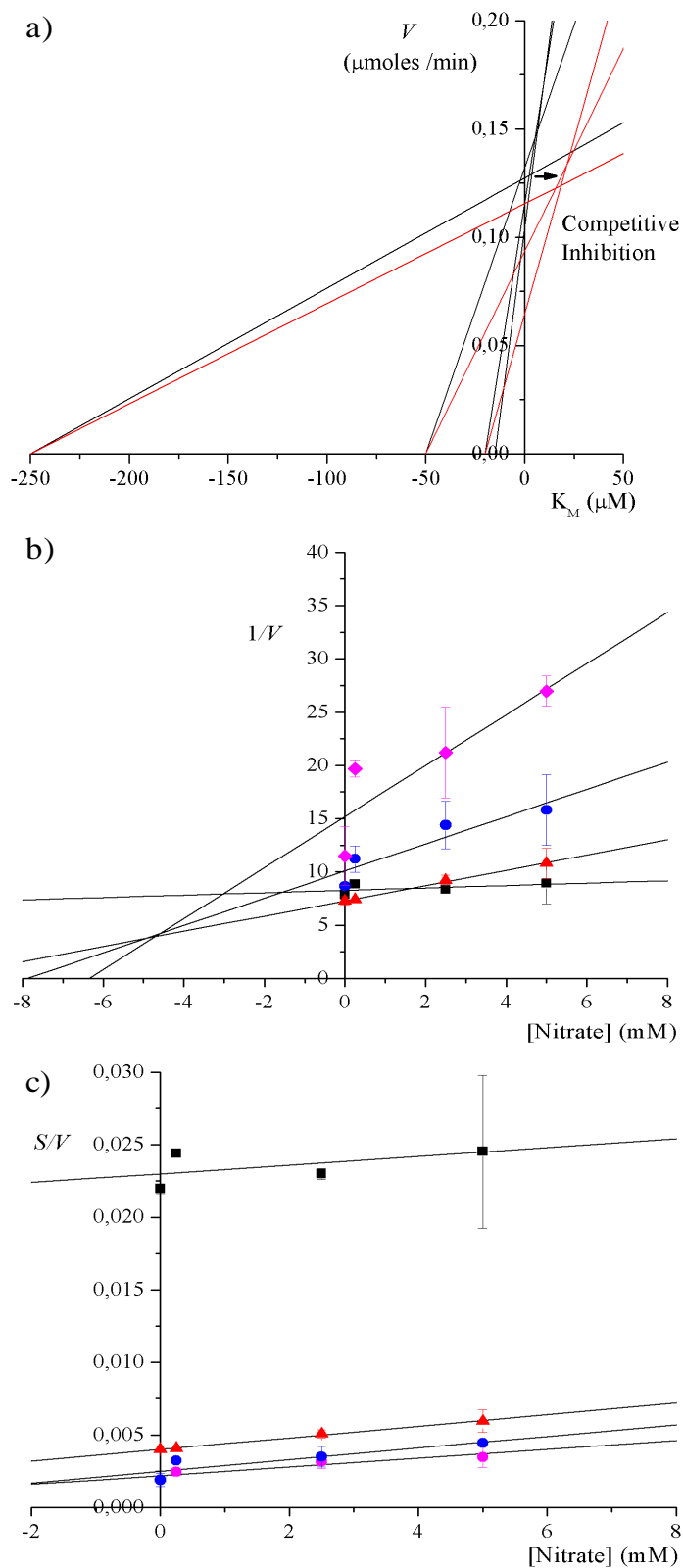


**Figure V.5] Inhibition type characterization of Fdh from *D. alaskensis* by nitrate.** (a) Direct linear plot showing competitive inhibition. Black and red lines correspond to the experiments in the presence or absence of 5 mM of nitrate, respectively; (b) Dixon plot used to calculate  $K_{ic}$ . (c) Parallel pattern of Cornish-Bowden plot showing competitive inhibition. Formate concentrations used: (■) 250  $\mu\text{M}$ , (▲) 50  $\mu\text{M}$ , (●) 20  $\mu\text{M}$  and (◆) 12.5  $\mu\text{M}$ .

Direct Linear Plots presented in figures V.3a, V.4a and V.5a indicate that  $k_{cat}$  is not affected, while  $K_M$  values change as the nitrate concentration increases. This indicates that, as already shown for the *Ec* Fdh-H [3], nitrate is in all these cases a competitive Fdh inhibitor. These results are supported by the Cornish-Bowden Plots that showed parallels lines (figures V.4c and V.5c, *D. gigas* and *D. alaskensis*, respectively). The  $K_{ic}$  determined by Dixon Plots are summarized in table V.1.

**Table V.1** | Fdh inhibition constants using nitrate as inhibitor determined by Dixon plots.

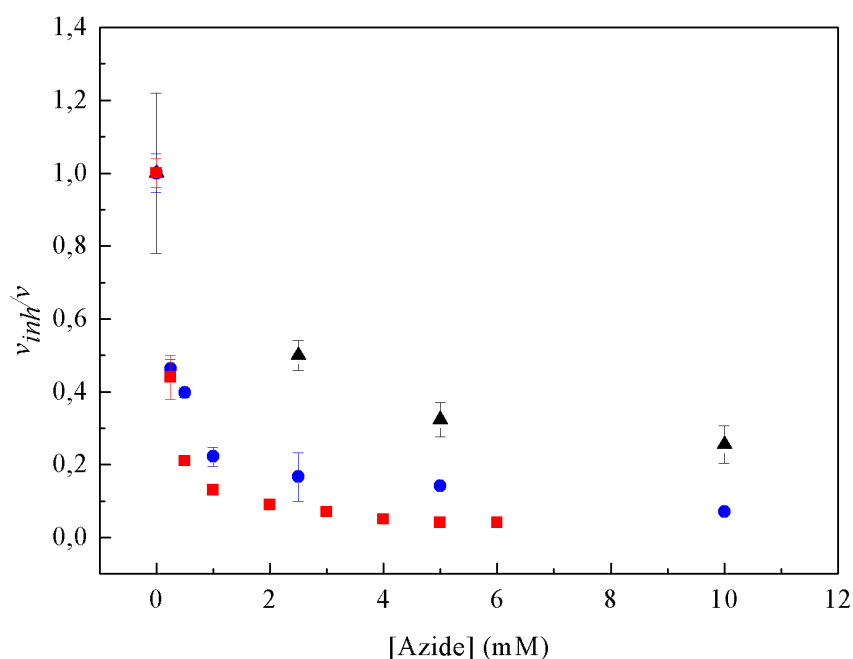
	<b><math>K_{ic}</math> (mM)</b>
Mo-Fdh	$0.6 \pm 0.2$
<i>D. desulfuricans</i>	(from reference [16])
W-Fdh	
<i>D. gigas</i>	$2.6 \pm 0.4$
W-Fdh	
<i>D. alaskensis</i>	$4.7 \pm 0.1$



#### V.4.1.2 Inhibition by azide

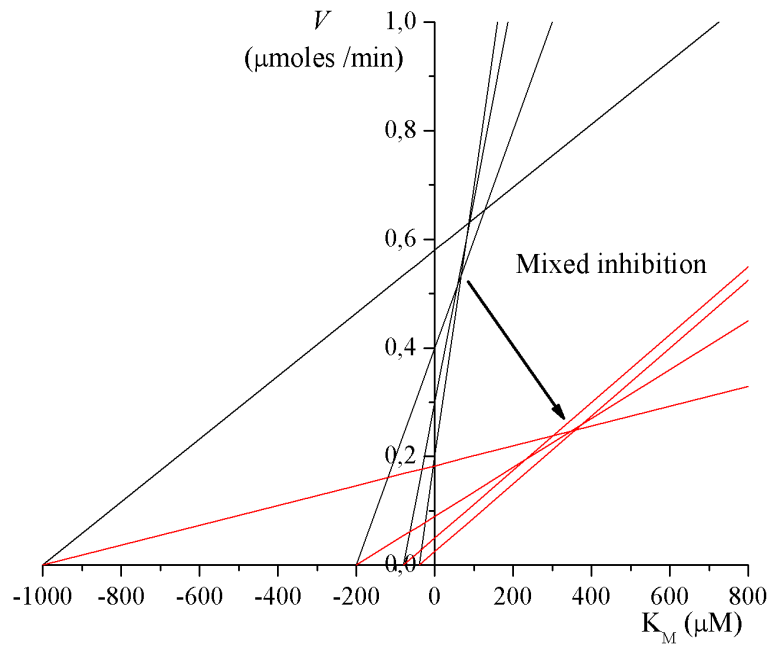
Since azide is a potent inhibitor of most Fdhs [3,17], this compound was also tested. Inactivation by azide was evaluated for Fdh from *D. desulfuricans* and was established that it is a reversible inhibitor. The results obtained show that this enzyme recovers at least 70% of activity after incubation with azide.

Figure V.6 shows the ratio between the initial rate in presence of inhibitor and the initial rate in absence of azide versus azide concentration for all the three enzymes under study.



**Figure V.6| Normalized initial rates vs. azide concentration.** (■): Fdh from *D. desulfuricans* (35 nM); (▲): Fdh from *D. gigas* (35nM); (●): Fdh from *D. alaskensis* (10 nM). Conditions used as described in section V.3.5, 10 mM of formate was used.

The type of inhibition and inhibition constants for Fdh from *D. desulfuricans*, *D. gigas* and *D. alaskensis* are shown in figures V.7, V.8 and V.9, respectively.



**Figure V.7| Characterization of the inhibition type by azide for the *Dd* Fdh.** (a) Direct linear plot showing mixed inhibition. Black and red lines correspond to the experiments in absence and presence of 0.5 mM of azide, respectively; (b) Inhibition constants ( $K_{ic}$  and  $K_{iuc}$ ) determined by Rivas *et al* [2,16].

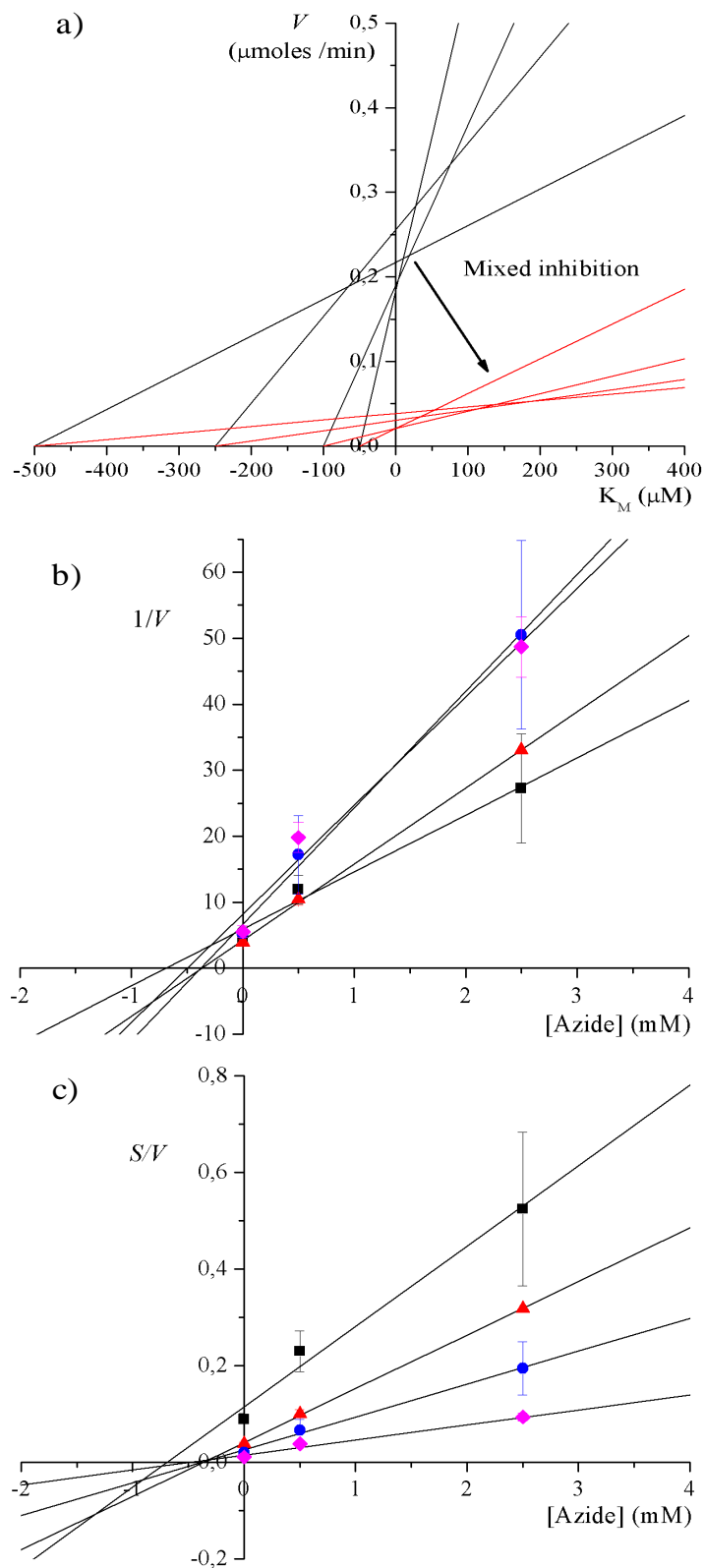


**Figure V.8| Characterization of the inhibition type by azide for the *Dg Fdh*.** (a) Direct linear plot showing mixed inhibition. Black and red lines correspond to the experiments in absence and presence of 10 mM of azide, respectively; (b) Dixon plot used to calculate  $K_{ic}$ . (c) Cornish-Bowden plot used to calculate  $K_{iuc}$ . Formate concentrations used: (■) 500  $\mu\text{M}$ , (▲) 250  $\mu\text{M}$ , (●) 100  $\mu\text{M}$  and (◆) 50  $\mu\text{M}$ .

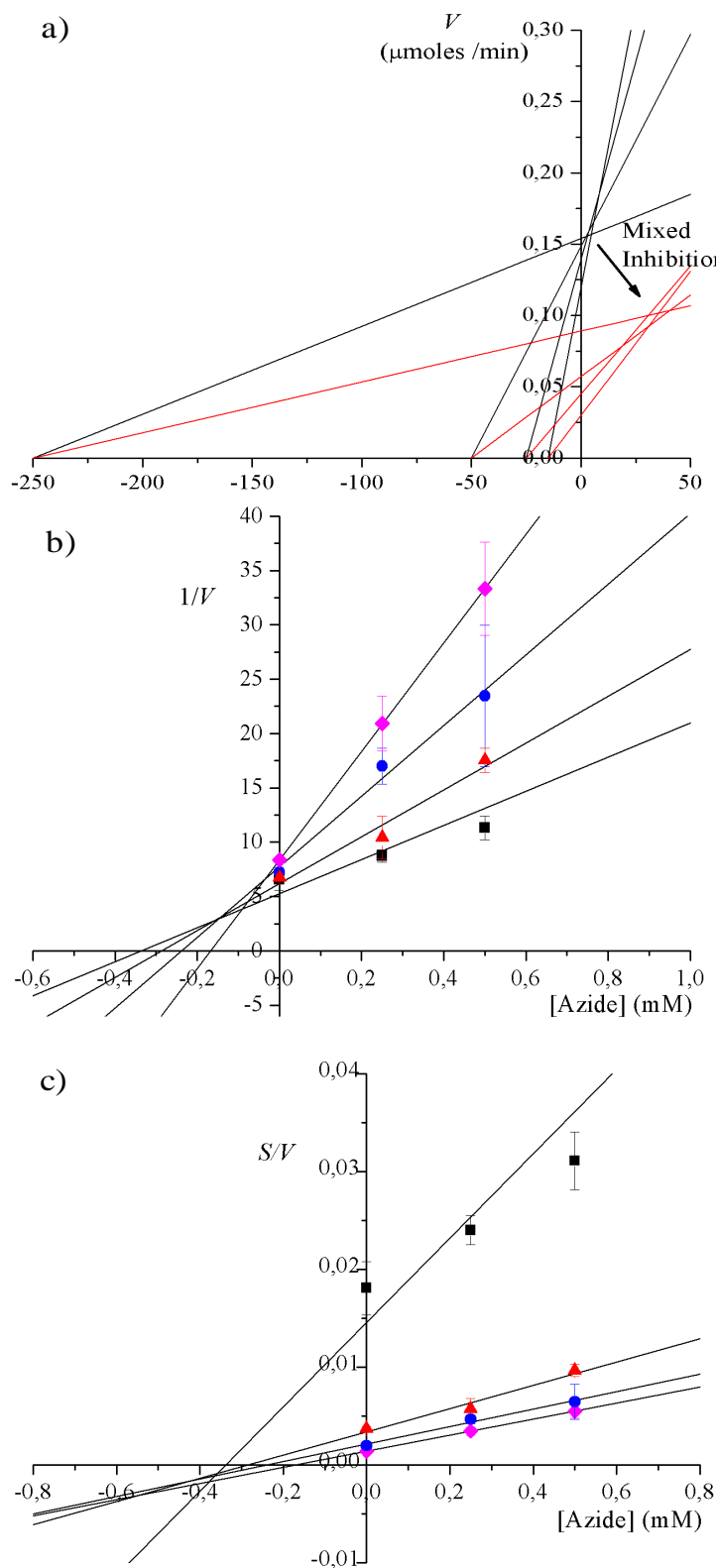


**Figure V.9| Characterization of the inhibition type by azide for the *Da Fdh*.** (a) Direct linear plot showing mixed inhibition. Black and red lines correspond to the experiments in absence and presence of 0.5 mM of azide, respectively; (b) Dixon plot used to calculate  $K_{ic}$ . (c) Cornish-Bowden plot used to calculate  $K_{iuc}$ . Formate concentrations used: (■) 250  $\mu\text{M}$ , (▲) 50  $\mu\text{M}$ , (●) 25  $\mu\text{M}$  and (◆) 15  $\mu\text{M}$ .

Since it is observed that both  $k_{cat}$  and  $K_M$  are affected by the presence of azide (figures V.7a, V.8a, and V.9a), it can be concluded that this molecule inhibit Fdhs in a mixed way. The inhibition constants ( $K_{ic}$  and  $K_{iuc}$ ) are presented in table V. 2.

**Table V.2| Fdh inhibition constants with azide determined by Dixon and Cornish-Bowden plots.**

	<b><math>K_{ic}</math> (mM)</b>	<b><math>K_{iuc}</math> (mM)</b>
Mo-Fdh <i>D. desulfuricans</i>	$0.030 \pm 0.003$ (from ref. [2,16])	$0.200 \pm 0.003$ (from ref. [2,16])
W-Fdh <i>D. gigas</i>	$0.3 \pm 0.1$	$0.5 \pm 0.2$
W-Fdh <i>D. alaskensis</i>	$0.20 \pm 0.03$	$0.4 \pm 0.1$

### V.4.1.3 Inhibition by cyanide

Cyanide, a common inhibitor of many molybdoenzymes [18], was also studied in the present work.

Figure V.10 shows the ratio between initial rate in presence of cyanide over initial rates in absence of inhibitor versus cyanide concentration. An unexpected result was obtained as only the Fdh isolated from *D. desulfuricans* is affected by the presence of this inhibitor.

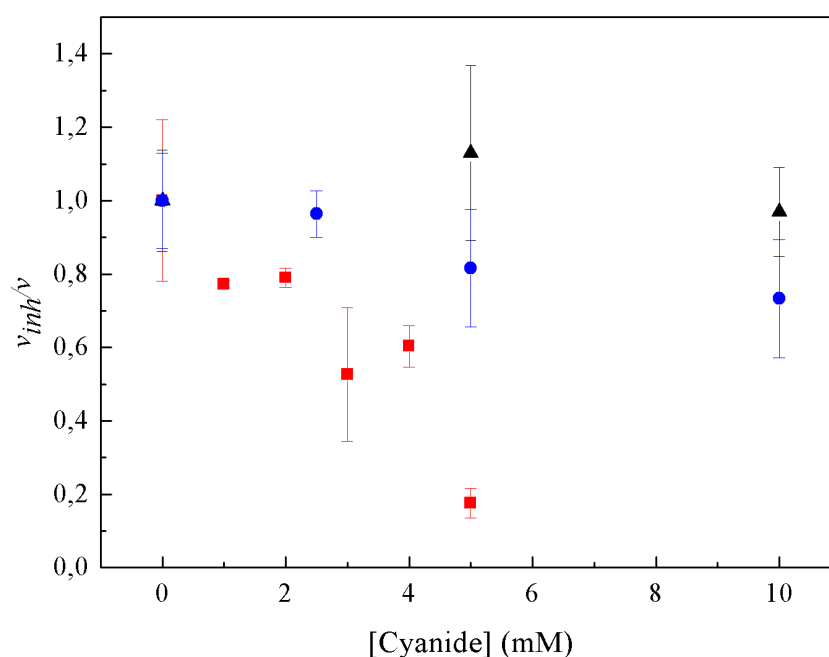


**Figure V.10| Normalized initial rates vs. cyanide concentration.** (■): Fdh from *D. desulfuricans* (35 nM); (▲): Fdh from *D. gigas* (35 nM); (●): Fdh from *D. alaskensis* (35 nM). Conditions used as described in section V.3.5, 10 mM of formate was used.

It is largely known that cyanide can inactivate Mo enzymes with a terminal sulphur ligand by a process called cyanolysis [18]. The reversibility of inhibition by cyanide was tested for Fdh from *D. desulfuricans* as explained in the experimental procedures section of this chapter. Samples treated with cyanide and dialyzed against cyanide-free buffer recovered c.a. 80% of the specific activity compared to control samples, confirming that cyanide, like azide, is a reversible inhibitor.

The type of inhibition of Fdh from *D. desulfuricans* with cyanide was determined by the Direct Linear Plot (figure V.11) as described by Cornish-Bowden [1], the  $K_{ic}$  and the  $K_{iuc}$  were determined by Dixon and Cornish-Bowden plots, respectively.

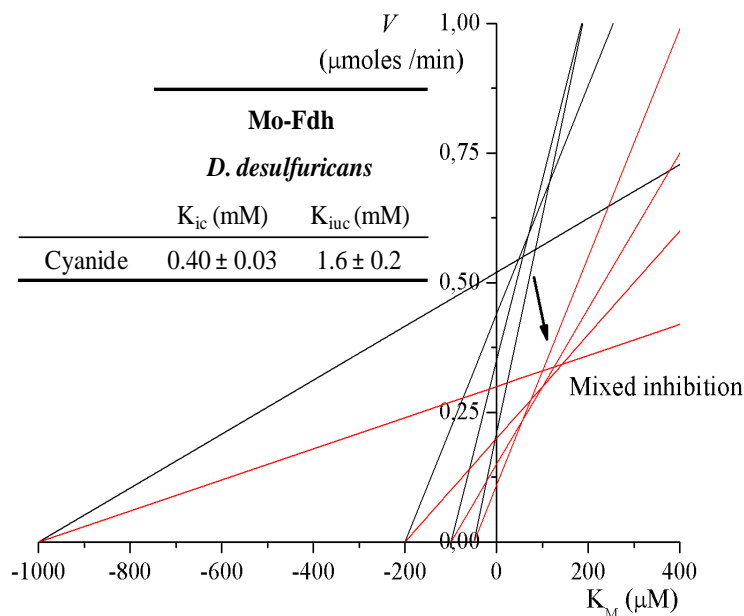


**Figure V.11| Characterization of the inhibition type by cyanide for the *Dd* Fdh.** Direct linear plot showing mixed inhibition. Black and red lines correspond to the experiments in absence and presence of 2.5 mM of cyanide, respectively; Inhibition constants ( $K_{ic}$  and  $K_{iuc}$ ) determined by Rivas *et al* [2,16].

The Direct Linear Plot for Mo-Fdh from *D. desulfuricans* in the presence (red) and absence (black) of cyanide show a mixed inhibition pattern (figure V.11). The  $K_{ic}$  and  $K_{iuc}$  values were calculated to be  $0.40 \pm 0.03$  mM and  $1.6 \pm 0.2$  mM, respectively [2,16].

#### V.4.2 Homology between $\alpha$ and $\beta$ subunits of Fdhs.

In order to find an explanation of the observed kinetic properties of the Fdhs studied in this work, the amino acid sequence of the corresponding  $\alpha$  and  $\beta$  subunit were aligned (figure V.12 and V.13, respectively) and the percentage of homology and presence of conserved amino acids were evaluated (table V.3). Because the *Dg* and *Da* Fdhs have no third subunit, the c-type heme containing  $\gamma$  subunit from the *Dd* Fdh was excluded from this analysis.

The three  $\alpha$  subunits analyzed contain the common features and conserved amino acids commonly found in these enzymes. The twin-arginine motif (RRXFL/IK) that determines the periplasmic translocation is showed as light grey, the specific recognition site where the signal peptide is cleaved is marked with a black triangle, and the cysteine motif (CXXCX<sub>n</sub>CX<sub>m</sub>C) which coordinates the [4Fe-4S] center commonly





	310	320	330	340	350	360
FdhDg						
	LYFKDYV	VNYTNAS	FIVGEG	FAFEEGL	FAGYNK	ETRKYDK
FdhDa	LYFREYV	AEYTNAS	YIVSEK	YSFENG	FFSGFN	PEKRN
FdhDd	LYHKEYV	VNNYTNA	AFVVDG	YAFEDGL	FSGYDAA	ARKYDK
	***:***	:****:***	:***:***	:***:***	:***:***	:***:***
	370	380	390	400	410	420
FdhDg	HPRCVF	QIMKKH	YERYDL	DKISAI	CGTPKE	LILKVY
FdhDa	HPRCVL	NLLKHE	YERYTV	DKVVDI	TGTPRE	DLAVYK
FdhDd	NPRCVI	NLMKD	HYSRYT	LKNVSD	VTGVSQ	DNLLK
	:****:***	:***:***	:***:***	:***:***	:***:***	:***:***
	430	440	450	460	470	480
FdhDg	TVGVQN	IRAMSI	NQLLL	GNIGV	AGGGV	NALRGE
FdhDa	TVGVQN	IRAMAI	IQLLL	GNIGV	AGGGV	NALRGE
FdhDd	TVGVQN	IRLSSL	VQLLL	GNIGI	AGGGI	NALRGE
	*****	:***:***	:***:***	:***:***	:***:***	:***:***
	490	500	510	520	530	540
FdhDg	PTYEET	TKKFT	TPVSK	DPQSAN	WWSNF	PKYSAS
FdhDa	PTLADY	NKAN	TPVSK	DPMSAN	WWSNQ	NPKYVA
FdhDd	QTLGEY	NKAN	TPVT	VVPSAN	WWSNR	PKYVTS
	* :*. *	***: *	*****	* ***	:* :*. :	* . . *
	550	560	570	580	590	600
FdhDg	---DYS	WLT	TLFDD	MFQGI	KGF	FAWGQ
FdhDa	PMTDY	FWLSM	FEKMH	KEQFK	GFFAW	GMPAC
FdhDd	---DYS	YMFV	MDRIN	KKIK	GGFIM	GVNPM
	** :. :	:. :. :	:. :. :	:. :. :	:. :. :	:. :. :
	610	620	630	640	650	660
FdhDg	SFWRGP	DMDPK	KIKTE	VFFL	PCAVAI	EKEGS
FdhDa	SFWKGP	GMNPS	DIKTE	VFFL	PCAVS	IEKEGS
FdhDd	DNWQR	PGVDP	KTTE	VFFL	PSAHR	IEKAG
	. * :. :	:. :. :	:. :. :	:. :. :	:. :. :	:. :. :
	670	680	690	700	710	720
FdhDg	ELAKRV	QKLLA	KTPGK	LAAV	TKLKT	DYVND
FdhDa	ELMEKV	RHLYG	KEGG	VFPD	IMHLN	LDDW
FdhDd	PLFNT	IRRM	YKTE	GGVLP	EAVLQ	MH---
	* :. :	:. :. :	:. :. :	:. :. :	:. :. :	:. :. :



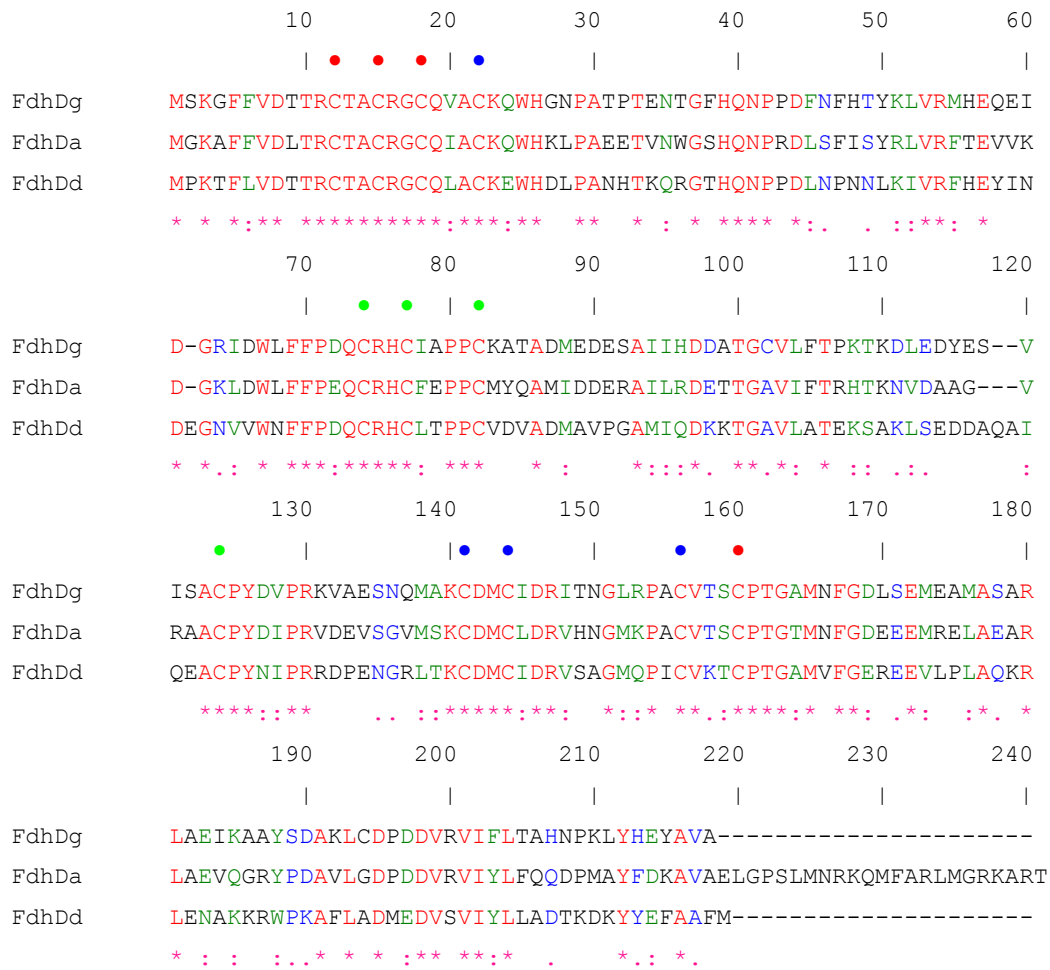


**Figure V.13| Aminoacids alignment of Fdhs β subunits.** FdhDg: β subunit from *D. gigas*; FdhDa: β subunit from *D. alaskensis*; FdhDd: β subunit from *D. desulfuricans*; ●, ●, and ●: cysteine motifs involved in the FeSII, FeSIII and FeSIV cluster binding; (\*): identity; (:): strongly similar; and (.) weekly similar.

The sequence similarity shown in table V.3 reveals high homology between these three Fdhs with at least 51% of identity between the catalytic  $\alpha$  subunits and no less than 46% of identity between the  $\beta$  subunits.

**Table V.3|** Alignment parameters between Mo-Fdh from *D. desulfuricans* (*Dd*) and W-Fdhs from *D. gigas* (*Dg*) and *D. alaskensis* (*Da*).

Alignments Subunit	<i>Dd vs Dg</i>		<i>Dd vs Da</i>		<i>Dg vs Da</i>	
	$\alpha$	$\beta$	$\alpha$	$\beta$	$\alpha$	$\beta$
Identity	53%	50%	51%	46%	66%	53%
Strongly similar	18%	18%	20%	19%	15%	15%
Weakly similar	8%	11%	9%	6%	6%	5%
Different	21%	21%	20%	29%	14%	27%

## V.5 Discussion

The type of inhibition of nitrate, azide and cyanide have been determined using steady-state kinetic studies. Primary sequence alignment analysis (Figure V.12 and V.13) show that the catalytic ( $\alpha$ ) and electron transfer ( $\beta$ ) subunits are highly similar, sharing above 50% of identity (table V.3). In agreement with this observation, the three dimensional alignment of the  $\alpha$ -subunits of the Fdhs analyzed in this chapter showed a very low RMSD for all backbone atoms (0.5 Å) and no obvious differences between the catalytic cores when fitted over the crystallographic structure of the W-containing Fdh from *D. gigas*. These structural similarities are reflected in the kinetic behaviour towards substrate, as observed for the similar  $K_M$  and  $k_{cat}$  values (table V.4), and inhibitors such as azide or nitrate.

**Table V.4|** Kinetic parameters using formate as substrate obtained by steady-state enzyme kinetic studies (data from Chapter IV, sectionIV.4.1).

	$k_{cat}$ ( $s^{-1}$ )	$K_M$ ( $\mu M$ )	$k_{cat}/K_M$
Mo-Fdh <i>D.desulfuricans</i>	347	64	5.4
W-Fdh <i>D.gigas</i>	174	51	3.4
W-Fdh <i>D.alaskensis</i>	241	10	24.1

The nitrate molecule is a relatively strong competitive inhibitor of Fdhs because nitrate is a polyatomic anion sharing similar stereochemistry with formate being the substrate of the structurally related periplasmic nitrate reductases. Although the results presented in this chapter show that nitrate is a competitive Fdh inhibitor, no nitrate reductase activity was observed (data not shown). Fdh from *D. alaskensis* seems to be the enzyme less sensible to nitrate inhibition, since this enzyme showed the higher  $k_{cat}/K_M$  ratio (table V.4).

In line with data reported for the *Ec* Fdh-H [3], azide is a reversible mixed inhibitor of the three Fdhs studied. The competitive component of azide shows to be predominant ( $K_{ic} < K_{iuc}$ ), which could be due to the structural analogy between this molecule and carbon dioxide, consequently blocking the substrate entrance similar to a product inhibition type. Other examples of Mo-enzymes from the same family of Mo/W-enzymes that are inhibited in a competitive manner by azide comprise the respiratory nitrate reductases (NarGH/I) and periplasmic nitrate reductases. In these enzymes azide competes with nitrate for the molybdenum active site [8,9]. Additional studies will be described in chapter VI aimed to understand how the active site is affected upon azide inhibition.

The most relevant result described in this chapter is that cyanide does not inhibit the *Dg* and *Da* W-Fdhs. As also observed in other molybdoenzymes [8,9], Mo-Fdh from *D. desulfuricans* in the presence of cyanide presents a mixed inhibition pattern [2,16] with  $K_{ic}$  four times smaller than  $K_{iuc}$ . This indicates that cyanide inhibition mainly occurs by competition with formate for the active site. EPR data are also in agreement with this conclusion. In this sense, the Mo(V) signal obtained after Fdh reduction with formate is modified when cyanide is present being this signal similar to the one obtained by incubation with azide [2]. The fact that *Da* Fdh and *Dg* Fdh are not inhibited by cyanide could be due to the presence of W instead Mo in the active site and/or the lack of the c-type hemes containing subunit present only in *Dd* Fdh. The latter is unlikely owing the competitive component of the inhibition is more important than the uncompetitive in *Dd* Fdh. On the other hand, Bertram *et al* demonstrated that the molybdenum formylmethanofuran dehydrogenase from *M. thermoautotrophicum* (an enzyme belonging to the DMSO reductase family) is inactivated by cyanide in contrast to the tungsten isoenzyme which is not affected by the presence of this molecule. Interestingly, when the tungsten atom from the formylmethanofuran dehydrogenase is

substituted by molybdenum, the enzyme becomes inactive after cyanide incubation [10].

The inhibition by cyanide of Fdh from *M. formicium* [5] was explained taking into account the behavior observed for xanthine oxidase and xanthine dehydrogenase enzymes, where the cyanide anion reacts with the sulfido ligand coordinated to molybdenum releasing thiocyanate [6]. In this chapter it was demonstrated that this hypothesis is unlikely, as *Dd* Fdh is not inactivated upon incubation with high concentrations of cyanide, showing that the activity can be recovered after dialyzing the enzyme against inhibitor-free buffer. This result indicates that cyanide is a reversible inhibitor of *Dd* Fdh and do not react with the terminal sulfur ligand to the Mo as observed in XO and XDH.

A careful analysis of the three-dimensional structures of the Fdhs active site cores (figure V.14) shows that some conserved aminoacids in the W-Fdhs from *D. gigas* and *D. alaskensis* are different from the *Dd* Mo-Fdh. These aminoacids together with the presence of a W atom at the active site could give some clues to explain why these two W-Fdhs have comparable kinetic behaviors towards substrate and inhibitors and present some differences when compared with the *Dd* Mo-Fdh.

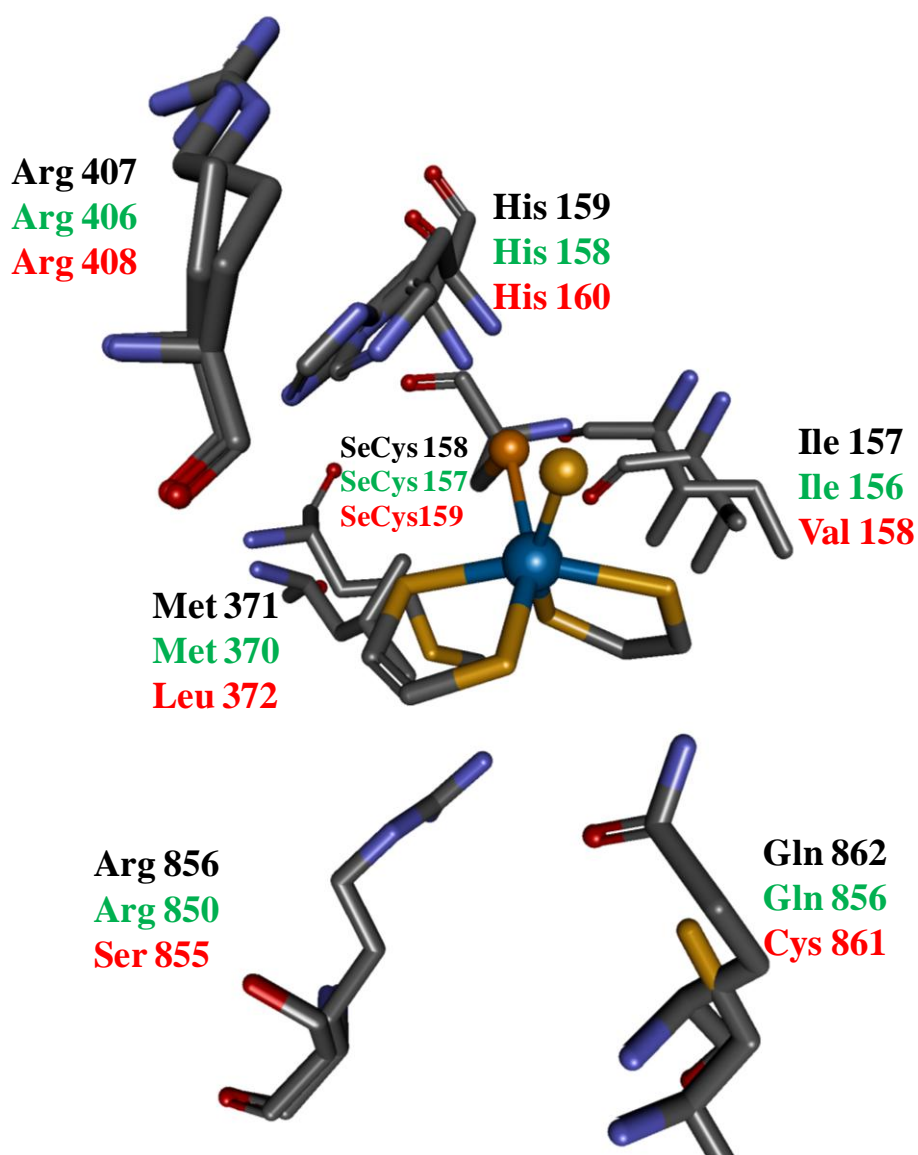


**Figure V.14| Fdhs active sites overlapped.** Fdhs active sites with aminoacids from neighborhood from *D. gigas* (black), *D. alaskensis* (green) and *D. desulfuricans* (red). The overlay was done using the structure of Fdh from *D. gigas* [19] as support.

## V.6 References

- 1 Cornish-Bowden, A. Fundamentals of Enzyme Kinetics. 3rd edition edn, (PORTLAND PRESS, 2004).
- 2 Rivas, M. G., Gonzalez, P. J., Brondino, C. D., Moura, J. J. & Moura, I. EPR characterization of the molybdenum(V) forms of formate dehydrogenase from *Desulfovibrio desulfuricans* ATCC 27774 upon formate reduction. J Inorg Biochem 101, 1617-1622, (2007).
- 3 Axley, M. J. & Grahame, D. A. Kinetics for formate dehydrogenase of *Escherichia coli* formate-hydrogenlyase. J Biol Chem 266, 13731-13736, (1991).
- 4 Liu, C. L. & Mortenson, L. E. Formate dehydrogenase of *Clostridium pasteurianum*. J Bacteriol 159, 375-380, (1984).
- 5 Barber, M. J., May, H. D. & Ferry, J. G. Inactivation of Formate Dehydrogenase from *Methanobacterium formicicum* by Cyanide. Biochemistry 25, 8150-8155, (1986).
- 6 Wahl, R. C. & Rajagopalan, K. V. Evidence for the inorganic nature of the cyanolyzable sulfur of molybdenum hydroxylases. J Biol Chem 257, 1354-1359, (1982).
- 7 Bursakov, S. A., Carneiro, C., Almendra, M. J., Duarte, R. O., Caldeira, J., Moura, I. & Moura, J. J. Enzymatic properties and effect of ionic strength on periplasmic nitrate reductase (NAP) from *Desulfovibrio desulfuricans* ATCC 27774. Biochem Biophys Res Commun 239, 816-822, (1997).
- 8 Butler, C. S., Charnock, J. M., Bennett, B., Sears, H. J., Reilly, A. J., Ferguson, S. J., Garner, C. D., Lowe, D. J., Thomson, A. J., Berks, B. C. & Richardson, D. J. Models for molybdenum coordination during the catalytic cycle of periplasmic nitrate reductase from *Paracoccus denitrificans* derived from EPR and EXAFS spectroscopy. Biochemistry 38, 9000-9012, (1999).
- 9 Elliott, S. J., Hoke, K. R., Heffron, K., Palak, M., Rothery, R. A., Weiner, J. H. & Armstrong, F. A. Voltammetric studies of the catalytic mechanism of the respiratory nitrate reductase from *Escherichia coli*: how nitrate reduction and inhibition depend on the oxidation state of the active site. Biochemistry 43, 799-807, (2004).



- 10 Bertram, P. A., Karrasch, M., Schmitz, R. A., Bocher, R., Albracht, S. P. & Thauer, R. K. Formylmethanofuran dehydrogenases from methanogenic Archaea. Substrate specificity, EPR properties and reversible inactivation by cyanide of the molybdenum or tungsten iron-sulfur proteins. *Eur J Biochem* 220, 477-484, (1994).
- 11 Boyington, J. C., Gladyshev, V. N., Khangulov, S. V., Stadtman, T. C. & Sun, P. D. Crystal structure of formate dehydrogenase H: catalysis involving Mo, molybdopterin, selenocysteine, and an Fe<sub>4</sub>S<sub>4</sub> cluster. *Science* 275, 1305-1308, (1997).
- 12 Raaijmakers, H. C. & Romao, M. J. Formate-reduced E. coli formate dehydrogenase H: The reinterpretation of the crystal structure suggests a new reaction mechanism. *J Biol Inorg Chem* 11, 849-854, (2006).
- 13 Moura, J. J., Brondino, C. D., Trincao, J. & Romao, M. J. Mo and W bis-MGD enzymes: nitrate reductases and formate dehydrogenases. *J Biol Inorg Chem* 9, 791-799, (2004).
- 14 Liu, M. C. & Peck, H. D., Jr. The isolation of a hexaheme cytochrome from *Desulfovibrio desulfuricans* and its identification as a new type of nitrite reductase. *J Biol Chem* 256, 13159-13164, (1981).
- 15 Legall, J., Mazza, G. & Dragoni, N. [Cytochrome C3 of *Desulfovibrio Gigas.*]. *Biochim Biophys Acta* 99, 385-387, (1965).
- 16 Rivas, M. G. Molybdenum-containing proteins from Sulphate Reducing Bacteria: studying proteins with novel cofactors and revealing new features of old enzymes. Ph.D. thesis, Faculdade de Ciências e Tecnologia - Universidade Nova de Lisboa, (2006).
- 17 Blanchard, J. S. & Cleland, W. W. Kinetic and chemical mechanisms of yeast formate dehydrogenase. *Biochemistry* 19, 3543-3550, (1980).
- 18 Coughlan, M. P., Johnson, J. L. & Rajagopalan, K. V. Mechanisms of inactivation of molybdoenzymes by cyanide. *J Biol Chem* 255, 2694-2699, (1980).
- 19 Raaijmakers, H., Macieira, S., Dias, J. M., Teixeira, S., Bursakov, S., Huber, R., Moura, J. J., Moura, I. & Romao, M. J. Gene sequence and the 1.8 Å crystal structure of the tungsten-containing formate dehydrogenase from *Desulfovibrio gigas*. *Structure* 10, 1261-1272, (2002).



# Chapter VI

*Theoretical methods revising spectroscopic data*

## VI.1 Summary

During the last two decades, formate dehydrogenases are being the subject of exhaustive research. However, contradictory conclusions have been elaborated on the basis of studies performed by means of different techniques like X-ray crystallography, X-ray absorption spectroscopy and EPR spectroscopy. In this chapter, DFT calculations along with an exhaustive literature analysis were performed in order to reconcile the available structural and spectroscopic data obtained in Mo and W containing Fdhs. Two different active site models were proposed in order to explain most of the experimental observations reported to date. In addition, these models have impact in the knowledge of the catalytic mechanism discussed in Chapter IV.

## VI.2 Introduction

Formate dehydrogenases share high primary sequence identity and show very similar polypeptide folds. The soluble heterotrimeric Fdh from *D. desulfuricans* is a Mo-containing enzyme with a catalytic subunit sharing very high sequence identity with the *Dg* W-Fdh (53%) [1,2]. Although the crystallographic structure of *Dd* Fdh is not available, 3D modeling suggest that the polypeptide fold of the catalytic subunit and the Mo ion coordination are very similar to those of *Dg* Fdh, *Ec* Fdh-H and *Ec* Fdh-N (RMSD of 0.5 Å for all backbone atoms).

The crystallographic structure of the hexacoordinated oxidized Mo or W atom (figure VI.1A) and the re-interpretation of this structure on basis of *Ec* Fdh-H, *Dg* FdhAB, *Dd* Nap and *Cn* Nap showing that the OH<sub>x</sub> ligand is a sulfur atom (figure VI.1B) [1,3-5] were described in Chapter II and IV. In Chapter IV, taking into account these models, DFT calculations demonstrated that the S and SeCys ligands can rearrange through a sulfur-shift process allowing the direct coordination of the substrate to the metal ion (figure VI.1C) [6].

According with this rearrange in the metal active site, X-ray data obtained with the formate-reduced form of Fdh-H showed that the Mo ion is pentacoordinated in a square pyramidal geometry. The base of the square pyramid comprises the four sulfur atoms from the two pyranopterin cofactors and the apical ligand is the Se atom from the SeCys residue (figure VI.1D) [7]. A recent reanalysis of this structure demonstrated that the

original crystallographic data was misinterpreted and that the apical ligand is in fact a terminal sulfur atom and that the Se atom is 11 Å away from the Mo ion (figure VI.1E) [5].

X-ray absorption spectroscopy (XAS) studies performed in an oxidized Fdh-H (incubated in O<sub>2</sub> atmosphere) suggested a similar coordination environment as in the original crystallographic report, i.e. with an oxygenic species bound to the Mo ion (figure VI.1A) [8]. XAS studies in the oxidized form of *Dd* Fdh yielded identical conclusions [9]. More strikingly it is the fact that in the reduced form of Fdh-H (incubated with dithionite) the molybdenum K-edge data indicated a Mo-Se and Mo-O ligation (2.62 Å and 2.10 Å, respectively) [8]. Selenium K-edge data recorded in this protein confirmed the Mo-Se bond distance and also indicated a short Se-S and Se-C bonds (2.20 Å and 1.98 Å, respectively) [8]. This coordination environment (figure VI.1F) does not fit with any of the crystallographic structures of the reduced Fdh-H reported by Boyington *et al* (figure VI.1D) and Raaijmakers *et al* (figure VI.1E) [5,7,8].

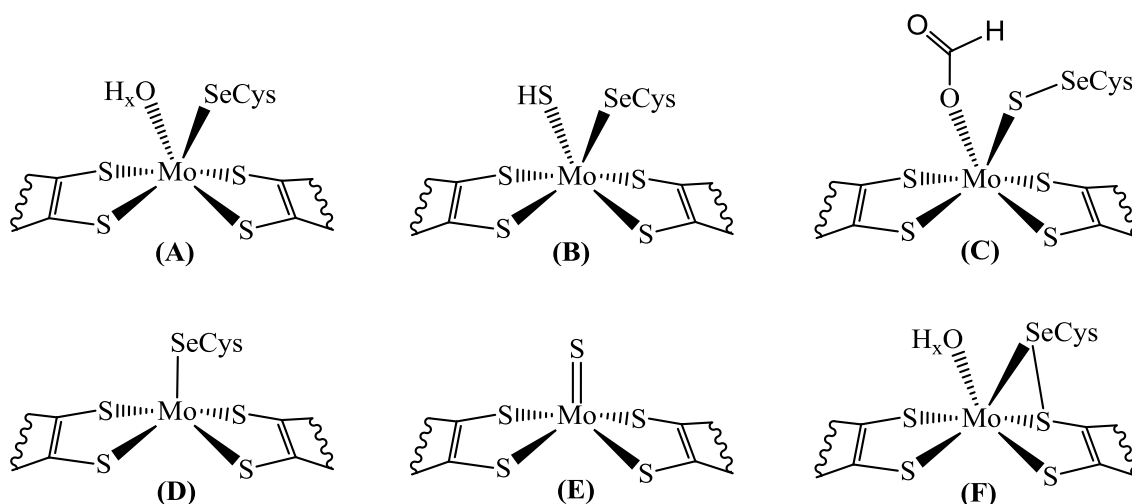


**Figure VI.1| Schematic representations of the several Mo ion coordination sphere proposed by several authors based on different experimental evidences.** X-ray crystallography: (A), (B), (D) and (E). DFT calculations: (C). XAS spectroscopy: (F).

EPR studies performed in *Ec* Fdh-H reduced with sodium formate identified a Mo(V) signals with unusual high anisotropy [10-12]. The EPR spectrum presented a nearly axial symmetry with an unusually high  $g_{zz}=2.094$  and therefore named *2.094* signal [11]. Using a <sup>77</sup>Se labeled Fdh-H sample the authors also observed a strong hyperfine

coupling (hfc) of  $^{77}\text{Se}$  ( $I=3/2$ ) with the Mo(V) ion and suggested a direct coordination of Se with Mo [11]. This is in agreement with the XAS and X-ray data summarized in figure VI.1D and 1F but in contrast with the more recent X-ray data depicted by figure VI.1E [5,7,8]. Hyperfine structure arising from the coupling with a solvent exchangeable proton was also observed ( $A_{zz}=7.5$  MHz,  $A_{yy}=18.9$  MHz,  $A_{xx}=20.9$  MHz) [11]. This proton was assigned to the alpha-proton of the formate that is transferred upon substrate oxidation to a Mo ligand that permits exchanging with the solvent in the second timescale [11]. The effect of a white light beam to this sample did not significantly affected the hfc of  $^{77}\text{Se}$ , but induced the photolysis of the exchangeable proton with the concomitant disappearance of the hfc and a shift of  $g_{zz}$  from 2.094 to 2.106 [11]. These evidences led the authors to conclude that the SeCys is not the group binding the strongly coupled proton and that there is a  $-\text{XH}$  group coordinated to the Mo(V) ion, similar to the models depicted in figure VI.1A, 1B and 1F.

More recent biochemical and EPR studies in the Mo-containing Fdh from *D. desulfuricans* demonstrated that X-ray crystallography, XAS, and EPR studies in *Ec* Fdh-H were performed with an inhibited form of the enzyme [13]. This was concluded because 3 mM azide was used as an additive in the preparations used for all the studies performed with Fdh-H [5,7,8]. The 2.094 Mo(V) signal obtained by reducing *Ec* Fdh-H with either dithionite or formate was also obtained in *Dd* Fdh when reducing a sample in the presence of inhibitors like azide or cyanide (figure VI.2A and B). These Mo(V) signals showed highly similar  $g$ -values and hyperfine structure to that described for *Ec* Fdh-H 2.094 Mo(V) species [13].

In the absence of inhibitors, the Mo(V) species obtained from *Dd* Fdh using either dithionite or formate are very different. The EPR signal obtained upon formate reduction (figure VI.2C and D) is rhombic and have smaller anisotropy ( $g_{zz}=2.012$ ,  $g_{yy}=1.996$  and  $g_{xx}=1.985$ ) compared to the 2.094 signal. In addition, hyperfine structure from two strongly coupled protons can be observed. The hyperfine splitting of the  $g_{zz}$  ( $A_{zz}=35$  MHz) is associated with a non solvent exchangeable proton, which was proposed to be one of the  $\beta$ -methylene protons of the coordinating SeCys residue on the basis of ENDOR spectroscopy studies performed in the periplasmic nitrate reductase from *P. pantotrophus* [14]. The strongly coupled proton splitting the three main  $g$ -values ( $A_{zz}=23$  MHz,  $A_{yy}=30$  MHz,  $A_{xx}=28$  MHz) is solvent exchangeable and was proposed to be the proton of the  $-\text{XH}$  ligand of Mo [13].

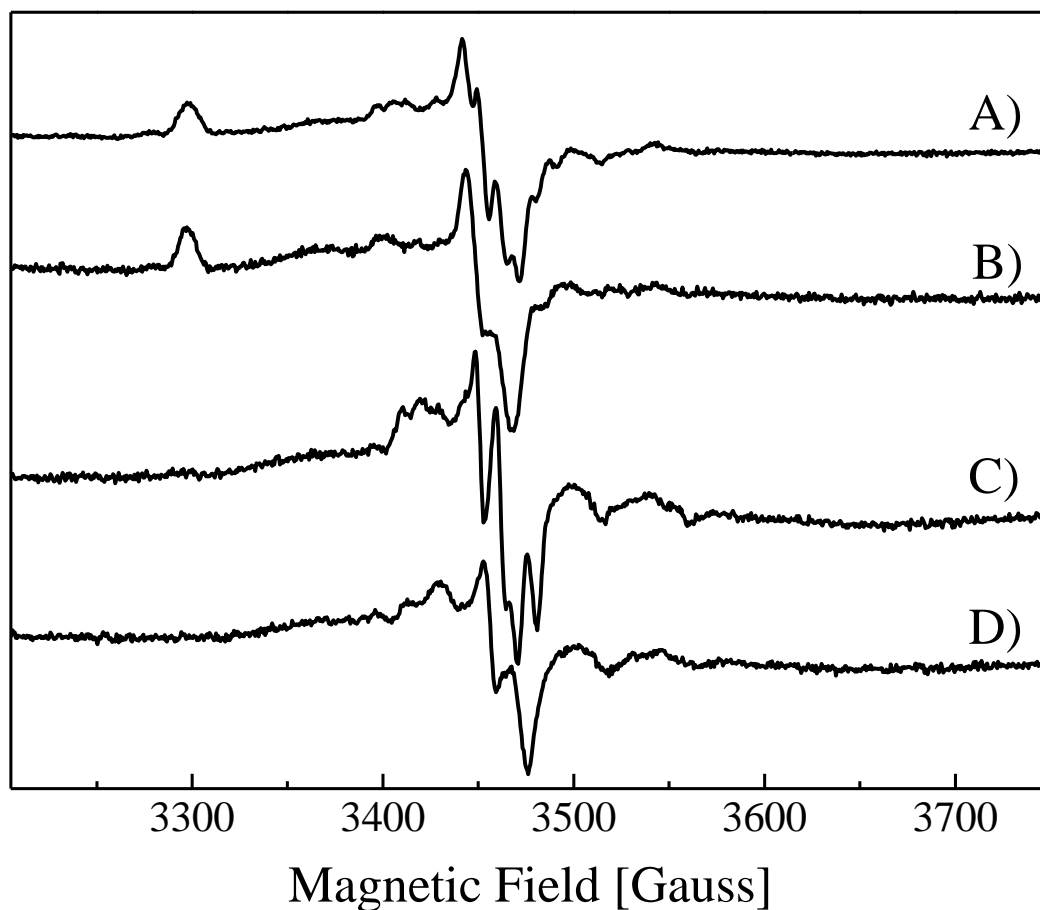


**Figure VI.2** CW-EPR spectra obtained in *Dd Fdh* samples (200  $\mu$ M) in presence or absence of the competitive inhibitor azide. A) Formate-reduced *Dd Fdh* incubated with 3 mM sodium azide in H<sub>2</sub>O-buffer. B) As A) but in D<sub>2</sub>O-buffer. C) Formate-reduced *Dd Fdh* in H<sub>2</sub>O-buffer. D) As C) but in D<sub>2</sub>O-buffer. Measurement conditions: Microwave frequency, 9.65 GHz; Modulation frequency, 100 kHz, Modulation amplitude, 5Gpp; Microwave power, 2 mW; Temperature, 100 K.

All these contradictory experimental evidences and conclusions obtained by several authors were never carefully revised. In an attempt to reconcile all the experimental data reported to date, DFT calculations were used to explain the structural nature of these two paramagnetic Mo(V) species and understand their role in the catalytic mechanism of Fdh.

**VI.3 Theoretical methods.**

**VI.3.1 Structure optimizations.** Structure optimizations were performed using Gaussian 03 [15]. The hybrid B3LYP functional and Lanl2DZ and 6-31G\*\* basis set (for Mo and the remaining atoms, respectively) were used as implemented in the software package [16-19]. All the structures were optimized in the vacuum with all atoms coordinates free, assuming a  $\text{Mo}^{5+}$  ion and  $[\text{H}_2\text{C}_2\text{S}_2]^{2-}$ ,  $[\text{SeCH}_3]^{1-}$ ,  $[\text{XH}]^{1-}$  and  $[\text{X}]^{2-}$ . Only for the case of the hexacoordinated Mo ion in trigonal prismatic geometry it was necessary to optimize a partially frozen structure. For this, the atom coordinates of a  $[\text{Mo}^{\text{V}}(\text{dithiolene})_3]^{1-}$  model was optimized in order to obtain a trigonal prismatic Mo coordination geometry. Then, one entire dithiolene ( $[\text{H}_2\text{C}_2\text{S}_2]^{2-}$ ) was deleted and replaced by a  $[\text{SeCH}_3]^{1-}$  and  $[\text{XH}]^{1-}$  ligand (X= O, S), respectively. The structure was further optimized with the coordinates of the Mo ion and the four dithiolene S atoms frozen, which was necessary to keep the trigonal prismatic geometry.

**VI.3.2 EPR parameters.** EPR parameters were calculated using the ORCA 2.8 package [20]. The hybrid B3LYP functional was used along with basis sets TZVP (for Mo, S and Se) and SVP (for H, C, N and O). The ZORA formalism was also included in the calculations [21,22]. Main  $g$ -values are those reported in the output file which are calculated as  $[g = g_e + g_{\text{RMC}} + g_{\text{DSO}} + g_{\text{PSO}}]$ ; where  $g_e$  is the  $g$  of free electron,  $g_{\text{RMC}}$  is the relativistic mass correction,  $g_{\text{DSO}}$  is the diamagnetic spin-orbit term (gauge-correction), and  $g_{\text{PSO}}$  is the paramagnetic spin-orbit term (Orbital Zeeman / Spin Orbit Coupling). Each main value of the hyperfine coupling are those reported in the output file of the calculations which are predicted as  $[A = A_{\text{FC}} + A_{\text{SD}} + A_{\text{SO}}]$ ; where  $A_{\text{FC}}$  is the Fermi contact contribution (finite spin density on the nucleus under investigation),  $A_{\text{SD}}$  the spin-dipolar interaction (magnetic dipole interaction of the magnetic nucleus with the magnetic moment of the electron), and  $A_{\text{SO}}$  the spin-orbit coupling (second order contribution).



## VI.4 Results

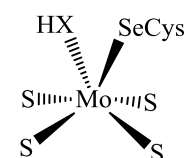
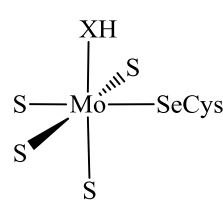
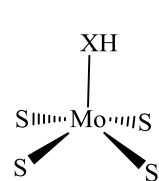
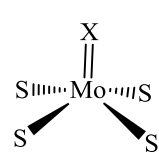
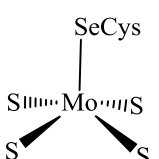
The Mo ion present in the Fdh active site can be found in the +4, +5 or +6 oxidation states. Of these three possible states, only the Mo(V) state has paramagnetic properties ([Ar] 3d<sup>1</sup>, S=½) that permit using the metal ion as a paramagnetic probe.

On the basis of the evidences summarized in the introduction section, DFT calculations were used to explain reported experimental results obtained with *Ec* Fdh-H and *Dd* Fdh. For the *azide* (2.094) Mo(V) species it was necessary to speculate which factors yield a Mo(V) EPR signal with such unusual anisotropy and low rhombicity. On the other hand, for the *formate* Mo(V) species it was necessary to obtain g-values corresponding to a rhombic signal with small anisotropy. In order to obtain this parameters, a series of models resembling figures VI.1A, B, D and E were built and their structures were optimized using Gaussian 03 package as described in the materials and methods section [15]. The atom coordinates of the resulting optimized structures were used to calculate the main g- and A-values with the ORCA 2.8 package [20] (table VI.1). The g- and A-values calculated with the hexacoordinated models (table VI.1, structure models A and B) fitted neither the *azide* (2.094) nor the *formate* Mo(V) EPR signals. Different authors have proposed that a square-pyramidal geometry would explain the symmetry of the *azide* (2.094) signal, arguing that the apical S or Se ligand are very strong ligands to the Mo ion and dictates the d<sub>xy</sub> character of the electronic ground state of the 2.094 species [11,13]. However, the DFT calculations indicated that the models with square-pyramidal geometry (figures VI.1D and 1E) can yield nearly axial EPR signals with relatively high anisotropy and low rhombicity, but not comparable with the values observed for the *azide* (2.094) signal (table VI.1, structure models C, D and E).

**Table VI.1| Summary of experimental and simulated  $g$ - and  $A$ -values (of the exchangeable proton, -XH) of the *formate* and *azide* Mo(V) signals and those obtained through DFT calculations of the structural models resembling the reported X-ray structures. A) Trigonal prismatic; B) Octahedral; C), D) and E) square-pyramidal. Anisotropy and rhombicity were calculated as  $[g_{zz}-g_{xx}]$  and  $[(g_{zz}-g_{yy})/(g_{zz}-g_{xx})]^*$ , respectively.  $A$ -values are in MHz.**

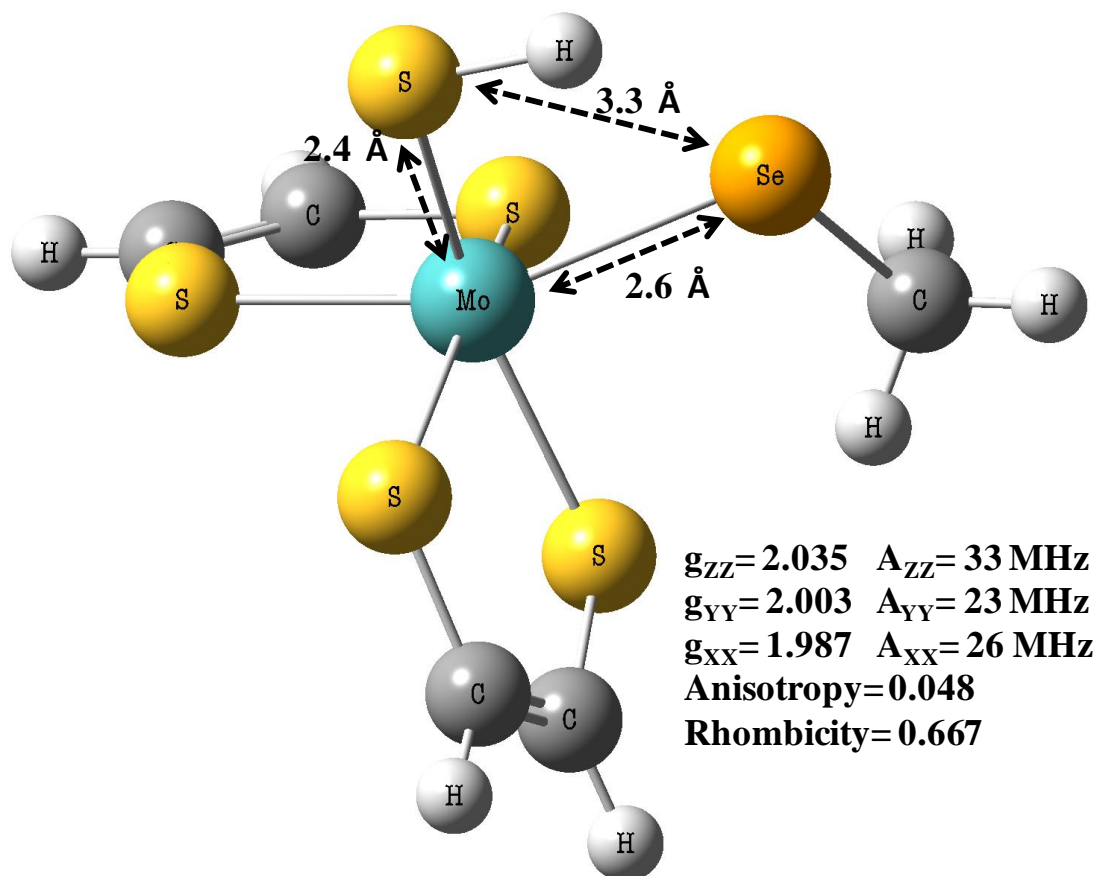
Mo(V) EPR signal		$g_{zz}$ ( $A_{zz}$ )	$g_{yy}$ ( $A_{yy}$ )	$g_{xx}$ ( $A_{xx}$ )	Anisotropy	Rhombicity
Formate		<b>2.012</b> (23)	<b>1.996</b> (30)	<b>1.985</b> (28)	<b>0.027</b>	<b>0.592</b>
Azide (2.094)		<b>2.092</b>	<b>2.000</b> (21)	<b>1.989</b> (21)	<b>0.103</b>	<b>0.893</b>

Structural model	X	$g_{zz}$ ( $A_{zz}$ )	$g_{yy}$ ( $A_{yy}$ )	$g_{xx}$ ( $A_{xx}$ )	Anisotropy	Rhombicity
A) 	S	2.034 (8)	2.009 (2)	1.995 (0.2)	0.039	0.641
	O	2.010 (75)	2.002 (58)	1.988 (57)	0.022	0.364
B) 	S	2.017 (57)	2.012 (50)	1.989 (49)	0.028	0.179
	O	2.027 (42)	2.010 (25)	1.958 (23)	0.069	0.246
C) 	S	2.032 (21)	2.000 (11)	1.969 (10)	0.063	0.508
	O	2.043 (19)	1.999 (7)	1.965 (6)	0.078	0.564
D) 	S	2.030	2.019	1.994	0.036	0.306
	O	2.030	2.010	1.998	0.032	0.625
E) 		2.027	1.997	1.975	0.052	0.577

\*According to the equation to calculate Rhombicity, a rhombic signal yield a value c.a. 0.500, an axial signal with  $g_{//} > g_{\perp}$  a value c.a. 1.000, and an axial signal with  $g_{//} < g_{\perp}$  a value c.a. 0.000.

In addition, none of these models can explain all the EPR spectroscopy results reported to date since, in the model of figure VI.1E there is no Se atom coordinating the Mo(V) ion (as concluded from EPR studies with  $^{77}\text{Se}$ -labeled Fdh-H) and in the model of figure VI.1D there is no Mo–XH ligand that explain the strong hfc with a solvent-exchangeable proton (showed by CW-EPR of normal and light-irradiated samples) [11]. Using a different approach, the atoms coordinates of the active site of oxidized *Dg* Fdh (Resolution 1.80 Å, PDB code: 1H0H [1]) were used to build a new structural model. The W atom was replaced by a Mo atom and the unknown sixth ligand was assigned as a sulfur atom. The model was completed adding an H atom bound to the terminal S ligand. The position of this proton was structurally optimized with Gaussian 03 package using the method described in the materials and methods section. The predicted anisotropy, rhombicity and the hyperfine coupling main values of the exchangeable proton (–SH ligand) obtained by DFT calculations (figure VI.3) are very close to those observed experimentally for the *formate* signal, making this structural model a good candidate to explain the EPR properties of this Mo(V) species. Interestingly, the Mo coordination geometry of this model is neither pure octahedral nor trigonal-prismatic, as these geometries do not yield the EPR parameters observed experimentally (table VI.1). Visual analysis of the structure depicted in figure VI.3 indicates that the Mo coordination geometry is an intermediate in-between the octahedral and the trigonal-prismatic conformations. It is important to mention that the Se-SH bond distance (3.3 Å) indicates the absence of interaction between these two atoms.



**Figure VI.3| 3D view of the structural model used to predict EPR parameters of the *formate* Mo(V) species.** Predicted  $g$ -values and hfc constants of the exchangeable proton bound to the  $-SH$  group are written next to the model.

The next step was to obtain a structural model for the *azide* (2.094) signal that explains both the EPR and XAS parameters. After careful analysis of the XAS spectroscopy reported data of *Ec Fdh-H* (note: remember that this enzyme was always studied in the presence of 3 mM sodium azide, therefore all the spectroscopic data should correspond to the *azide* (2.094) Mo(V) species), we found that a Mo-O interaction was actually not observed in the XANES spectra of neither the oxidized nor reduced form of the enzyme. Moreover, a Mo-O interaction was not necessary to fit the corresponding Mo and Se K-edge EXAFS spectra, indicating that neither a Mo-O nor a Se-O interaction was observed in the *Ec Fdh-H* samples [8]. George *et al* proposed a model biased by the crystallographic structure of *Ec Fdh-H* (figure VI.1F) [8]. They argue that the X-ray data would not wrongly fit an O atom in the electron density corresponding to the sixth coordination position of the Mo ion [7]. However, recent reanalysis of the crystallographic structure of *Ec Fdh-H*, and new X-ray data recorded with *Dd NapA* and

*Cn* NapAB native crystals, have shown unambiguously that the electron density of the OH<sub>x</sub> ligand was misinterpreted and that the sixth ligand to the Mo ion is a S atom in formate dehydrogenases and the closely related periplasmic nitrate reductases [1,3-5]. Taking this into account, an exhaustive search of models that would explain all EPR and XAS experimental observations on *Ec* Fdh-H was performed (not shown). The only model that fits better the XAS and EPR data is presented in figure VI.4. This model was obtained assuming a Mo ion in a pseudo square-pyramidal geometry, where the apical XH ligand was replaced by an [H-S-Se-CH<sub>3</sub>]<sup>2-</sup>. All the atom distances were set according to the bond distances observed by EXAFS [8]. The *g*-values, anisotropy and rhombicity of the predicted Mo(V) signal are reasonably close to those observed experimentally for the *azide* (2.094) Mo(V) species (table VI.1). In addition, the magnitude of the hyperfine coupling constants of the exchangeable proton (-SH) is remarkably close to those observed experimentally. However, the magnitude of the predicted A<sub>zz</sub> (29 MHz) is larger than expected, as no splitting of the g<sub>zz</sub> component can be observed in the experimental spectrum [11,13]. Along with this inconsistency, the predicted A<sub>xx</sub> is too small (10 MHz) as the g<sub>xx</sub> should be split in 21 MHz. Although the A<sub>ISO</sub> values of the exchangeable proton predicted through DFT calculations (20 MHz) and observed experimentally in the *azide* (2.094) signal (17 MHz, assuming A<sub>zz</sub>= 7.5 MHz as reported for *Ec* Fdh-H) are similar, the fact that the A<sub>zz</sub> and A<sub>xx</sub> values do not fit those observed experimentally is cumbersome and must be further investigated.

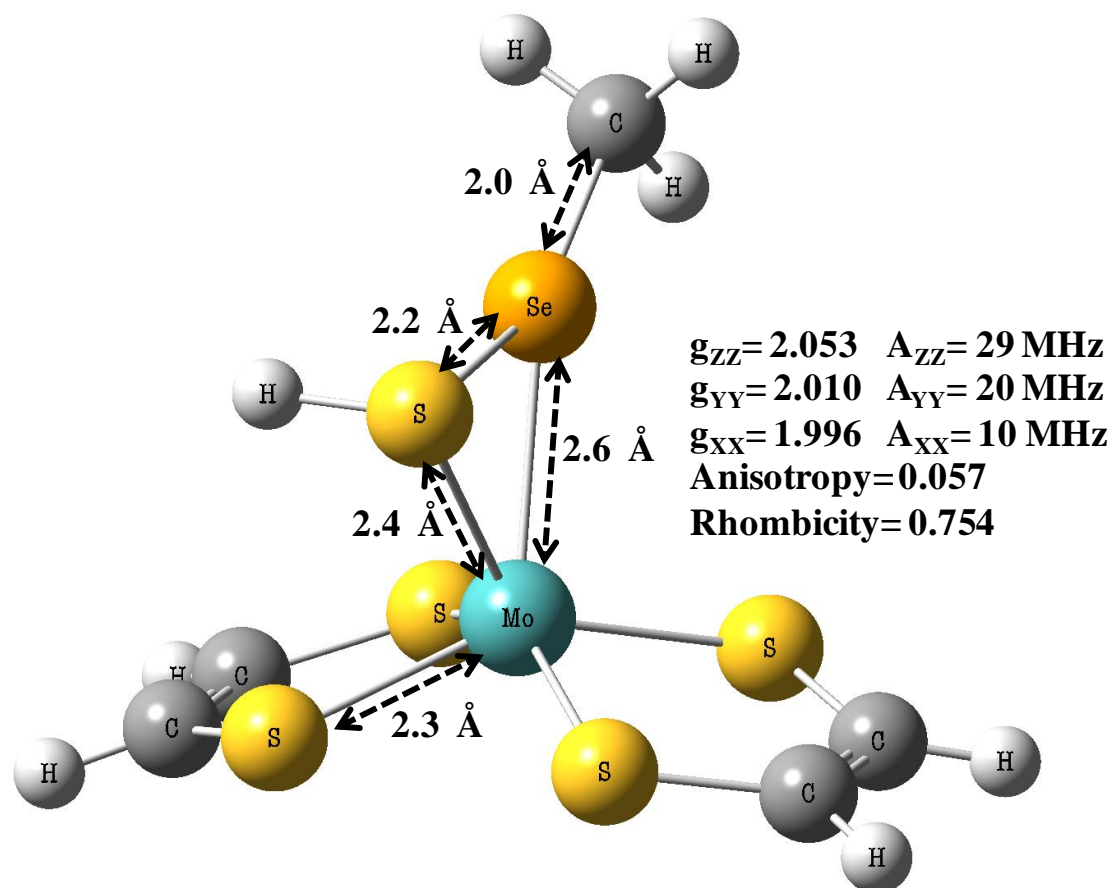


**Figure VI.4: 3D view of the structural model used to predict EPR parameters of the azide (2.094) Mo(V) species.** Predicted  $g$ -values and hfc constants of the exchangeable proton are written next to the model. The bond lengths specified in the model were frozen according to the EXAFS data.

## VI.5 Discussion

Density functional theory methods have been used to hypothesize structural models of the paramagnetic Mo(V) site of formate dehydrogenases to explain all the spectroscopic (EPR and XAS) observations reported to date.

First, a series of structural models with different coordination numbers (hexa- or pentacoordinated) and geometries (octahedral, trigonal-prismatic, and square-pyramidal) were analyzed in order to evaluate whether they fit the main  $g$  and  $A$  values observed through EPR spectroscopy studies performed in both *Dd Fdh* and *Ec Fdh-H* [11,13]. In these models the sixth ligand to the Mo(V) ion (-XH) was assumed as either an O or S atom. None of the nine models analyzed and that are summarized in table

VI.1 yielded EPR parameters that reasonable approximate those observed experimentally in the *formate* and *azide* (2.094) species. From the analysis summarized in table VI.1 it was also possible to see that Mo(V) sites with square-pyramidal coordination geometry yield g-values corresponding to an axial EPR signal with  $g_{\parallel} > g_{\perp}$  as in the *azide* (2.094) signal. However, the anisotropy magnitudes calculated from the predicted g-values are remarkably smaller than those observed for the *azide* (2.094) species. These results, along with the fact that EPR spectroscopy studies performed with *Ec* Fdh-H detected both a strong hfc with  $^{77}\text{Se}$  and an exchangeable proton bound to a Mo ligand (-XH), suggested that a pentacoordinated Mo(V) site cannot explain the *azide* (2.094) species. An axial EPR signal with both relatively high anisotropy and satisfactory rhombicity was obtained assuming a hexacoordinated Mo(V) site with a Mo-Se and S-Se bond distances similar to those observed by EXAFS (figure VI.4). This model is in agreement with both EPR and XAS experimental observations, as a Mo-Se, Mo-SH and Se-S interactions are present.

The structural models used to explain the *formate* and the *azide* (2.094) signals show the same coordination number. However, the distorted octahedral geometry of the model of figure VI.3 yielded completely different g-values that are similar to those observed in the *formate* signal. In contrast to the hypothesis that the addition of azide affects the coordination number of the Mo(V) ion, the present results suggest that the presence of the inhibitor modify the coordination geometry of the metal ion, which has drastic effects in the symmetry of the EPR signal.

In Chapter IV it was mentioned that when a Mo(V) ion was assumed, the Mo-Se bond is broken generating a pentacoordinated metal ion. This was not observed in the DFT calculations presented in this chapter. This difference can be explained with the different protonation states of the inorganic sulfur ligand of the Mo ion used in Chapter IV and Chapter VI. The presence of an additional proton in the -SH ligand would stabilize the extra negative density of the one-electron reduced Mo site, cushioning the electrostatic repulsion that promotes the release of the  $\text{SeCH}_3$  ligand used in the model of Chapter IV.

#### *Mechanistic implications of this study.*

EPR spectroscopy studies performed with both *Ec* Fdh-H and *Dd* Fdh have shown that the exchangeable proton observed in the *azide* (2.094) signal is the H atom transferred from the substrate to the active site. According to the results presented in this chapter,

an exchangeable proton that produces a hyperfine coupling in the order of 20-30 MHz must be bound to a Mo ion ligand of the first coordination sphere. Therefore, according to the results presented in this and Chapter IV, the proton of the formate that is transferred to the Se anion would be subsequently transferred to the inorganic S atom bound to the Mo. Assuming that the proton transfer from the Se to the S ligand also happens in the azide-free sample, this provides an important clue on how the deprotonation and regeneration of the active sites would occur. In order to demonstrate this hypothesis, a study similar to that performed for the *azide* (2.094) signal should be performed. However, the timescale of proton/deuterium exchange of the strongly coupled proton of the *formate* signal is much shorter than for the azide inhibited sample (Mota *et al*, unpublished results). In order to overcome this, rapid-freeze quench techniques will be used.

## VI.6 References

- 1 Raaijmakers, H., Macieira, S., Dias, J. M., Teixeira, S., Bursakov, S., Huber, R., Moura, J. J., Moura, I. & Romao, M. J. Gene sequence and the 1.8 Å crystal structure of the tungsten-containing formate dehydrogenase from *Desulfovibrio gigas*. *Structure* 10, 1261-1272, (2002).
- 2 Costa, C., Teixeira, M., LeGall, J., Moura, J. J. G. & Moura, I. Formate dehydrogenase from *Desulfovibrio desulfuricans* ATCC27774: isolation and spectroscopic characterization of the active sites (heme, iron- sulfur centers and molybdenum). *J Biol Chem* 2, 198-208, (1997).
- 3 Najmudin, S., Gonzalez, P. J., Trincao, J., Coelho, C., Mukhopadhyay, A., Cerqueira, N. M., Romao, C. C., Moura, I., Moura, J. J., Brondino, C. D. & Romao, M. J. Periplasmic nitrate reductase revisited: a sulfur atom completes the sixth coordination of the catalytic molybdenum. *J Biol Inorg Chem* 13, 737-753, (2008).
- 4 Coelho, C., Gonzalez, P. J., Trincao, J., Carvalho, A. L., Najmudin, S., Hettman, T., Dieckman, S., Moura, J. J., Moura, I. & Romao, M. J. Heterodimeric nitrate reductase (NapAB) from *Cupriavidus necator* H16: purification, crystallization and preliminary X-ray analysis. *Acta Crystallogr Sect F Struct Biol Cryst Commun* 63, 516-519, (2007).



- 5 Raaijmakers, H. C. & Romao, M. J. Formate-reduced *E. coli* formate dehydrogenase H: The reinterpretation of the crystal structure suggests a new reaction mechanism. *J Biol Inorg Chem* 11, 849-854, (2006).
- 6 Mota, C. S., Rivas, M. G., Brondino, C. D., Moura, I., Moura, J. J., González, P. J. & Cerqueira, N. M. The mechanism of formate oxidation by metal-dependent formate dehydrogenase. Submitted, (2010).
- 7 Boyington, J. C., Gladyshev, V. N., Khangulov, S. V., Stadtman, T. C. & Sun, P. D. Crystal structure of formate dehydrogenase H: catalysis involving Mo, molybdopterin, selenocysteine, and an Fe<sub>4</sub>S<sub>4</sub> cluster. *Science* 275, 1305-1308, (1997).
- 8 George, G. N., Colangelo, C. M., Dong, J., Scott, R. A., Khangulov, S. V., Gladyshev, V. N. & Stadtman, T. C. X-ray Absorption Spectroscopy of the Molybdenum Site of *Escherichia coli* Formate Dehydrogenase. *J Am Chem Soc* 120, 1267-1273, (1998).
- 9 George, G. N., Costa, C., Moura, J. J. G. & Moura, I. Observation of Ligand-Based Redox Chemistry at the Active Site of a Molybdenum Enzyme. *J Am Chem Soc* 121, 2625-2626, (1999).
- 10 Gladyshev, V. N., Khangulov, S. V., Axley, M. J. & Stadtman, T. C. Coordination of selenium to molybdenum in formate dehydrogenase H from *Escherichia coli*. *Proc Natl Acad Sci U S A* 91, 7708-7711, (1994).
- 11 Khangulov, S. V., Gladyshev, V. N., Dismukes, G. C. & Stadtman, T. C. Selenium-containing formate dehydrogenase H from *Escherichia coli*: a molybdopterin enzyme that catalyzes formate oxidation without oxygen transfer. *Biochemistry* 37, 3518-3528, (1998).
- 12 Gladyshev, V. N., Boyington, J. C., Khangulov, S. V., Grahame, D. A., Stadtman, T. C. & Sun, P. D. Characterization of crystalline formate dehydrogenase H from *Escherichia coli*. Stabilization, EPR spectroscopy, and preliminary crystallographic analysis. *J Biol Chem* 271, 8095-8100, (1996).
- 13 Rivas, M. G., Gonzalez, P. J., Brondino, C. D., Moura, J. J. & Moura, I. EPR characterization of the molybdenum(V) forms of formate dehydrogenase from *Desulfovibrio desulfuricans* ATCC 27774 upon formate reduction. *J Inorg Biochem* 101, 1617-1622, (2007).
- 14 Butler, C. S., Fairhurst, S. A., Ferguson, S. J., Thomson, A. J., Berks, B. C., Richardson, D. J. & Lowe, D. J. Mo(V) co-ordination in the periplasmic nitrate

- reductase from *Paracoccus pantotrophus* probed by electron nuclear double resonance (ENDOR) spectroscopy. *Biochem J* 363, 817-823, (2002).
- 15 Gaussian 03 v. Gaussian 03 v.revision D.01/D.02 (Gaussian, Inc., Pittsburgh, Pa, 2003).
- 16 Becke, A. D. Density-functional thermochemistry. III. The role of exact. *J Chem Phys* 98, 5648-5652, (1993).
- 17 Lee, C. T., Yang, W. T. & Parr, R. G. Development of the Colle-Salvetti Correlation-Energy Formula into a Functional of the Electron-Density. *Phys Rev B* 37, 785-789, (1988).
- 18 Stephens, P. J., Devlin, F. J., Chabalowski, C. F. & Frisch, M. J. Ab-Initio Calculation of Vibrational Absorption and Circular-Dichroism Spectra Using Density-Functional Force-Fields. *J Phys Chem* 98, 11623-11627, (1994).
- 19 Vosko, S. H., Wilk, L. & Nusair, M. Accurate Spin-Dependent Electron Liquid Correlation Energies for Local Spin-Density Calculations - a Critical Analysis. *Can J Phys* 58, 1200-1211, (1980).
- 20 Neese, F. The ORCA Program System. Wiley Review Series, in press, (2010).
- 21 Pantazis, D. A., Chen, X. Y., Landis, C. R. & Neese, F. All-electron scalar relativistic basis sets for third-row transition metal atoms. *J Chem Theory Comput* 4, 908-919, (2008).
- 22 Pantazis, D. A. & Neese, F. All-electron scalar relativistic basis sets for the lanthanides. *J Chem Theory Comput* 5, 2229-2238, (2009).

# **Chapter VII**

*Final remarks and future work*

The work described in this thesis was focused on the study of Mo- and W-containing formate dehydrogenases isolated from *Desulfovibrio* species.

The studies presented in Chapter III were aimed to understand the effects of Mo and W supplementation on both the gene expression levels and the biochemical properties of the Fdhs coded in the genome of *Desulfovibrio alaskensis*. The isolation of two different Fdhs (Mo/W-Fdh and W-Fdh) from *D. alaskensis* cells, the identification of the genes coding these enzymes, and the correlation of these data with the genes expression levels provide us a new example of an organism that containing two homologous enzymes, has mechanisms that allow the recognition and selective incorporation of Mo or W in the enzyme cofactor. However, the fact that the Mo/W-Fdh enzyme incorporates either Mo or W, open new questions about the metal specificity of the proteins involved in cofactor biosynthesis and the chaperones that assist the cofactor insertion. Future work including knockout experiments of the genes related to cofactor biosynthesis and insertion should be performed in order to obtain information about the processes regulating the specificity of Mo- or W-cofactor insertion into enzymes. On the other hand, the studies of the expression levels of the genes involved in tungstate transport provided an unexpected and very interesting result. Despite being closely contiguous genes arranged as in an operon, the *tup* genes, particularly the *tupA* and *tupB* components, does not belong to the same transcriptional unit. This unprecedented result open a new subject of study aimed to understand the regulation mechanisms of adjacent genes expression.

The mechanism of formate oxidation by Fdhs was presented in Chapter IV. This catalytic mechanism was predicted using DFT tools and correlating the theoretical observations with present and reported experimental data. The different proposals available in the literature based on theoretical and experimental data are rather incomplete or too empirical and do not fit all the experimental observations reported to date. The results presented in this thesis have shown that the substrate approximation forces a Mo-Se bond break in order to enable an available binding site to coordinate the Mo(VI) ion. This process was called sulfur-shift, and was also observed by different authors by simulating the catalytic mechanism of periplasmic nitrate reductases. In agreement with the experimental results, DFT calculations indicated that the abstraction of the proton from the formate is the rate limiting step of the catalytic mechanism. On the other hand, it was possible to assign the role for the highly conserved aminoacids that surround the active site. Future studies will be aimed to produce site-directed Fdh

mutants of these aminoacids in order to study the effect of either single or multiple mutations in the reaction rates and substrate specificity.

Chapter V presents an exhaustive study of the effect of common inhibitors of Mo and W enzymes on formate dehydrogenases isolated from different *Desulfovibrio* species. As expected, nitrate acts as a competitive inhibitor of Fdh, due to the structural homology with formate. On the other hand, azide is a mixed inhibitor with a stronger competitive component. The most intriguing result presented in this chapter arises from the inhibition studies performed with cyanide. This compound is a mixed inhibitor like azide but, in contrast to the latter, cyanide does not affect the formate oxidation rates by W-containing Fdhs. Owing the high sequence homology of the catalytic subunits of studied Fdhs, the different behavior of Mo- and W- containing Fdhs in presence of cyanide suggests that probably the metal composition or some aminoacids that were not mentioned as relevant in the neighborhood of the active site, have determinant roles in the catalytic mechanism. Further studies, covering the evaluation of site-directed mutants and Fdh forms with different metal composition (Mo or W) should be performed to identify the reasons behind the resistance to cyanide inhibition.

The structural models presented in Chapter VI correlated with a detailed literature examination help to hypothesize some key steps of the catalytic mechanism that cannot be theorized with the present knowledge. To support the conclusions mentioned in Chapter VI, the theoretical results need to be complemented with spectroscopic studies such as X-ray absorption spectroscopy (XANES and EXAFS) and EPR based techniques (ESEEM, HYSCORE and pulsed ENDOR spectroscopies).

While in the last years important advances were achieved in the understanding of Mo and W-enzymes, the challenging results presented here and in other recently published works continue raising new questions in this field, which need to be further studied in order to be answered in the oncoming years.